Passive damping for a flexure-based mechanism in cryogenic conditions

Ambaum, N.

Award date:
2021

TU/e - MSc program Mechanical Engineering (MW)
Dynamics and Control group

Passive damping for a flexure-based mechanism in cryogenic conditions

Graduation Project - Final report

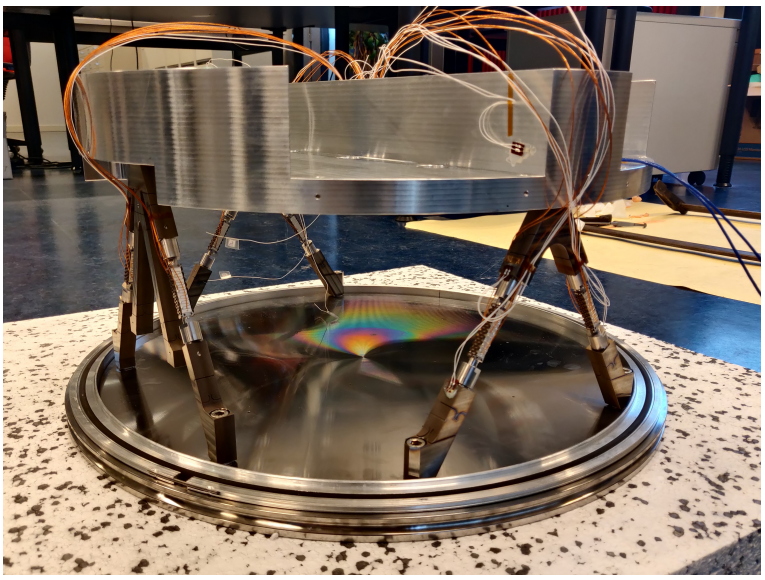

Report-number: DC 2021.029

Author:				
		N. (Niek)	Ambaum	0910516
Committee:				
Chairman	prof.	H. (Henk)	Nijmeijer	TU/e
Supervisor	prof.	J.P.M.B. (Hans)	Vermeulen	TU/e
Member	prof.	M. F. (Marcel)	Heertjes	TU/e
External Supervisor	dr.	B. (Bilal)	Mokrani	ASML

Eindhoven, 31st March 2021

Abstract

The high demand for semiconductor chips led to an urgent need to increase the productivity of lithography machines, which is translated into the search for more powerful electromagnetic actuators, used to accelerate and accurately position the wafer during exposure. Such powerful actuators are obtained by oversizing their permanent magnets (magnet table), which is limited by the available volume. To cope with this limit, a superconducting magnet is being developed, which would increase the magnetic field density by a factor 5 to 10.

The superconducting magnet coils need to operate at cryogenic temperatures, and thus requiring an appropriate fixation and thermal isolation. Such constraints result into undesired internal dynamics of the magnet coils' fixation design, with very lightly damped vibration modes. Conventional damping solutions become unsuitable as viscoelastic dampers lose their viscoelastic properties and become brittle while fluid dampers would simply solidify. This thesis addresses the passive damping of a superconducting planar motor, operating at cryogenic conditions.

First, eddy current damping is investigated, and implemented numerically on a simple model. It proved inefficient for this specific application due to the relatively low damping constant, achieved at the high frequencies and at a temperature of $T = 80$ K.

Alternatively, the use of piezoelectric shunt damping is proposed; this is already widely investigated for normal environments and the properties are not significantly impacted by temperature changes. It is shown that the damping performance only decreases 15.6% at temperature $T = 80$ K and 33.0% at $T = 4$ K. The study is conducted numerically by considering piezoelectric properties from the literature. Then, the resistive and inductive RL-shunt is implemented on a demonstrator of the superconducting magnet plate for experimental validation. A modal damping of $4.5\% - 4.7\%$ is obtained at $T = 77$ K $- 100$ K compared to 5.3% at room temperature.

Acknowledgements

This thesis is the result of my graduation project in the Dynamics and Control group as the final chapter to my master studies Mechanical Engineering at Eindhoven University of Technology. Closing this chapter would not have been possible without the help of a number of people. First of all I would like to thank my supervisor prof. Hans Vermeulen for giving me the opportunity of doing a project which was a combination of academic research, practical implementation and doing experiments. I also want to thank my supervisor dr. Bilal Mokrani, for the support and the valuable discussions we had throughout the process. Furthermore I want to express my gratitude to my colleague students, for the useful sessions on the Wednesday mornings. I would also like to thank prof. Henk Nijmeijer and prof. Marcel Heertjes, for taking part in my graduation committee. I hope you, and everybody else, will enjoy reading my report.

A lot of support during my master studies came from my parents Arthur and Helmi, by listening to me without really understanding what I was saying and putting things in perspective when needed. I am grateful to my housemates and friends for showing their interest and providing relaxation from time to time. Special thanks to my girlfriend, Caitlyn, for handling me when being grumpy if things did not go as planned and for providing distraction when needed.

Lastly, I would like to thank the COVID-19 pandemic, for giving me so much spare time to focus on my thesis.

Niek Ambaum

Nomenclature

Abbreviations

2D	two dimensional
DoF	degree of freedom
ECD	eddy current damping
EMF	electro-motive force
EPS	expanded polystyrene
EUV	extreme ultraviolet
FEM	finite element method/model
FRF	frequency response function
LN2	liquid nitrogen
RT	room temperature
SCPM	superconducting planar motor
TU/e	Eindhoven University of Technology

Greek Symbols

δ	state space coordinate	–
δ_s	skin depth	m
Δ	displacement at piezo-spring connection	m
ε	dielectric constant	F/m
η	modal decomposition coordinate	–
	material damping	–
γ_1	stiffness ratio of k over total stiffness.	–
γ_2	stiffness ratio of K_a over total stiffness.	–
μ	permeability	H/m
ν	fraction of strain energy	–
ω	natural frequency (with shorted electrodes)	–
Ω	natural frequency (with open electrodes)	–
Φ	eigencolumns	–
σ	electrical conductivity	S/m
ζ	damping ratio	–
ζ_0	natural damping ratio	–
ζ_{att}	damping ratio by attenuation level	–
ζ_d	obtainable damping ratio	–
ζ_e	electrical damping ratio	–

Roman Symbols

A	area	m^2
B	magnetic field	T
c	stiffness	N/m

C	capacitance (electric)	F
	capacitance (thermal)	J
c_p	specific heat capacitance (with constant pressure)	J/kg
d	damping constant	Ns/m
d_{33}	piezoelectric constant (axial electric to axial mechanical)	$-$
E	electrostatic field	$-$
	young's modulus	N/m^2
	energy	J
f	natural frequency	Hz
$f_{s,p}$	force (s, spring. p, piezo)	N
F	force	N
h	height	m
J	current density	A/m^2
k	stiffness	N/m
k_{33}	electromechanical coupling factor (axial electric to axial mechanical)	$-$
k_c	electromechanical coupling factor	$-$
K	global generalized coupling factor	$-$
K_a	stiffness of piezo transducer	N/m
L	length	m
	inductance	H
	latent heat of vaporization	J/kg
m	mass	kg
n	number of layers	$-$
Q	current	A
r	radius	m
R	resistance (electrical)	Ω
	resistance (thermal)	K/W
s	elastic compliance	m^2/N
t	thickness	m
T	temperature	K
v	velocity	m/s
V	voltage	V
W	width	m
Y	admittance	S
Z	impedance	Ω

Superscripts/Subscripts

D	constant electrical displacement (open electrodes)
E	constant electrical field (shorted electrodes)
l	numbering of piezoelectric transducer
S	constant strain
T	constant stress
$*$	constant electrical displacement (open electrodes)
c	conductor
e	effective (conductivity)
	electrical
m	mode number
r	remanent (magnetic field)

Contents

CHAPTER 1

Introduction

In current literature and practice, various passive damping methods are known and widely used for different applications. The difference between passive and active damping lies with the fact that passive damping uses simple devices without adding energy to the system, whereas active damping relies on a closed-loop system with a sensor, controller and actuator setup.

Under cryogenic and vacuum conditions, inherent damping of structures is significantly reduced and most classical passive damping methods become unsuitable or inefficient. Moreover, in view of the relatively poor efficiency to remove heat at cryogenic temperatures, interfaces to the environment are typically designed to have low thermal conductivity, hence poor (frictional) damping properties. The strength of flexure based designs comes from the monolithic manufacturing, which only contains material inherent damping, with typical loss factor $\eta = 0.001$ for structural metals [1]. This even becomes worse for cryogenic environments, as material damping decreases with temperature. Furthermore, viscoelastic dampers that are known to be effective under room temperature conditions, do not work at low temperature. Due to its temperature dependence, rubber loses its visco-elastic properties and becomes brittle at low temperature, leading to very low loss factor levels. Lastly, fluid or hydraulic dampers would simply freeze or solidify at cryogenic temperatures.

Most common cryogenic damping applications are aerospace related. Research on passive damping for cryogenic turbo-machinery has been performed in [2] and [3]. Both examined damping of rotor instabilities by means of passive damping in a cryogenic environment, stating Eddy Current Damping (ECD) as a feasible solution to proceed with. Furthermore, vibration damping mechanisms for space telescopes and interferometers operating below $T = 45$ K, have been investigated by [4], where modal damping of $\zeta = 0.04 - 0.08$ has been achieved down to $T = 17$ K. A second, more recent, application is vibration reduction for magnetic levitation (maglev) systems. The effectiveness of using eddy current damping in such systems is studied in [5] and [6] and shows improvements regarding the damping performance of the maglev systems.

On the other hand, piezoelectric shunt damping is also a promising solution for cryogenic applications. Indeed, piezoelectric shunt techniques have been already widely studied for normal environments (e.g. room temperature) [7][8], but not under cryogenic conditions. While it has been already demonstrated that the piezoelectric properties are not significantly impacted by temperature changes [9], their performance for damping under cryogenic conditions remains little explored. The piezoelectric properties are mostly studied in regard of actuating purposes [10][11][12], this would mean that there are also possibilities for the

use of piezoelectric shunt damping at cryogenic temperatures.

Other vibration reduction techniques for cryogenic applications are not of a damping nature, e.g. the use of undamped dynamic absorbers by [13] or working around the harsh environment by local temperature control as proposed by [14] for the damping of a cryogenic structure.

Problem definition and research question

In this work viable options for implementing passive damping for a flexure-based application in cryogenic conditions will be studied. In Chapter 2, an introduction to the Superconducting Planar Motor (SCPM) will be made, where some background on the system dynamics will be given. The demonstrator setup of the SCPM is also described. In Chapter 3 Eddy Current Damping (ECD) and piezoelectric shunt damping will be analysed by deriving an analytical model and simulating their damping performance. Consequently, piezoelectric shunt damping will be put forward as most promising passive damping solution for the SCPM. Then, the piezoelectric damping solution is optimized, detailed and implemented for the demonstrator of the SCPM in Chapter 4. In addition to theoretical analyses, mechanical design and related optimizations, the damping solution is also experimentally validated by cooling the demonstrator setup to $T = 77$ K of which the results can be found in Chapter 5.

The related research question to this work can be formulated as:

> *What is the most viable passive damping solution for the superconducting planar motor at cryogenic conditions?*

The related project goal is defined as:

> *Find the most viable passive damping solution for the superconducting planar motor based on theoretical analyses and deliver a realized, experimentally validated conceptual design.*

CHAPTER 2

Cryogenic application

Chapter 2 gives an introduction on the application of the SCPM and provides some detail on the system. After this, the demonstrator setup which will be used for experimental validation of the damping solution is described.

2.1 Cryogenics

In engineering, cryogenics is the science that addresses the production and effects of very low temperatures. Although the words "Kryo" (frost) and "Genic" (to produce) are as old as the Greek language, the term cryogenic was first used in 1894 as a reference to the liquefaction of 'permanent' gases. During this period, scientists were experimenting with the liquefaction of gases like oxygen, nitrogen, hydrogen and helium [15]. The boiling points corresponding to these gases where eventually found and are displayed in Table 2.1.

Table 2.1: Boiling points of 'permanent' gases (Adapted from: [15])

Cryogen		Temperature [K]	[C°]
Oxygen	(O_2)	90.2	-183.0
Nitrogen	(N_2)	77.4	-195.8
Hydrogen	(H_2)	20.3	-252.9
Helium	(He)	4.2	-269.0
Absolute zero		0	-273.15

Together with the boiling points of the permanent gases, also the absolute zero point is incorporated as a reference. The absolute zero point is the zero of the thermodynamic temperature scale, which is known as the Kelvin scale. In general, the term cryogenics is used for temperature below $T = 123.15$ K (-150 C°) [15].

Common applications for cryogenics are in the industrial and medical segment. Here, cryogenic temperatures is needed to meet thermal requirements or use is being made of material properties at cryogenic conditions, for example with conducting materials where the conductivity increases with decreasing temperature. Other applications include the fast freezing of some foods and to preserve materials like human blood, tissue and semen. Also, it can be used in cryosurgery where unwanted tissue can be destroyed using cryogenics.

2.2 Superconducting planar motor

The feasibility of a superconducting planar motor to replace the current magnet plate for wafer stage actuation of ASML's lithography machines (see Figure 2.1) has been investigated in [16]. The magnet plate is used to actuate stages in 6 Degrees of Freedom (DoF) while levitating them. For these machines to produce integrated circuits, it is needed to position the stages containing these wafers at nanometre accuracy under the projection optics. In order to obtain a higher throughput of wafers and thus productivity of the machine in the future, it is desired to move the wafer stages with increasing accelerations. The motion profile of the wafer stage exists of a stepping and a scanning phase, both taking approximately 50% of the exposure cycle of a wafer, of which the stepping time can be significantly reduced by increased acceleration [16][17].

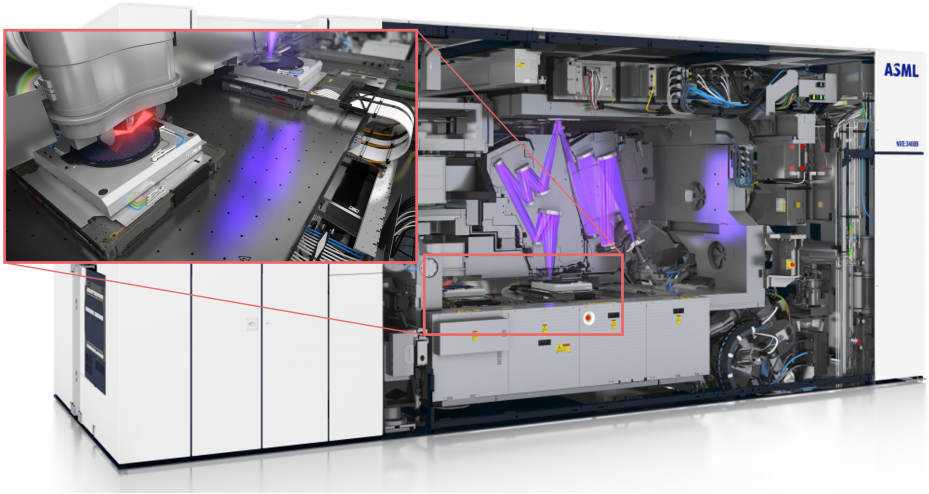

Figure 2.1: EUV machine with zoom on the wafer stages and magnet plate. (Source: [18])

Lorentz motors currently used in lithography systems are pushed to their limit and using them to increase acceleration further is challenging and requires to use bulky and strong magnets [16]. For this reason, the use of superconducting linear and planar motors has been studied in [19][20]. Due to their operation at cryogenic temperatures, it is possible to obtain a higher magnetic flux density (of 5-10× the current design [16]), increasing their performance with respect to current copper coils and permanent magnets. However, the fixation of superconductors is a challenge as designing for both stiffness and low thermal conductivity is conflicting in cryostat fixation designs. The main design challenges regarding a superconducting planar motor concept are addressed in the work of [16], where feasibility is shown in the end and a demonstrator setup is designed and realized.

2.2.1 Superconducting planar motor concept

An overview of the current design stack is shown in Figure 2.2 with the three main components being the cold frame (carrying the superconducting coils), the thermal shield (providing isolation for the cold frame) and lastly the vacuum vessel (needed for vacuum compatibility and functioning as main balance mass). The function of the balance mass is to avoid forces to be transferred towards the rest of the machine [17].

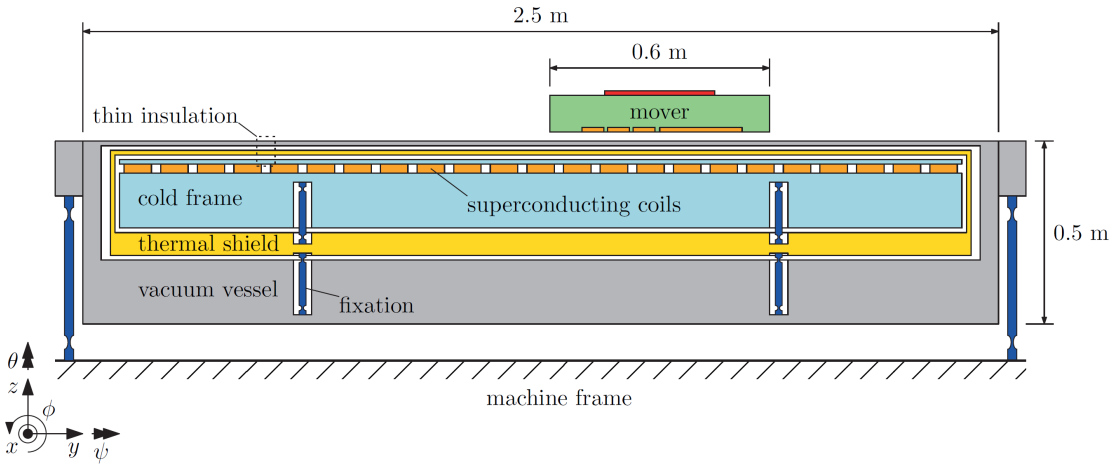

Figure 2.2: Stack-up of SC planar motor (Source: [16])

The function of the whole cryostat is to provide a stable low temperature and to include a mechanical fixation of the cold world [16]. A lumped model of the system can be found in Figure 2.3. The temperatures of the different components can be found in Table 2.2. The kinematic mounting of the different components is done by using 3 pairs of struts (of which the z-direction is schematically visualized), aiming for an exactly determined design by constraining all 6 degrees of freedom.

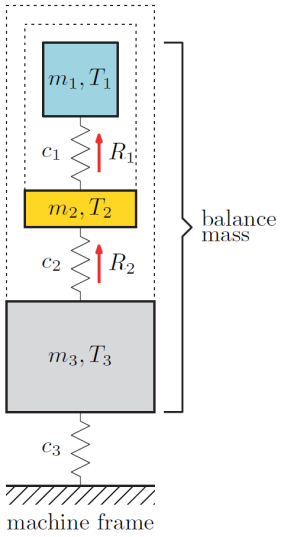

Figure 2.3: Lumped model of SC planar motor (Adapted from: [16])

Table 2.2: SC planar motor specifications (Adapted from: [16])

Parameter		**Value**	**Unit**
Temperature	T_1	4-20	K
	T_2	45-80	K
	T_3	293	K
Mass	m_1	500	kg
	m_2	200	kg
	m_3	2300	kg
Frequency (in-plane)	f_1	0.5	Hz
	f_2	40	Hz
	f_3	125	Hz
Frequency (out-of-plane)	f_1	40	Hz
	f_2	72	Hz
	f_3	155	Hz

The rest of the parameters corresponding to the lumped model of Figure 2.3 can be found in Table 2.2. Here it is seen that the balance mass is compliant for the in-plane direction having a natural frequency of $f_1 = 0.5$ Hz and that the internal modes (both in-plane and out-of-plane) occur at $f_2 = 40$ Hz, 72 Hz and $f_3 = 125$ Hz, 155 Hz, degrading stability properties for position control. The key to the mechanical fixation design lies with the trade-off between

stiffness (c_i) and thermal isolation (R_i) as both need to meet requirements but counteract each other as shown in [16].

2.2.2 Demonstrator

A demonstrator setup has been built [16], representing the system concept for the final superconducting planar motor as mentioned above. It is designed to show the working of the SCPM by using a smaller magnet plate (0.4 m by 0.4 m) compared to the full magnet plate (1.5 m by 2.5 m). The design of the demonstrator setup is shown in Figure 2.4 with the cold frame (blue), thermal shield (yellow) and vacuum vessel (grey and green). Furthermore, the magnet plate is visible on the top view and a mover with 3 force coils is depicted, which can be used to generate reaction forces in the x and z-direction when used in shown orientation.

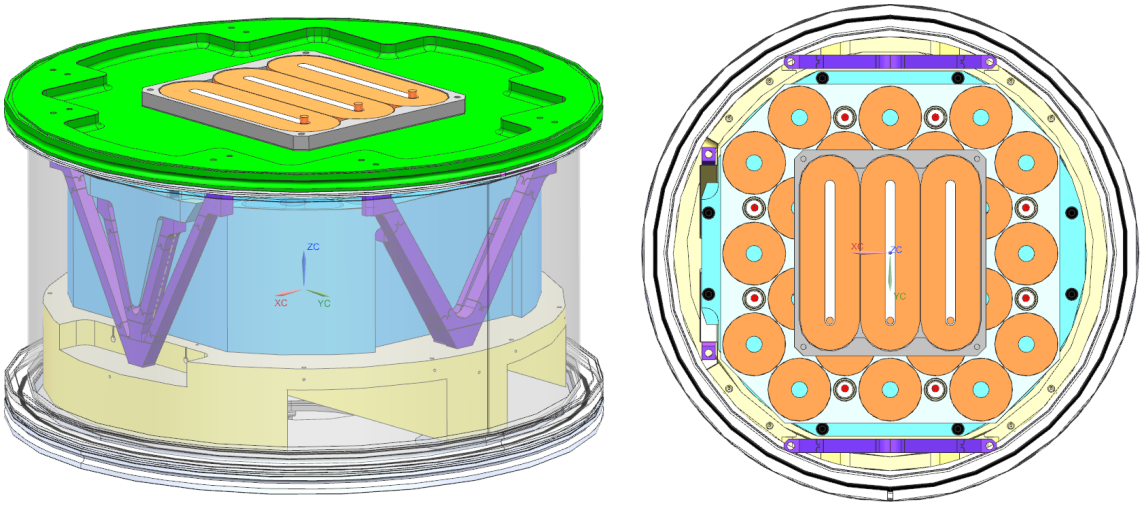

(a) Isometric view (b) Top view

Figure 2.4: SCPM demonstrator setup built in [16] (Note: Some parts of the setup are hidden.)

Besides, the mechanical fixation design is shown (purple) with two times two pairs of struts visible in Figure 2.4a and the location of the 3$^{\text{rd}}$ two pairs of struts in Figure 2.4b. Here, the smaller (inner) pairs of struts are to fixate the coldframe to the isolation frame (c_1) and the second, larger, pairs of struts to fixate the isolation frame to the vacuum vessel (c_2). The V-frames (pair of struts) are designed with a double elastic hinge to increase the stiffness ratios to prevent an overdetermined design [16]. The top and bottom pair of struts on the top view are used to constrain the two translational and two rotational degrees of freedom, while the left pair of struts is used to constraint the two remaining degrees of freedom.

As no fixation design of the vacuum vessel to the machine frame was designed (c_3), the demonstrator setup is analysed as a double mass-spring system with the vacuum vessel clamped to the fixed world. The demonstrator specifications can be found in Table 2.3, which gives the dynamics as shown in Figure 2.5a and Figure 2.5b.

Table 2.3: Demonstrator setup specifications

	Parameter	Value	Unit
Mass	m_1	29.5	kg
	m_2	28.4	kg
Stiffness	c_1	6.7e7	N/m
(x)	c_2	7.4e7	N/m
Stiffness	c_1	2.9e8	N/m
(z)	c_2	2.5e8	N/m
Frequency	f_1	154	Hz
(x)	f_2	399	Hz
Frequency	f_1	294	Hz
(z)	f_2	802	Hz

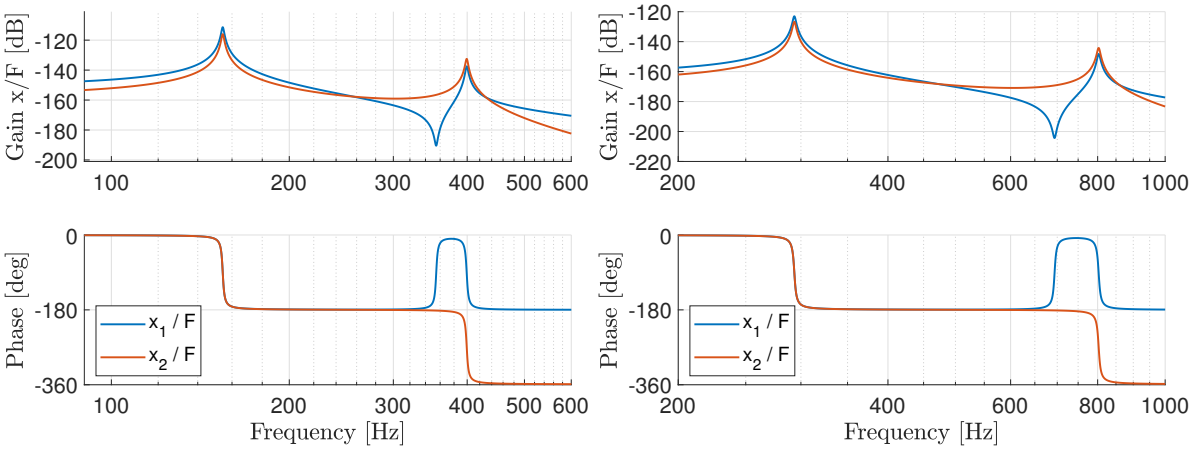

(a) x-direction (b) z-direction

Figure 2.5: Demonstration setup dynamics

The frequency range of the first resonances in the demo setup is a bit higher than specified for the SCPM concept, namely 150 Hz - 300 Hz. However, damping on these modes is still needed to obtain higher system performance, as the resonances degrade the stability properties for positioning control [17]. For this reason, the main objective is to obtain a damping ratio of $\zeta = 0.05 - 0.1$ for the modes occurring in a range of $f = 50$ Hz $-$ 500 Hz for the SCPM concept and demonstrator setup. A second objective is to also target the higher modes and aim for a damping ratio of $\zeta = 0.01$-0.02 for the range of $f = 500$ Hz $-$ 1000 Hz. This results in damping coefficients of $d =$ 2e3 Ns/m $-$ 2e4 Ns/m to be obtained.

CHAPTER 3

Cryogenic damping solutions

Eddy current damping (ECD) and piezoelectric shunt damping came forward in the literature review as potential solutions for passive damping in cryogenic conditions. In this chapter first ECD and then piezoelectric shunt damping is further investigated. It is concluded by a comparison and decision on the most feasible option.

3.1 Eddy current damping

Eddy current damping (ECD) is a damping technique based on the dissipation of eddy currents, induced by a relative motion between a permanent magnet (or solenoid) and a conductor. This relative motion can be the conductor moving in the magnetic field or a changing position or strength of the magnetic field source. The time-varying magnetic field induces eddy currents circulating in the conductor and these currents create an opposing magnetic field interacting with the magnets magnetic field. In this way a resistive force to the original motion is created. The mechanical energy is transformed into heat, leading to mechanical damping.

It is possible to divide this damping principle into two cases, where the source is fixed and the conductor moves or the conductor is fixed and the source has a motion/change of magnetic field. It is shown that the damping-per-volume efficiency of a moving conductor is higher for both rectangular and circular ECD systems in almost all realistic situations [21]. Therefore, only the case of a moving conductor will be considered.

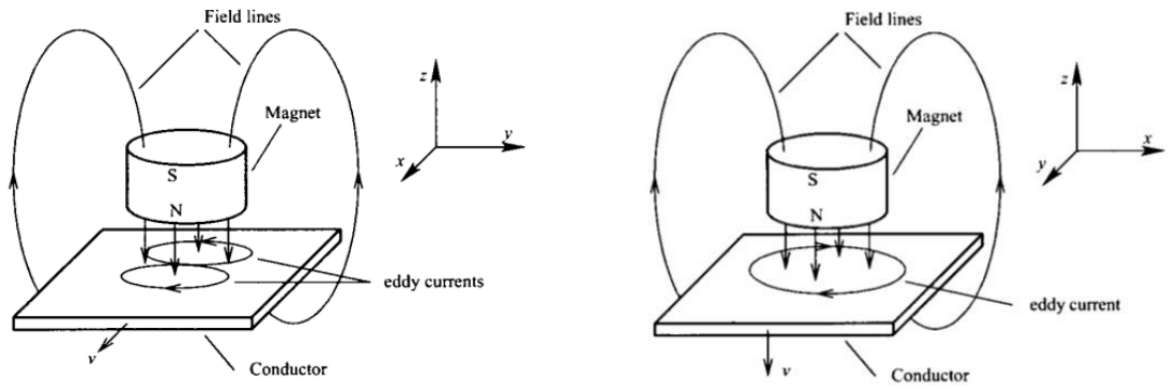

(a) perpendicular moving conductor (b) parallel moving conductor

Figure 3.1: Schematic depiction of eddy current principle (Source: [22])

A second division can be made into perpendicular movement and parallel movement of the conductor with respect to the polar configuration of the magnet as is depicted in Figure 3.1a and Figure 3.1b. This can also be seen as respectively an axial and radial principle, which is based on the magnetic flux direction that induces the eddy currents.

The perpendicular principle is widely used for magnetic braking systems in vehicles, roller-coasters and elevators [23]. It is also used in tuned mass dampers in large buildings [24], for a scanning tunnelling microscope [25] and for a vibration isolation system for a space shuttle payload [26]. Another study regarding eddy current damping is for the suppression of lateral vibrations of rotor shafts of cryogenic turbo-machinery [2][3]. The parallel principle is studied by Sodano et. al. in [27] and [28], but not widely used in applications yet. However, in literature the principle seems to find its first broader application in the magnetic levitation above superconducting material [29][30]. Examining ECD in literature suggests the perpendicular principle to be more commonly used, which is more practical to implement as the conductor remains at a constant distance to the source.

ECD has two interesting properties, first of all the force is proportional to the velocity or frequency of the moving conductor, which makes it behave as a viscous damper. Secondly, the damping effect is higher for lower temperatures. The damping coefficient varies inversely to the resistivity of a conductor moving in the magnetic field and the resistivity of a conductor significantly decreases for lower temperatures, which benefits for applications that require damping at low temperatures.

3.1.1 Modelling

To get to an analytical model, first an expression for the induced eddy current must be obtained based on Faraday's law of induction. The current density for a conducting medium moving in a reference frame can be written as,

$$\boldsymbol{J} = \sigma(\boldsymbol{E} + \boldsymbol{v} \times \boldsymbol{B}) \tag{3.1}$$

with σ the conductivity of the material and $\boldsymbol{E}$ the electrostatic field induced within the conductive sheet along the edges [3][27][31]. Here $\boldsymbol{v} \times \boldsymbol{B}$ is the electro-motive force (an electric action, produced by a non-electric source) driving the eddy currents, with $\boldsymbol{v}$ the velocity of the moving conducting medium and $\boldsymbol{B}$ the magnetic field. Due to Lenz's law, the eddy currents will produce a force opposing the direction of motion, based on the Lorentz force

$$\boldsymbol{F} = \int_V (\rho \boldsymbol{E} + \boldsymbol{J} \times \boldsymbol{B}) \mathrm{d}V \tag{3.2}$$

where the volume integral is taken over the pole projection area of the magnetic field on the conductor. The electrical force component $\boldsymbol{E}$ is neglected by [27] and [31], under the assumption that surface charges can be ignored. This leaves the following expressions for the force in orthogonal directions

$$\begin{bmatrix} F_x \\ F_y \\ F_z \end{bmatrix} = \sigma \int_V \left(\begin{bmatrix} B_z(B_x v_z - B_z v_x) - B_y(B_y v_x - B_x v_y) \\ B_x(B_y v_x - B_x v_y) - B_z(B_z v_y - B_y v_z) \\ B_y(B_z v_y - B_y v_z) - B_x(B_x v_z - B_z v_x) \end{bmatrix} \right) \mathrm{d}V \tag{3.3}$$

For the parallel movement, the velocity in x- and y-direction is assumed zero (i.e. $v_{x,y} = 0$), leaving the damping force to

$$F_z = \sigma \int_V \left(-(B_x^2 + B_y^2)v_z\right) \mathrm{d}V \tag{3.4}$$

Changing to polar coordinates leaves the integral for the damping constant to

$$d_z = 2\pi\sigma \int_0^h \int_0^{r_c} -rB_r^2(r,z)\mathrm{d}r\mathrm{d}z \tag{3.5}$$

with r_c the equivalent radius, and h the height of the conductor. For the perpendicular movement a similar derivation for the damping constant can be done, where the velocity in z-direction is assumed zero (i.e. $v_z = 0$). This leaves the damping constant for respectively x- and y-direction to

$$d_x = \sigma \int_V -(B_z^2 + B_y^2)\mathrm{d}V \tag{3.6}$$

$$d_y = \sigma \int_V -(B_z^2 + B_x^2)\mathrm{d}V \tag{3.7}$$

Analytical integration of Equation 3.5 - 3.7 becomes too complex, as the magnetic flux density B_i depends on the positions over which is integrated. Therefore, numerical integrations methods will be used. First the problem will be converted to 2D, by choosing a cylindrical magnet and using the polar coordinates to define the problem as axi-symmetrical. The resulting 2D configuration can be seen in Figure 3.2, where the vertical axis is the axis of symmetry. The magnetic flux density is obtained using a Finite Element Method program for magnetics [32] and numerical integration is used to calculated the total magnetic flux density of the conductor volume. These results are verified using the analytical expressions of the magnetic flux density for cylindrical magnets from [33]. The resulting magnetic flux density can be found in Figure 3.2. A samarium-cobalt (SmCo, $B_r = 1.2$ T) magnet of relatively large size ($r = 9$ mm, $h = 10$ mm) is used to set the properties of the cylindrical magnet.

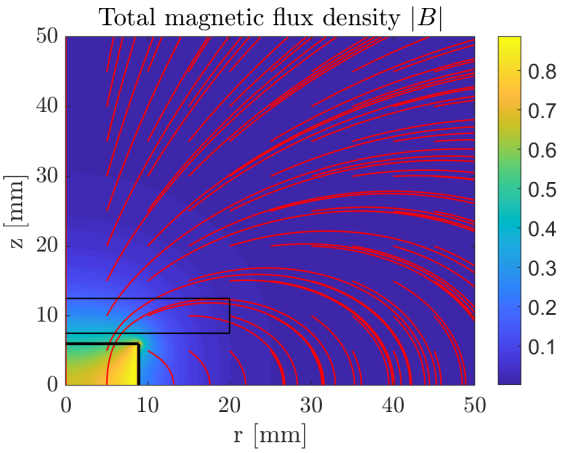

Figure 3.2: Magnetic flux density of a cylindrical, axially polarized magnet

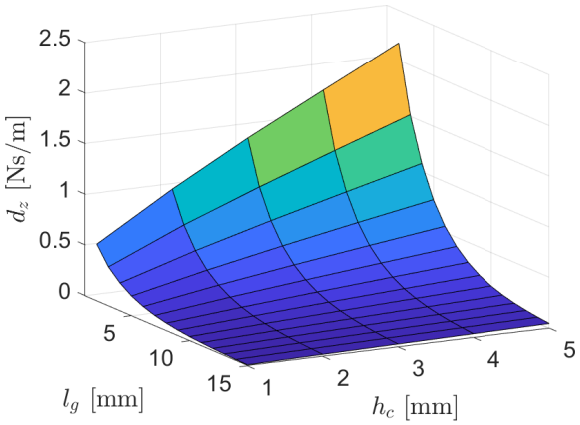

Figure 3.3: Damping constant for varying gap l_g and conductor height h_c @ RT

The total magnetic flux in the conductor volume is analysed for different conductor heights (h_c) and varying gap between magnet and conductor (l_g) and depicted in the form of the

damping constant at room temperature in Figure 3.3. Here it can be seen that the largest total magnetic flux in the conductor is obtained for a conductor with more height, placed as close to the magnet as possible. A damping constant of $d_z = 2.17$ Ns/m is found for a gap of $l_g = 2$ mm and conductor height of $h_c = 5$ mm, which are seen as feasible dimensions for practical implementation. Considering the desired damping constants in the range of $d = 2e3$ Ns/m to 2e4 Ns/m it seems that eddy current damping is not a feasible damping solution at room temperature.

3.1.2 Cryogenic effect

The low performance at room temperature is not a surprise, ECD is known as a damping solution with relatively low damping performance. It could benefit greatly though from operating at cryogenic temperatures, as its principle relies on the electrical conductivity, which is known to increase significantly for lower temperatures. To see if ECD is a viable solution for cryogenic applications, the analysis is continued for lower temperatures. In Figure 3.4 the electrical conductivity of copper for cryogenic temperatures can be found. Here it is seen that the conductivity will increase a factor 10 from RT to $T = 80$ K and a factor 1000 to $T = 4$ K. The resulting improvement for the damping constant is shown in Figure 3.5, which is very promising as the damping constant rises to $d_z = 1860$ Ns/m.

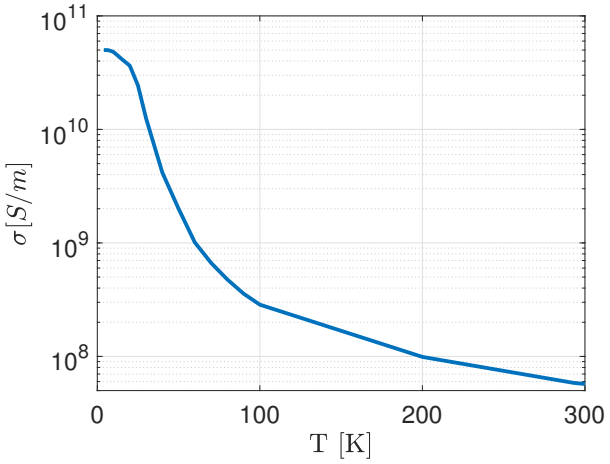

Figure 3.4: Electrical conductivity of copper for low temperatures (Adapted from: [34])

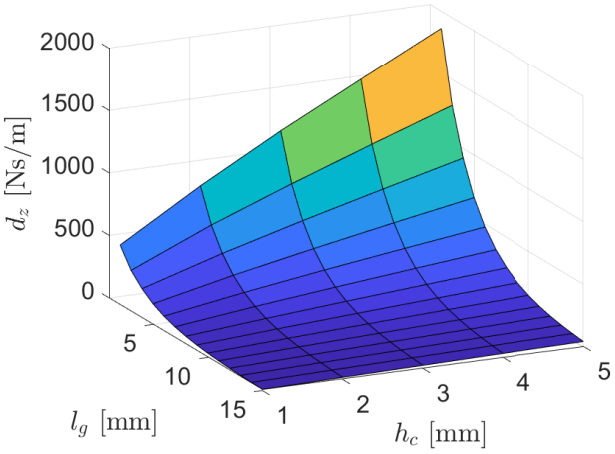

Figure 3.5: Damping constant for varying gap l_g and conductor height h_c at $T = 4$ K

3.1.3 Model improvement

Generally assumptions are made to simplify the ECD modelling, with the main assumption being a thin enough conductor plate in order to be able to neglect the skin effect. Secondly, mutual inductance is ignored for most applications when frequencies will remain below a certain level ($f < 100$ Hz). Both will be investigated to get better insight in the true damping performance for the application.

Skin effect

Taking the skin effect into account could reduce the conductor's effective cross-section and thus increase its effective resistance. The skin effect is expressed by the penetration depth (or skin depth) which characterizes the depth of penetration of the currents into the surface. With one unit of skin depth, the current density is reduced to e^{-1} ($\approx 37\%$), showing that most of the current resides in the skin. The skin depth can be computed by

$$\delta_s(\sigma, f) = \frac{1}{\sqrt{\pi f \mu \sigma}} \tag{3.8}$$

where μ is the permeability of the material, which is equal to the magnetic constant in vacuum (μ_0) for copper [35]. The skin depth as function of conductivity and frequency can be found in Figure 3.6. At low frequency and room temperature the skin depth is considered large enough ($\delta_s > 5$ mm) to neglect its effect when using thin conductor plates ($h_c < 5$ mm). However, when looking at the skin depth at high frequency and cryogenic temperatures ($\delta_s < 0.5$ mm) it is seen that the assumption of thin conductor plates does not hold any longer.

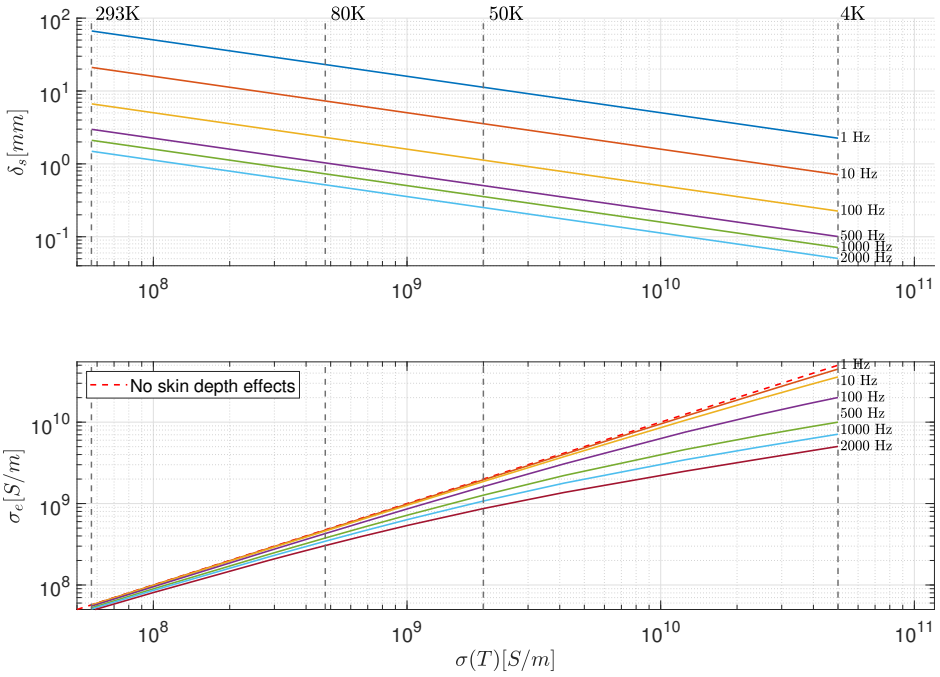

Figure 3.6: Skin depth (top) and effective conductivity (bottom) versus conductivity copper

To take into account the skin depth the effective cross-section is used to correct the volume integral of Equation 3.5 - 3.7. The correction can be made by replacing the conductivity by an effective conductivity, represented by

$$\sigma_e = \frac{2\delta_s}{h_c}\left(1 - e^{-h_c/2\delta_s}\right)\sigma \tag{3.9}$$

The effective conductivity can be found in Figure 3.6. Here it is seen that the conductivity at T = 4 K drops with a factor 2.5 when operating at f = 100 Hz and a factor 10 for f = 1000 Hz. The conductor height is fixed to h_c = 5 mm, to purely show the effect of the

skin depth on the effective conductivity. Taking lower conductor height would increase the effective conductivity, but this is negated by integrating over a smaller height. An overview of application cases is given in Table 3.1. Here it can be seen what the effective conductivity and skin depth will be for these cases. A comparison of the damping performance without taking skin depth into account (d) versus incorporating it (d_{δ_s}) is made.

Table 3.1: skin depth effect and resulting damping performance for different cases.

	f_n [Hz]	T [K]	σ [S/m]	σ_e [S/m]	δ_s [mm]	d [Ns/m]	d_{δ_s} [Ns/m]
SCPM (main)	50	80	4.8e8	4.5e8	3	17.9	16.7
	500	80	4.8e8	3.8e8	1	17.9	14.1
SCPM (side)	500	10	4.8e10	1e10	0.1	1790	372
	1000	10	4.8e10	7e9	0.07	1790	260

It can be observed that the high performance expected before of $d_z \approx 1800$ Nm/s is reduced a factor 6 when taking skin depth into account. The main performance of ECD occurs at low temperatures (T $<$ 50 K), but this is also the range where the effective conductivity decreases the most. Lastly, it can be concluded that higher operating frequencies have a negative effect on the damping performance due to the decreasing penetration depth of the eddy currents. These observations show that the skin effect should be taken into account to properly model the damping performance obtained with ECD. It can also be concluded that a bulky magnet setup is needed to reach the specified damping of $d =$ 2e3 Ns/m to 2e4 Ns/m for the main objective.

Mutual inductance

Besides the effect of the frequency on the penetration depth, a second frequency dependent effect can be observed. This is the effect of mutual inductance (or self- inductance) where the change of the magnetic field induced by the eddy current counteracts itself. Mutual inductance (MI) is generally neglected due to its relatively small contribution compared to the magnetic field of the permanent magnet. Also, neglecting the MI greatly benefits the simplicity of the model.

However, the assumption of small MI is not always valid. This is observed in [27], where a difference between experimental results and the model without MI is seen for higher frequencies. The theoretical model without MI fits the experimental data for lower frequencies, but a mismatch of approximately 2 dB is seen at $f = 170$ Hz and an even higher mismatch of 8 dB at $f = 350$ Hz. More investigation into the modelling of MI is done in [36], which showed that including MI in the model has a large effect on the damping force for frequencies above $f_1 = 100$ Hz. It is thus shown that mutual inductance should be taken into account depending on the specific application.

3.2 Piezoelectric shunt damping

Piezoelectricity is a principle that can convert mechanical energy into electrical energy and vice versa. When a piezoelectric material is under tension or compression it undergoes a potential difference due to the rearrangement of its atoms, the direct piezoelectric effect. The principle can also be reversed, where applying an electric field creates mechanical deformation of the material, which is known as the indirect piezoelectric effect. Both principles are shown in Figure 3.7.

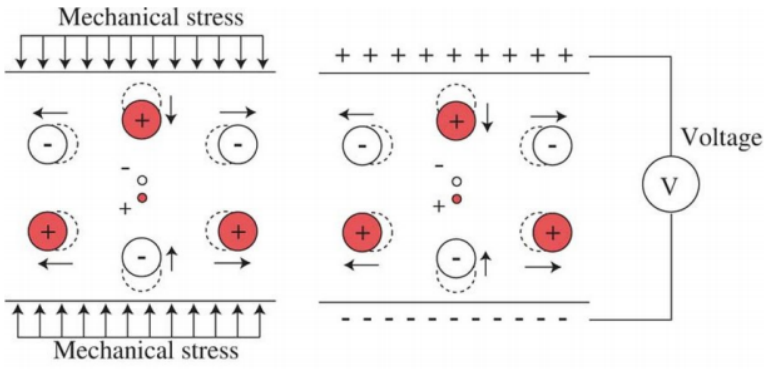

Figure 3.7: Schematic visualization of a Quartz crystal with the direct piezoelectric effect (left) and the indirect piezoelectric effect (right) (Adapted from: [37])

The first effect is commonly used in sensor applications, while the second is used for actuating purposes. The combination of both is a popular method for active vibration control, but in this work the focus only lies on passive damping. For passive damping, the direct piezoelectric effect is used, where the mechanical energy of a vibrating system is converted into electrical energy. By simply adding a resistor to the electric circuit connected to the electrodes of the piezoelectric transducer, energy is dissipated through heat. Another common method is, besides the added resistor, also adding an inductor in series with the resistor to create an extra resonator system. Application of piezoelectric shunt damping can be found in aerospace [38], automotive [39], turbomachinery [40] and optical structures [41]. A schematic overview of a piezoelectric transducer with RL-shunt is given in Figure 3.8.

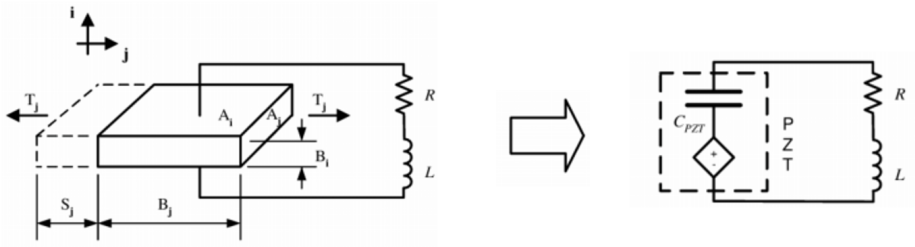

Figure 3.8: Schematic overview of piezoelectric RL-shunt circuit (Adapted from: [42])

The resistor shunt circuit shows viscoelastic behaviour albeit with a lower loss factor and higher stiffness and the RL-shunt behaves similar to a mechanical tuned mass damper [43]. The different damping effects are visualized in Figure 3.9, which also shows the open-circuit and short-circuit situation.

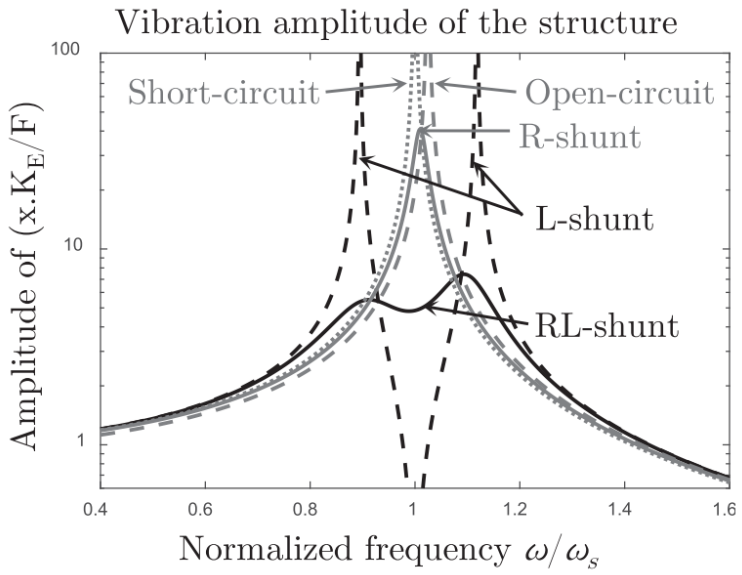

Figure 3.9: Damping effect on a single resonant mode for different circuits (Source: [7])

Observe that the R-shunt provides some damping on the system and the RL-shunt indeed behaves like a tuned mass damper. Because of its superior damping performance, it is decided to make use of the RL-shunt.

3.2.1 1-DoF mass-spring-piezo system

A basic mass-spring-piezo model is used to show the properties of a piezoelectric transducer implemented in a structure. To derive the electro-mechanical equations, the transducer is modelled in series with the spring of a mass-spring system, as shown in the schematic overview of Figure 3.10. x_1 represents the displacement of the mass m_1 and Δ_1 represents the displacement of the piezo-spring connection.

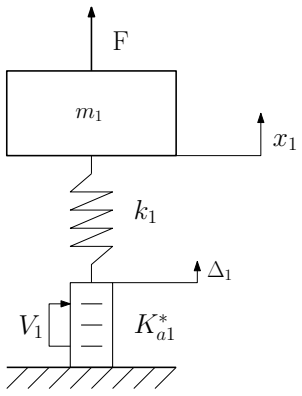

Figure 3.10: 1DOF system with 1 mass

The dynamic equilibrium of the mass gives the mechanical equation of motion based on Newton's second law

$$m_1\ddot{x}_1 = -f_s + F \tag{3.10}$$

with F the external force applied to mass m_1 and f_s the spring force. The spring is connected at attachment point Δ_1 to a multilayer piezoelectric transducer. The force f_{p1} of the transducer, is given by ([44]),

$$f_{p1} = -\frac{nd_{33}K_{a1}^*}{C_1}Q_1 + K_{a1}^*\Delta_1 \tag{3.11}$$

With n the number of ceramic layers in the piezo transducer, d_{33} the piezoelectric constant and C_1 the capacitance. Furthermore, Q_1 is the electric charge and K_{a1}^* is the stiffness of the transducer under constant electric displacement (open circuit),

$$K_{a1}^* = \frac{K_{a1}}{1-k_c^2} \tag{3.12}$$

with K_{a1} the piezo transducer stiffness with constant electric field (short circuit) and k_c the electromechanical coupling factor. By making use of the equilibrium between the piezo force f_{p1} and the spring force f_s and defining the stiffness ratio of the spring k_1 as

$$\gamma_1 = \frac{k_1}{k_1 + K_{a1}^*} \tag{3.13}$$

it is possible to eliminate Δ_1 from Equation 3.11. This results in an expression for the piezoelectric force and thus a new expression for the system of Equation 3.10

$$f_{p1} = -\frac{nd_{33}K_{a1}^*\gamma_1}{C_1}Q_1 + K_{a1}^*\gamma_1 x_1 \tag{3.14}$$

$$m_1\ddot{x}_1 = -K_{a1}^*\gamma_1 x_1 + \frac{nd_{33}K_{a1}^*\gamma_1}{C_1}Q_1 + F \tag{3.15}$$

The piezoelectric behaviour of a multilayer stack is given by ([44]),

$$V_1 = \frac{1}{C_1(1-k_c^2)}Q_1 - \frac{nd_{33}K_{a1}^*}{C_1}\Delta_1 \tag{3.16}$$

Now by defining the stiffness ratio of the transducer K_{a1}^* as,

$$\gamma_2 = \frac{K_{a1}^*}{k_1 + K_{a1}^*}, \tag{3.17}$$

it is possible to express the piezoelectric behaviour as

$$V_1 = \left(\frac{1}{C_1(1-k_c^2)} - \frac{n^2d_{33}^2K_{a1}^*\gamma_2}{C_1}\right)Q_1 - \frac{nd_{33}K_{a1}^*\gamma_1}{C_1}x_1 \tag{3.18}$$

The electromechanical coupling factor k_c can be define and used to simplify the expression

$$k_c^2 = \frac{n^2d_{33}^2K_{a1}}{C_1} \tag{3.19}$$

$$V_1 = \frac{1-\gamma_2k_c^2}{C_1(1-k_c^2)}Q_1 - \frac{nd_{33}K_{a1}^*\gamma_1}{C_1}x_1 \tag{3.20}$$

This makes the total set of system equations together with Equation 3.15, which can be transformed to the Laplace domain resulting in

$$\begin{bmatrix} m_1 s^2 + K_{a1}^* \gamma_1 & -\frac{n d_{33} K_{a1}^* \gamma_1}{C_1} \\ -\frac{n d_{33} K_{a1}^* \gamma_1}{C_1} & \frac{1-\gamma_2 k_c^2}{C_1(1-k_c^2)} \end{bmatrix} \begin{bmatrix} x_1 \\ Q_1 \end{bmatrix} = \begin{bmatrix} F \\ V_1 \end{bmatrix} \tag{3.21}$$

Admittance function

Using the total set of electromechanical equations from Equation 3.21, the properties of the system can be derived. A common way to do this is by deriving the admittance function $Y(s) = I/V$ or the dynamic capacitance $Y(s)/s = Q/V$. By taking $F = 0$ N, the dynamic capacitance can be obtained from Equation 3.21,

$$\frac{Y(s)}{s} = \frac{Q}{V} = C_1(1 - k_c^2)\frac{ms^2 + K_{a1}^* \gamma_1}{ms^2(1 - \gamma_2 k_c^2) + K_{a1}\gamma_1} \tag{3.22}$$

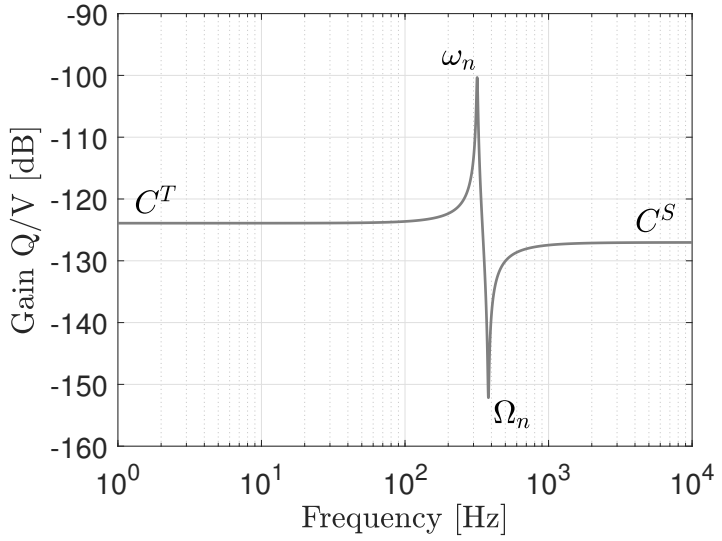

Figure 3.11: Dynamic capacitance of piezoelectric transducer

For the situation with open electrodes, the charge would be blocked, which gives the eigenfrequency of the system as

$$\Omega_n = \sqrt{\frac{K_{a1}^* \gamma_1}{m_1}} \tag{3.23}$$

While for the situation with short-circuited electrodes, the voltage is zero, which gives the eigenfrequency of the system as

$$\omega_n = \sqrt{\frac{K_{a1}\gamma_1}{m_1(1 - \gamma_2 k_c^2)}} \tag{3.24}$$

From the open and short-circuited eigenfrequency, the generalized electromechanical coupling factor can be calculated by ([44])

$$K^2 = \frac{\Omega_n^2 - \omega_n^2}{\Omega_n^2} \tag{3.25}$$

$$K^2 \simeq \frac{k_c^2}{1 - k_c^2}\nu \tag{3.26}$$

The generalized coupling factor is a combination of the structural characteristic (fraction of strain energy ν) and the electromechanical characteristic (coupling factor k_c) of the piezoelectric transducer; it is an indicator for obtainable damping performance. Furthermore, the capacitance can be read from the dynamic capacitance curve. When $\lim_{\omega\to 0}$, the system is mechanically free (constant stress, depicted by T), which leaves

$$C^T = \lim_{\omega\to 0} \frac{Q_1}{V_1} = C_1 \tag{3.27}$$

while with $\lim_{\omega\to\infty}$, the system is mechanically blocked and allows external forces (constant strain, depicted by S), giving,

$$C^S = \lim_{\omega\to\infty} \frac{Q_1}{V_1} = C_1 \frac{1-k_c^2}{1-\gamma_2 k_c^2} \tag{3.28}$$

It is shown that the admittance function is a powerful tool to derive both electrical and mechanical properties, this is useful when quick characterization of the system is needed.

Inductive shunt tuning

The system of Equation 3.21 can be connected to a RL-shunt, modelled by admittance

$$\left(\frac{I}{V}\right)_{\text{shunt}} = -\frac{1}{Ls+R} \tag{3.29}$$

This shunt makes it possible to create a second resonator added to the original system. The equality between the admittance of the shunt and the admittance of the structure of Equation 3.22 gives

$$-\frac{1}{Ls+R} = sC_1(1-k_c^2)\frac{ms^2+K_{a1}^*\gamma_1}{ms^2(1-\gamma_2 k_c^2)+K_{a1}\gamma_1} \tag{3.30}$$

or

$$-\frac{1}{(Ls+R)sC_1(1-k_c^2)} = \frac{ms^2+K_{a1}^*\gamma_1}{ms^2(1-\gamma_2 k_c^2)+K_{a1}\gamma_1} \tag{3.31}$$

The electrical frequency can be defined as

$$\omega_e = \frac{1}{LC(1-k_c^2)} \tag{3.32}$$

and the electrical damping as

$$2\zeta_e\omega_e = \frac{R}{L} \tag{3.33}$$

The inductance can be used to tune the electrical eigenfrequency to the mechanical eigenfrequency and the resistance is tuned to optimize the energy flow such that the dissipated energy is maximized. This is done in a similar fashion as tuning a tuned mass damper, but instead of the mass ratio as a key parameter, the electromechanical coupling factor k_c is used. The analogy between the two was first noted in [43] and studied in [45].

A maximum damping design can be used to maximize the damping of the targeted mode and thus minimizing the response at this mode's eigenfrequency. Another possibility is using the equal peak design, which aims at minimizing the H_∞ norm, i.e. minimizing the maximum

of the frequency response x/F. The tuning rules for the electrical eigenfrequency ω_e and electrical damping ζ_e are given in Table 3.2. The obtainable damping ratio ζ_d with both tuning rules can be expressed as function of the global coupling factor K [46].

Table 3.2: Tuning rules and damping performance for piezo shunt design

Max. damping	**Equal peak**
$\omega_e = \frac{\omega_n}{1-K^2}$	$\omega_e = \frac{\omega_n}{\sqrt{1-K^2}}$
$\zeta_e = K$	$\zeta_e = \sqrt{\frac{3}{8}}K$
$\zeta_d = K/(2\sqrt{2})$	$\zeta_d = K/2$

Damping performance

The system is modelled for $m_1 = 30$ kg, $k_1 = 3e8$ N/m and typical piezoelectric properties are used, which are given in Table 3.3. The damped response of the electromechanical system of Equation 3.31 is shown in Figure 3.12, together with the short circuited and open circuited response of the system.

Table 3.3: Typical piezoelectric properties for axial electric and mechanical quantities $_{33}$.

Parameter	**Variable**	**Value**	**Unit**
Cross section	A	100	mm^2
Thickness	t	250	μm
Number of layers	n	100	-
Coupling factor	k_c	0.71	-
Piezoelectric constant	d_{33}	400e-12	C/N or m/V
Elastic compliance	s_{33}^E	20	$\mu m^2/N$
Dielectric constant	ε^T	1800	-

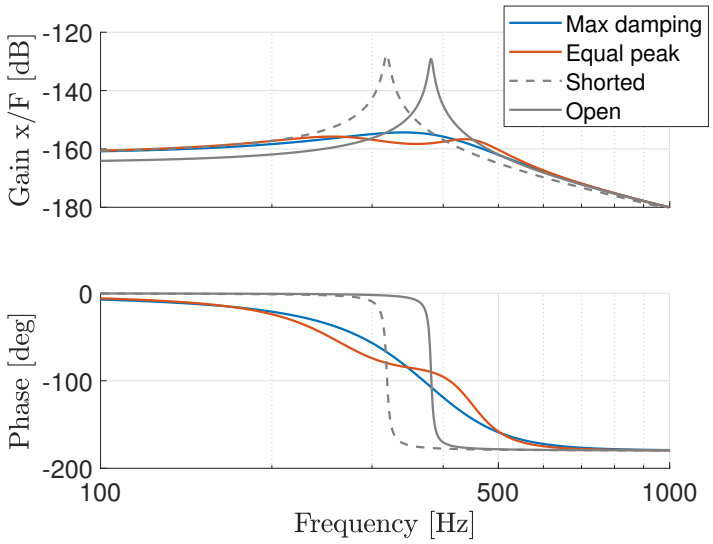

Figure 3.12: Transfer function for 1-DoF mass-spring-piezo system

It can be observed that the open circuited response is at a higher frequency compared to the short circuited response, this is as expected as the electrical boundary conditions influence the stiffness as seen in Equation 3.12. Furthermore, it is seen that the damped response (maximum damping design) has its mechanical eigenfrequency in between the short circuited and open circuited response.

The damping results can be found in Table 3.4, with the obtainable damping ζ_d calculated according to Table 3.2 and ζ_{att} calculated by the attenuation w.r.t. the natural damping of $\zeta_0 = 0.01$. The attenuation is $25 - 28$ dB as can be seen in Figure 3.12, resulting in damping of $\zeta_{att} = 0.182$ for the maximum damping design and $\zeta_{att} = 0.263$ for the equal peak design. The obtained damping is almost equal to the theoretical maximum obtainable damping for both tuning rules, so the RL-shunt was tuned properly.

Table 3.4: Damping performance for different tuning rules.

	$\boldsymbol{K}$	$\boldsymbol{\zeta_d}$	$\boldsymbol{\zeta_{att}}$
Max. damping	0.547	0.194	0.182
Equal peak	0.547	0.275	0.263

3.2.2 1-DoF double mass-spring-piezo system

After the basics are formulated for the single mass-spring-piezo system, the system matrix for a double mass-spring-piezo is derived. This configuration is the closest to the SCPM when the vacuum vessel is clamped to the fixed world. A schematic depiction of this system is given in Figure 3.13. The derivation of the electromechanical equations is similar to that of the single mass-spring-piezo system and can be found in Appendix A.

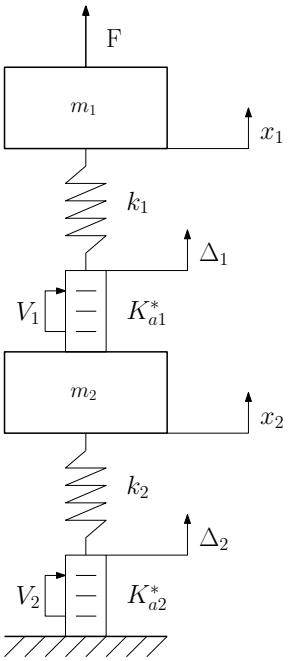

Figure 3.13: 1-DoF system of a double mass-spring-piezo configuration

The connection point between the spring and the transducer is modelled by the displacement Δ_i and the electric potential over the transducer electrodes is given by V_i. The system overview is shown in Figure 3.13. The system matrix in the Laplace domain is derived in Appendix A as

$$\begin{bmatrix} m_1 s^2 + K_{a1}^* \gamma_{11} & -K_{a1}^* \gamma_{11} & -a_1 & 0 \\ -K_{a1}^* \gamma_{11} & m_2 s^2 + K_{a1}^* \gamma_{11} + K_{a2}^* \gamma_{12} & a_1 & -a_2 \\ -a_1 & a_1 & b_1 & 0 \\ 0 & -a_2 & 0 & b_2 \end{bmatrix} \begin{bmatrix} x_1 \\ x_2 \\ Q_1 \\ Q_2 \end{bmatrix} = \begin{bmatrix} F_1 \\ F_2 \\ V_1 \\ V_2 \end{bmatrix} \tag{3.34}$$

with

$$a_i = \frac{n_i d_{33} K_{ai}^*}{C_i} \gamma_{1i}, \qquad b_i = \frac{1 - \gamma_{2i} k_{ci}^2}{C_i (1 - k_{ci}^2)} \tag{3.35}$$

Shunt system

As there will be multiple transducers implemented into the structure, it is possible to distinguish between the different transducers by using the ***specific*** *generalized electromechanical coupling* factor which is given as ([45])

$${}^l K_m^2 = \frac{{}^l \Omega_m^2 - \omega_m^2}{{}^l \Omega_m^2} \simeq \frac{k_c^2}{1 - k_c^2} {}^l \nu_m \qquad \text{for} \quad l = 1, 2, ..., N \tag{3.36}$$

where ${}^l \Omega_m$ depicts the natural frequency of mode m when all transducers are short-circuited except for the l^{th} transducer while ω_m gives the natural frequency when all transducers are short-circuited. The fraction of strain energy corresponding to this transducer in the structure is depicted by ${}^l \nu_m$. The poles of the admittance function ${}^l Q / {}^l V$ are located at ω_m while the zeros are located at ${}^l \Omega_m$. Furthermore, the ***global*** *generalized coupling factor* is defined as ([44])

$$K_m^2 = \frac{\Omega_m^2 - \omega_m^2}{\Omega_m^2} \tag{3.37}$$

For the simplicity of the dynamical model, only K_m will be used and therefore from now on referred to as the generalized coupling factor. This is possible under the assumption that:

- All transducers tuned for the same mode have the same fraction of strain energy ${}^l \nu$
- All transducers tuned for the same mode have the same coupling factor k_c
- The variation of the mode shapes is marginal and assumed unchanged for simplicity.

By these assumptions the generalized coupling factor will become

$$K_m^2 \approx \frac{k_c^2}{1 - k_c^2} \sum_{l=1}^{N} {}^l \nu_m = N \, {}^l K_m^2 \tag{3.38}$$

The generalized coupling factor is used for the tuning of the shunt circuit according to the maximum damping design by using the (approximated) tuning rules ([47])

$$L_i \approx \frac{1}{\omega_m^2 C_{static}} \tag{3.39}$$

$$R_i \approx \frac{2K_m}{\omega_m C_{static}} \tag{3.40}$$

The maximum damping that can be obtained with this RL-shunt is expressed by

$$\zeta_d \approx \frac{K_m}{2\sqrt{2}} \tag{3.41}$$

To decide which transducer will be used to damp each mode, the fraction of strain energy in the transducers and in the V-frames per mode are calculated by respectively

$$\nu_{i,m}(K_a^*) = \frac{K_{ai}^*(b^T \Phi_m \gamma_{1i})^2}{\Omega_m} \tag{3.42}$$

$$\nu_{i,m}(k) = \frac{k_i(b^T \Phi_m \gamma_{2i})^2}{\Omega_m} \tag{3.43}$$

where b^T is a projection vector, used to obtain the relative displacement of the masses. The resulting strain energies are displayed in Table 3.5. Here it can be seen that there is more strain energy in the second transducer for mode 1 and more in the first transducer for mode 2. This is as expected based on the mode shapes of the SCPM. More strain energy means more mechanical energy that can be converted into electrical energy, for this reason it is chosen to use the transducer p_1 for mode 2 and p_2 for mode 1.

Table 3.5: Fraction of strain energy for piezo transducers and V-frames

↓ Mode	Piezo transducer		V-frame		Total
Strain energy →	1	2	1	2	$\Sigma\nu_{i,m}$
Mode 1 ($\nu_{i,1}$)	0.094	0.239	0.189	0.487	1.01
Mode 2 ($\nu_{i,2}$)	0.241	0.093	0.472	0.188	0.99

A value for K_m using Equation 3.37 is needed before it is possible to tune the system using the tuning rules. For each transducer and each mode, the short- and open circuited eigenfrequencies are therefore obtained by making use of the electrical boundary conditions of Table 3.6, e.g. to obtain ω_1 the used transducer p_2 is short-circuited and the unused transducer p_1 is also short-circuited. Elaboration on this can be found in Appendix A.

Table 3.6: Boundary conditions when targeting multiple modes

	p_2		p_1	
↓ Transducer set	**Mode 1** (K_1)		**Mode 2** (K_2)	
Obtained →	ω_1	Ω_1	ω_2	Ω_2
p_2	Short	Open	Open	Open
p_1	Short	Short	Short	Open

System performance

After obtaining the open and short-circuit eigenfrequencies and tuning the shunt according to Equations 3.39-3.40, the damping performance can be analysed. The x_1/F_1 transfer functions can be found in Figure 3.14 representing the superconducting planar motor dynamics in x-direction. The system is displayed for both the open and short-circuited transducers, with

a natural damping of $\zeta_0 = 0.01$ and the system damped with a RL-shunt. The response in z-direction can be found in Appendix A.

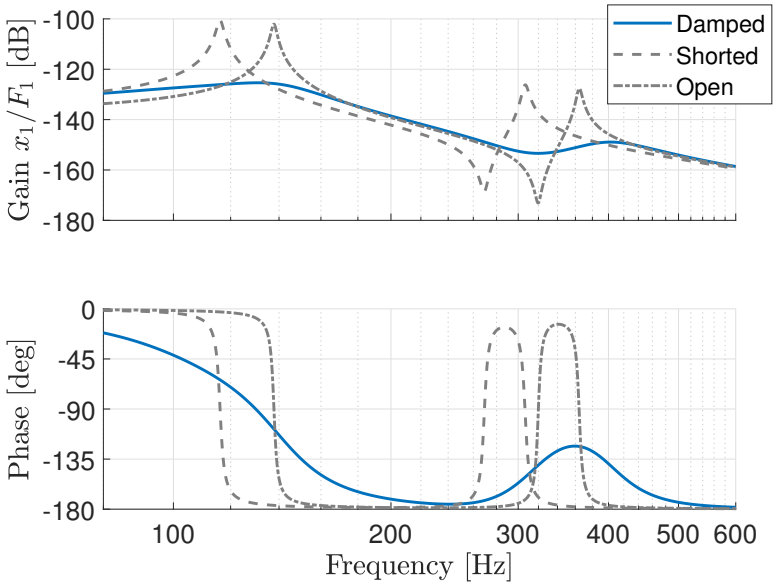

Figure 3.14: Compliance x_1/F_1 in x-direction for 1-DoF double mass-spring-piezo system.

The resulting generalized coupling factor can be found in Table 3.7 together with the maximum obtainable damping and the realized damping. It is seen that a damping of $\zeta_{att} = 0.109$ is obtained at RT for the first mode in x-direction.

Table 3.7: Damping performance for 1-DoF double mass-spring-piezo system in x-direction

	$\boldsymbol{K_m}$	$\boldsymbol{\zeta_d}$ [%]	$\boldsymbol{\zeta_{att}}$ [%]
Mode 1 (p_1)	0.406	14.3	10.9
Mode 2 (p_2)	0.407	14.4	9.0

The obtained damping ζ_{att} is however not equal to the maximum obtainable damping performance ζ_d of Equation 3.41. The difference can occur due to the approximation that is used for tuning the shunt circuit. A second explanation is that the eigenfrequencies Ω_m, ω_m are derived without knowing the exact impedance of the other transducers as shown in Appendix A, creating an uncertainty for both the tuning and the theoretical maximum obtainable damping. Furthermore, adding the piezo transducer in series with the original spring adds compliance to the system, which causes the eigenfrequency of the original system ($f_1 = 154$ Hz, see Figure 2.5a) to decrease to $f_1 = 140$ Hz.

3.2.3 Cryogenic behaviour

The next step is to update the model for cryogenic conditions. As the damping performance is indicated by the generalized coupling factor K_i (see Equation 3.41), it is of interest to have a closer look at it as function of temperature. The generalized coupling factor consists of an electromechanical part (k_{ci}) and a structural part ($\nu_{i,m}$) as can be seen in Equation 3.38. Here, the coupling factor k_{ci} depending on three main parameters can be defined as

$$k_{ci} = \frac{d_{33}}{\sqrt{\varepsilon_{33}^{T} s^{E}}} \tag{3.44}$$

The change of these three parameters as function of temperature is studied together with the total change in k_{ci} ($= k_{33}$). Studying the temperature effect on the fraction of strain energy $\nu_{i,m}$ (see Equation 3.42) is more complicated, as it depends on the structure it is operating in. When assumed that the mode shape Φ_m will not change for different temperatures it follows that the fraction of strain energy, given by Equation 3.42, mostly depends on the stiffness ratio γ_{1i}. So comparing the temperature dependent stiffness change of the titanium V-frame to the elastic compliance of PZT will give insight in the structural component.

Piezoelectric properties in literature

Lead zirconate titanate (PZT) is one of the most used piezoelectric materials [48], so the main focus lies on this material. Especially on the PZT navy types II and V which are 'soft' grades and exhibit higher electromechanical coupling factors. In Figure 3.15 the decreasing piezoelectric constant and dielectric constant can be found, which have respectively a decreasing and increasing effect on the coupling factor k_{33}. Values are obtained at temperatures of interest and summarized in Table 3.8.

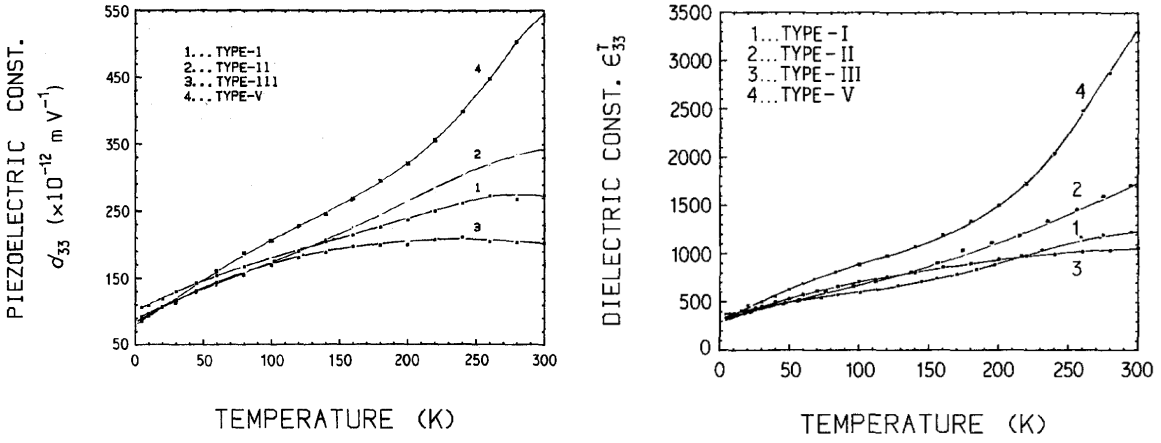

Figure 3.15: Piezoelectric properties tested for cryogenic temperatures with piezoelectric constant d_{33} (left) and dielectric constant ε_{33}^{T} (right) (Source: [49])

Unfortunately there is no experimental data on the elastic compliance s^E for the full temperature range. An elastic test on PZT EC-65, equivalent to PZT type II, has been conducted in the range of $T = 108$ K $- 473$ K in [50]. The results can be found in Figure 3.16, where it is seen that the elastic compliance drops from $s^E \approx 18.5$ μm^2/N at $T = 293$ K to $s^E \approx 15.5$ μm^2/N at $T = 108$K. The elastic compliance for lower temperatures is extrapolated from this data as a first estimate, to be $s^E = 15$ μm^2/N at $T = 80$ K and $s^E = 13.7$ μm^2/N at $T = 4$ K. This is assumed to be a good indication, as it is observed that no phase changes will occur for the soft grades below $T = 200$ K, based on the behaviour of the piezoelectric and dielectric constant.

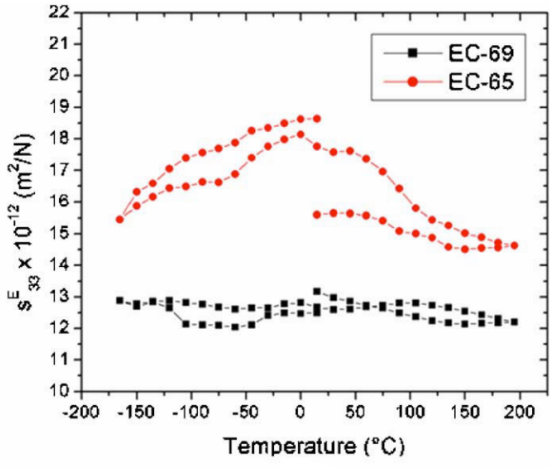

Figure 3.16: Elastic compliance s^E for cryogenic temperatures (Source: [50])

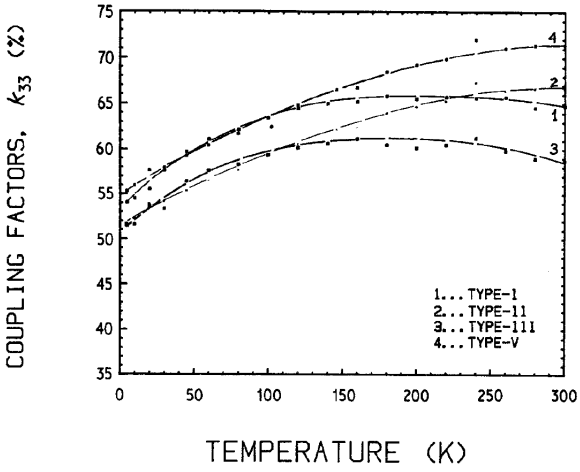

Figure 3.17: Coupling factor k_{33} for cryogenic temperatures (Source: [49])

Data on electromechanical coupling factor k_{33} is also available and can be found in Figure 3.17. Here it is seen that for Type II, the coupling factor shifts from $k_{33} = 0.67$ to 0.58 to 0.52 for respectively $T = 293$K, 80K and 4K. This is a decrease of respectively 13% and 22%. Extra data on the elastic compliance is obtained using the coupling factor k_{ci}, d_{33} and ε^T_{33} via Equation 3.44 and can be found in Table 3.8.

Table 3.8: Parameters used for piezo stack.

Property		293K	80K	4K
k_{33} [-]	II	0.67	0.58	0.52
	V	0.71	0.62	0.55
d_{33} [pm/V]	II	340	160	90
	V	530	190	90
ε^T_{33} [-]	II	1700	600	350
	V	3200	800	350
s^E [$\times 10^{-12}$m^2/V]	II[1]	18.5	15	13.7
	II[2]	17.1	14.3	9.67
	V[2]	19.7	13.3	8.64

It must be said that besides the different PZT types also materials classified under a certain type can differ from each other, with slightly different electromechanical properties as a consequence. For this reason there are different values specified by common piezo suppliers of which more details can be found in Section 4.1.1. More literature studies substantiates the findings on the cryogenic properties [10][11][51], albeit not as all-encompassing as in [49].

[2]Calculated with Equation 3.44 and data of Figure 3.15 and Figure 3.17.
[1]Interpolating from data on EC-65 in Figure 3.16.

Cryogenic system performance

To analyse the damping performance at cryogenic temperatures, the piezoelectric parameters (type II of Table 3.8) are implemented in the dynamic model together with the elastic modulus for Ti-6Al-4V for different temperatures [52]. The resulting system with the shunt connected can be seen in Figure 3.18, where the frequency is shifted due to the decreased elastic compliance.

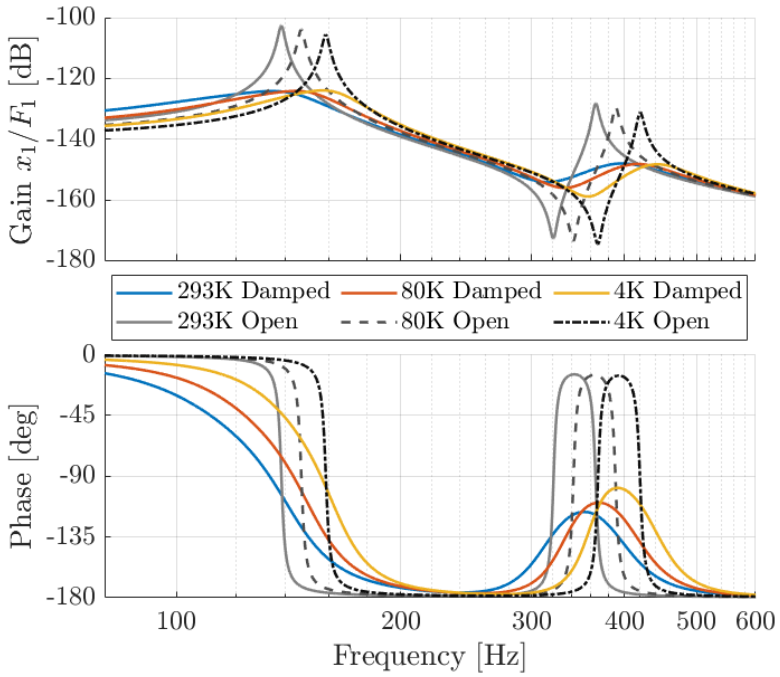

Figure 3.18: Transfer function x_1/F_1 in x-direction for different temperatures

The resulting damping performance at different temperatures can be found in Table 3.9. When comparing to room temperature, it is seen that the realized damping ζ_{att} is decreased 15.6% and 33.0% at $T = 80$ K and $T = 4$ K. This effect is directly related to the decrease in electromechanical coupling factor k_{ci}, which is similar. The fraction of strain energy remains similar as the decrease in elastic compliance for PZT and Ti-6Al-4V do not differ much (both decrease 10-20%). Furthermore, it is observed that the attainable damping ζ_d decreases similarly to the realized damping.

Table 3.9: Cryogenic damping performance for 1-DoF double mass-spring-piezo system

	Temp. [K]	k_{ci}	K_m	ζ_d [%]	ζ_{att} [%]
Mode 1	293	0.67	0.41	14.3	10.9
	80	0.58	0.35	12.4	9.2
	4	0.52	0.28	10.0	7.3
Mode 2	293	0.67	0.41	14.4	9.0
	80	0.58	0.35	12.4	8.0
	4	0.52	0.29	10.1	6.4

3.3 Conclusion

It is concluded that eddy current damping is less viable to use for SCPM application, as the operating conditions are not favourable. For temperatures $T > 50$ K and frequencies $f > 100$ Hz, the damping performance of ECD is significantly less compared to temperatures $T < 10$ K and frequencies $f < 10$ Hz.

This is mainly because the strong increase in conductivity of copper only occurs at $T < 50$ K. But it is also seen that the skin effects of the eddy currents occurring due to the low temperature and high frequency deteriorate the damping performance. Another effect deteriorating the damping performance for the application is the mutual inductance, which is also due to the operating frequencies of $f > 100$ Hz.

For piezoelectric damping, it is needed to model the system in more detail to obtain insight in strain energy distribution over the structure. It is shown that the piezoelectric transducers can have significant strain energy when implemented in series with the flexure-based V-frames. This, in combination with the wide presence of piezoelectric shunt damping applications in literature [7][8], shows the feasibility of using piezoelectric damping at room temperature.

It is seen that the damping performance of piezoelectric damping relies on the fraction of strain energy (structural component) and the piezoelectric coupling factor (piezoelectric property). The fraction of strain energy will not change significantly with temperature as long as the elastic modulus of the structural materials have the same temperature dependency as PZT. So the main dependence of damping performance as function of temperature lies with the piezoelectric properties.

By comparing the piezoelectric properties ($d_{33}, \varepsilon_{33}^T, s_{33}^E$ and most importantly k_{33}) between room temperature and cryogenic temperatures it is shown that the reduction in damping performance is only 15.6% for $T = 80$ K and 33% for $T = 4$ K. Due to these promising results, it is chosen to damp the lower modes of the SCPM by implementing piezoelectric transducers in series with the outer V-frames.

CHAPTER 4

Design and implementation

A piezoelectric transducer will be selected, followed by its implementation in the demonstrator setup. After this, the variable RL circuit will be designed for shunt-tuning. The chapter is concluded by analysing the dynamic behaviour of the system with transducers implemented.

4.1 Transducer design

The piezoelectric transducer is selected in order to maximize its damping capability, and thus its generalized electromechanical coupling factor for the m^{th} mode

$$K^2 = \frac{k_c^2}{1-k_c^2}\frac{K_{ai}^*(b^T\Phi_m\gamma_{1i})^2}{\Omega_m^2} \tag{4.1}$$

The first part of the expression only contains the coupling factor k_c, being the main parameter for material selection. Almost all parameters of the second part depend on the transducer stiffness and thus on both elastic compliance s^E and geometry. Therefore, after the material selection, the optimal geometry within volume restrictions is obtained.

4.1.1 Material selection

Piezoelectric materials can be divided into several categories, with the most common being ceramics (PZT), single-crystals (PMN-PT, PZN-PT) and polymers (PVDF). Properties of these categories are given in Table 4.1. Material parameters can vary within each category and differ from the values given below, as all manufacturers develop different compositions.

Table 4.1: Material parameters for typical piezoelectric materials

Material type	$\boldsymbol{k_{33}}$ [−]	$\boldsymbol{\varepsilon^T}$ [−]	$\boldsymbol{s^E}$ [μm^2/N]	$\boldsymbol{d_{33}}$ [pC/N]	Source
Multilayer ceramic					
Soft-PZT	0.68-0.75	3000-3800	21-22	400-600	[53][54][55][56]
Hard-PZT	0.50-0.60	1400	16	250-350	[53][55]
Single crystal ceramic					
PMN-PT	0.90-0.95	5300-7000	50-70	1250-1400	[55][56][57][58]
PZN-PT	0.90-0.95	6100	100	2500	[53][56][58][46]
Polymer					
PVDF	0.2-0.3	6-12	1000	-30	[53][55][58]

It is seen that single crystals outperform both multilayers and polymers regarding energy con-

version, having an extremely high electromechanical coupling of $k_{33} = 0.90 - 0.95$, resulting into a damping performance 2-3 times higher compared to the coupling factor of soft-PZT. Furthermore, single crystals have higher dielectric constants ε^T. This increases the capacitance of the piezo, which results into a lower needed inductor value following from Equation 3.39. Lastly, higher elastic compliance s^E lowers the stiffness, increasing the strain energy. Higher compliance could be beneficial for implementation, but depends on the structure it is implemented in regarding volume and stiffness specification.

Based on these observations, PMN-PT or PZN-PT would be the preferred material. Unfortunately, single crystals are hard to grow and therefore way more expensive and not widely available. Besides this, the possibilities regarding geometry are limited and they are more fragile. For this reason, it is chosen to use soft-PZT as a good second option, giving more geometry possibilities and having wider availability. Soft-PZT is outperforming both hard-PZT and polymers on coupling factor and dielectric constant.

4.1.2 Geometry optimization

After material selection, the geometry can be optimized for the given application. The geometry changes the stiffness of the transducer and as a result of this, the fraction of strain energy of the transducer will change. The transducer's stiffness for open circuited electrodes is given by

$$K_{a2}^* = \frac{E^D W^2}{L} \tag{4.2}$$

Where W gives the width of the (square) transducer and L gives its length. Designing for a compliant transducer gives a high fraction of strain energy and thus more damping but also lowers the total stiffness, making the system's eigenfrequency drop. A further breakdown of the global coupling factor K_1 is done to make a good trade-off. Figure 4.1 shows that K_1 increases for lower geometry ratio W/L.

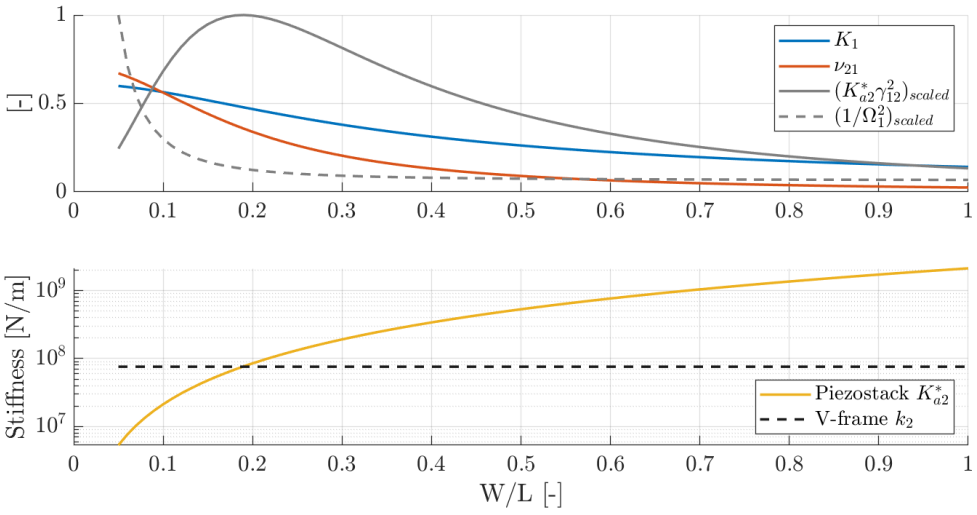

Figure 4.1: Geometry optimization of piezo stack for the first mode ($m = 1$): Decoupling for the fraction of strain energy (top) and stiffness comparison (bottom)

When decoupling the fraction of strain energy ν_{21} into the strain energy in the transducer ($K^*_{a2}\gamma^2_{12}$) divided by the total strain energy (Ω^2_1) it is seen that the increase of ν_{21} mainly comes from the whole system becoming more compliant at a certain point ($1/\Omega^2_1$ increasing significantly for $W/L < 0.2$). This is the point to make the trade-off between damping and stiffness, increasing the damping performance will come at a high cost of lowering the systems natural frequency. An optimum for the strain energy in the transducer is observed around $W/L = 0.2$. As the transducer is implemented in the structure in series with the V-frame, the optimal transducer geometry depends on the V-frame stiffness. In the bottom graph of Figure 4.1 it can be seen that designing for a transducer stiffness equal to the structure stiffness gives an optimal transducer strain energy. In the case of a transducer geometry with ratio $W/L = 0.2$, the total stiffness of the system is reduced with a factor 2.

4.2 Implementation

It is best to implement the transducer in series with the outer V-frames of the demo setup of Figure 2.4, based on the fraction of strain energy in Section 3.2.2. By implementing it in between the two double hinges, the transducers can be used in two directions due to the kinematic design. The design space becomes 15x10x110 mm (HxWxL) which reduces to approximately 15x10x50 mm for the transducer when taking the connection to the V-frame into account. This design space including the final transducer design implemented can be seen in Figure 4.2.

4.2.1 Pre-loading

As piezo stacks consist of multiple ceramic layers stacked on top of each other, it is key to not have tensile stresses in the stack. To compensate for tensile forces, a pre-load can be used to be able to dynamically operate the piezo stack. The recommended pre-load is typically 10-20 MPa and the maximum pre-load is limited to 30-40 MPa [59][60].

Based on the planar motor application, reaction forces up to $F = 12.5$ kN in x-z direction are expected as a result of the forcer coils moving above the superconducting coils [16]. This can give tensile forces up to $F = 1.8$ kN per transducer. Based on the volume restriction, this would be feasible for pre-loading, resulting in a pre-load of 18 MPa when considering $A = 100$ mm^2.

4.2.2 Selected design

Only few suppliers offer piezo stacks which are cryo-compatible. Keeping availability and delivery times in mind, it was decided to go for CTS Corps' plate stack series which fit the cryogenic requirements and have the option for a pre-load mechanism. Coming with a cross section of 5x5 mm, 7x7 mm and 10x10 mm with different lengths. Based on the geometry optimization the 7x7 mm stack with length of 34 mm is selected. The specification of the final pre-loaded transducer stack can be found in Table 4.2 and the transducer itself is shown in Figure 4.3.

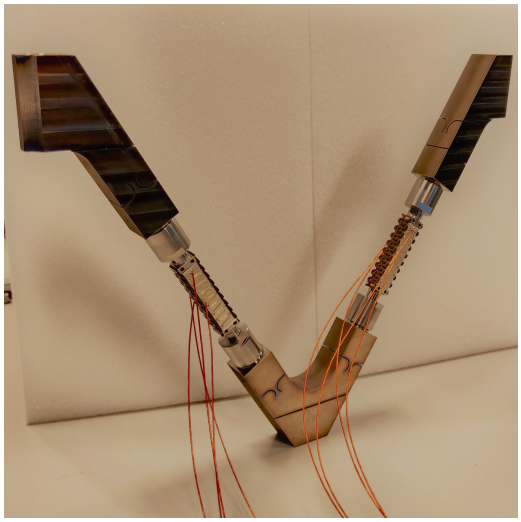

Figure 4.2: Piezo transducer implemented in V-frame

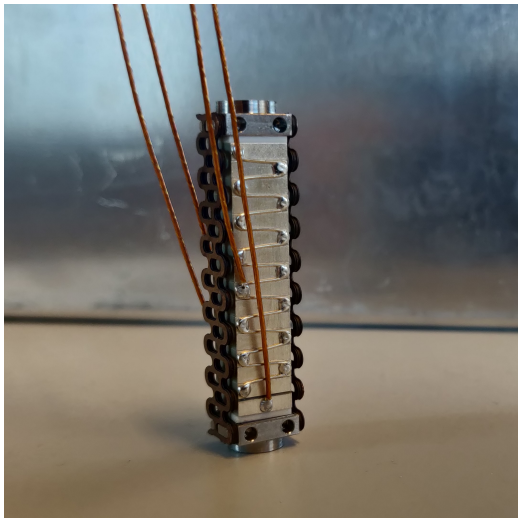

Figure 4.3: NAC2014-H34P piezo transducer with pre-load springs

Table 4.2: Properties of NAC2014-H34P piezo stack

Property	**Variable**	**Value**	**Unit**
Coupling factor [1]	k_{33}	0.74	-
Min. operating temp.	T_{min}	4	K
Height (total height)	H (H_t)	7 (10)	mm
Width (total width)	W (W_t)	7 (8.8)	mm
Length (total length)	L (L_t)	34 (41.5)	mm
Layer thickness	t	500	μm
Free stroke, static	x_{free}	51.2 $\pm$15%	μm
Blocking force, static	F_{block}	2060 $\pm$20%	N
Max. pull force	F_{pull}	500	N
Max. operating voltage	V_{max}	150	V
Capacitance @1V_{RMS},1kHz	C	5470	nF

It can be seen that the maximal pull force is limited to $F_{\text{pull}} = 500$ N, this is due to standard pre-load design for a recommended pre-load of 10 MPa. As the experimental setup will not be tested on full capacity (e.g. 12.5 kN reaction forces), the maximum pull force is sufficient. When desired, a new pre-loading mechanism could be designed to full-fill the $F = 1.8$ kN pre-load requirement.

The connection design is based on clamping a connection pin with an union nut on both sides of the piezo, which can be seen in Figure 4.4. By using a clamped mechanism the orientation can always be corrected for good alignment. It is also possible to demount the piezo element in case of failing. The realized V-frame with implemented piezo transducers can be found in Figure 4.2 and the total of 6 transducers implemented in the setup can be found in Figure 4.5.

[1] This parameter is for bulk material NCE51F, of which further material parameters can be found in [61].

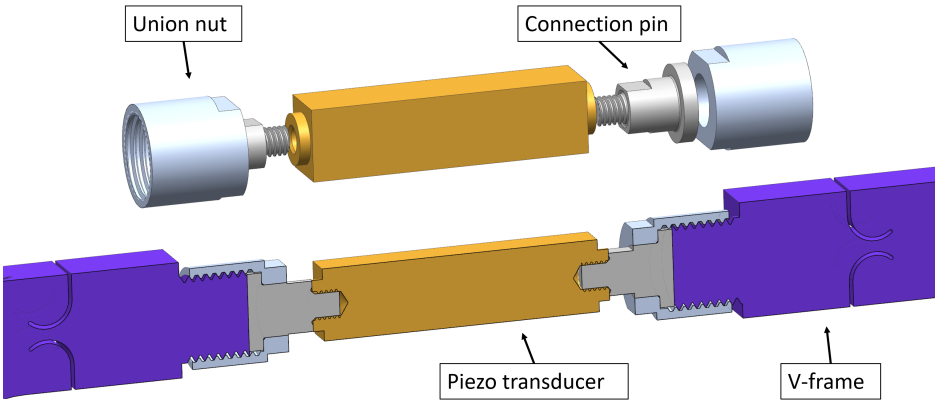

Figure 4.4: Piezo transducer connection to V-frame

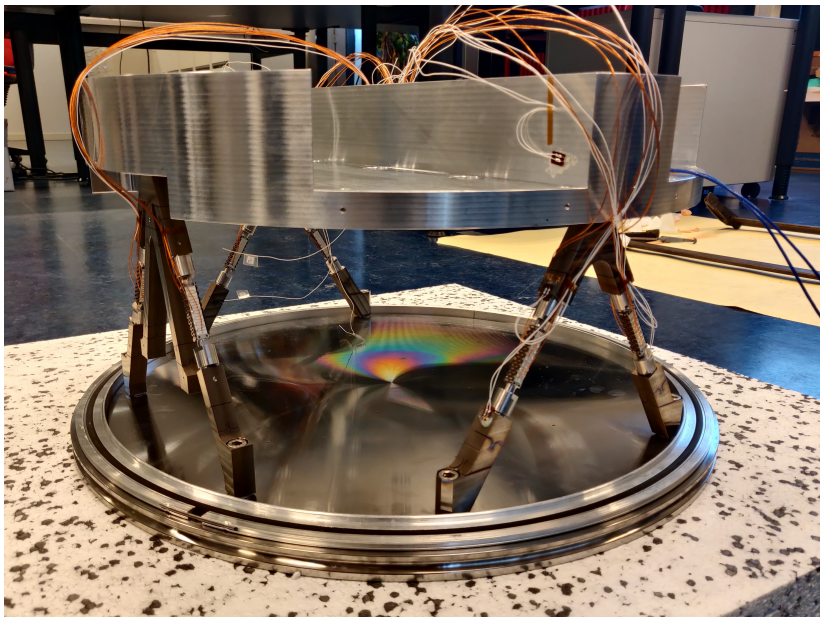

Figure 4.5: Picture of setup with all 6 transducers implemented

4.3 Active inductor - Gyrator

A variable RL-shunt is chosen to tune the electrical resonance, via inductance L_{eq}, and the electrical resistance R directly, both according to the shunt tuning rules described in Section 3.2.2. A synthetic inductor (Antonio circuit [62]) will be used, where the inductance is linearly related to a variable resistance as shown in Equation 4.3 The synthetic inductor is connected in series with a variable resistance of which the schematical overview can be found in Figure 4.6 with component selection according to Table 4.3.

$$L_{eq} = \frac{R_1 R_3 (R_4 + R_5^{var})}{R_2} C_{gyr} \tag{4.3}$$

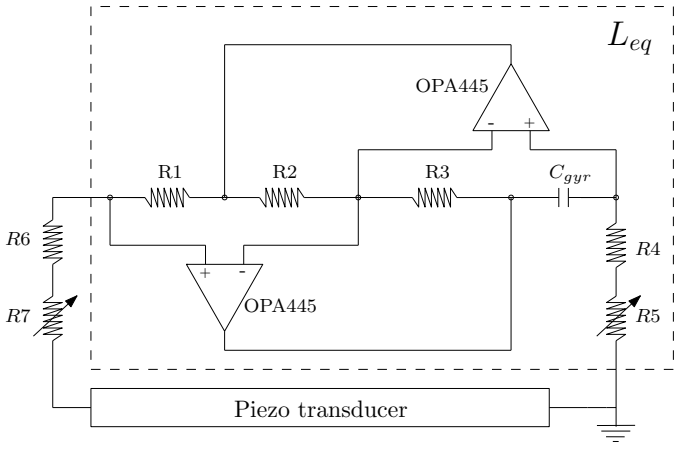

Figure 4.6: Schemetics of RLC circuit

Table 4.3: RLC circuit specifications

Variable	Value
R_1	1 kΩ
R_2	1 kΩ
R_3	1 kΩ
R_4	1 kΩ
R_5^{var}	0-10 kΩ
C_{gyr}	100 nF
R_6	10 Ω
R_7^{var}	0-1 kΩ

The electrical frequency for either blocked or free transducer capacitance can be obtained by

$$\omega_e = \frac{1}{\sqrt{L_{eq}C^i}} \tag{4.4}$$

and is visualized in Figure 4.7, where both the frequency and induction are depicted as function of resistance. The parameters of Table 4.3 are chosen such that the electrical frequency can be tuned in the range of $f = 95 - 230$ Hz when operating at RT. This range will be wider in reality as the capacitance will be in between the free and blocked values.

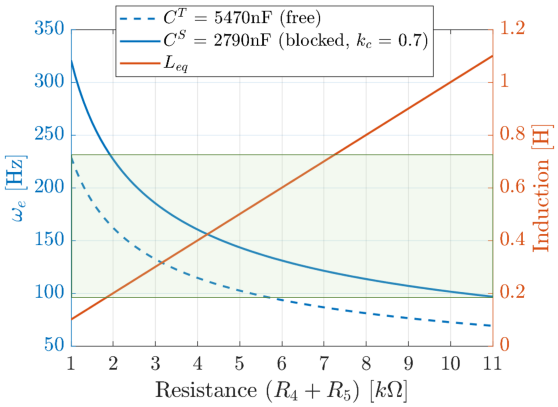

Figure 4.7: Gyrator tuning (293K)

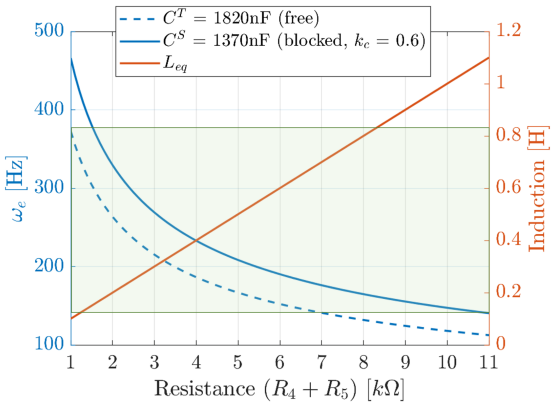

Figure 4.8: Gyrator tuning (77K)

The same is done for the RLC circuit at $T = 77$ K as shown in Figure 4.8, for this the capacitance is estimated based on literature of Section 3.2.3. As the capacitance drops, the electrical frequency will increase creating an operating range of the shunt system of $f = 140 - 370$ Hz. A higher range is convenient as the eigenfrequencies will increase for lower temperatures.

A second variable resistance (R_7) is used for tuning the electrical resistance R directly, which is done according to Equation 3.40. The variable resistance needs to cover a range of frequencies, global coupling factors and capacitance values. To cover the desired range of $K_1 = 0.1 - 0.4$, $f = 95$ Hz $- 370$ Hz and $C = 1500$ nF $- 5500$ nF, the resistance needs to be $R = 15\ \Omega - 900\ \Omega$ resulting in chosen resistances $R_6 = 10\ \Omega$ and $R_7 = 0\ k\Omega - 1\ k\Omega$.

4.4 Dynamical model

The model of the experimental setup consists of the vacuum vessel mass, the isolation frame mass and the V-frames with implemented piezo transducers. Modal analysis using FEM software is performed to get better insight on the dynamical behaviour. An overview of the setup can be found in Figure 4.9. The piezo elements are modelled in their volume claim as a stiffness of 4e7 N/m based on the properties of Table 4.2.

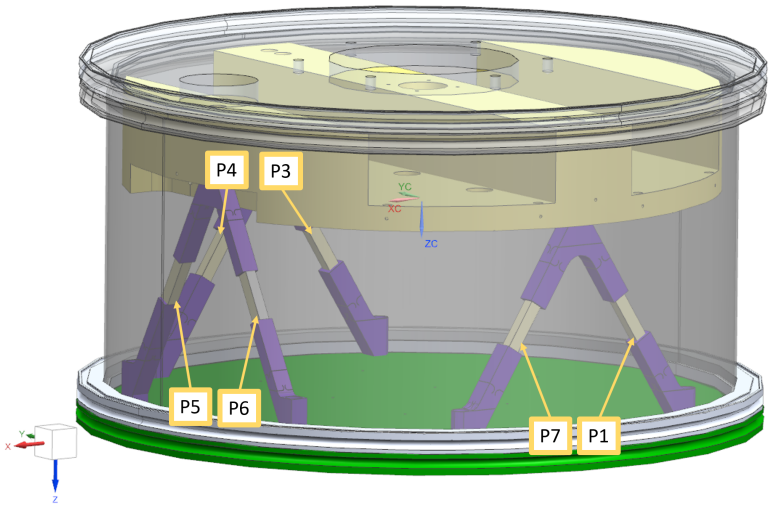

Figure 4.9: Overview of tested setup. Note: Transducer P_7 is used because transducer P_2 was damaged during assembly.

The eigenfrequencies are given in Table 4.4 with the degrees of freedom of the isolation frame as an indication for the mode shapes. Mode shapes related to the vacuum vessel (nr. 7 & 8) are not incorporated as they exist of plate modes.

Table 4.4: Modes overview

Nr.	Freq. [Hz]	Mode shape
1	102 Hz	y
2	148 Hz	R_y
3	209 Hz	x
4	224 Hz	plate
5	281 Hz	R_z
6	308 Hz	z (+ plate)
9	473 Hz	z
10	480 Hz	R_x

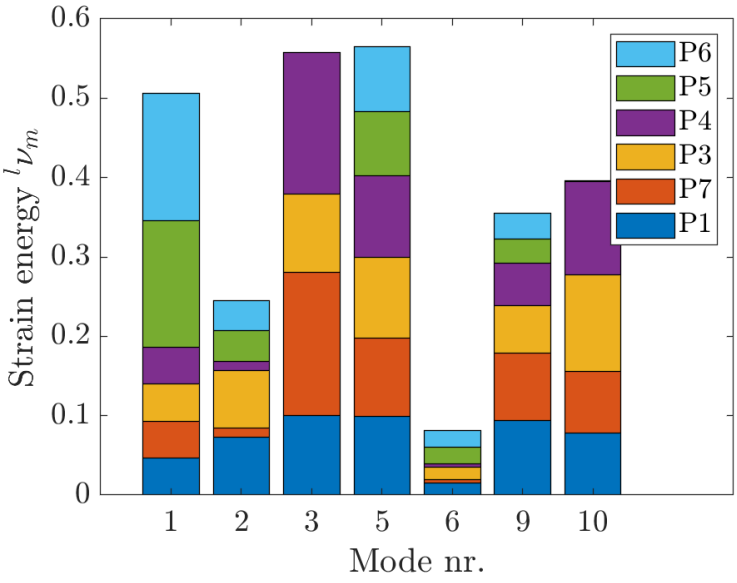

Figure 4.10: Fraction of strain energy

The first modes occur along the y and R_y direction, which is as expected based on the V-frame placement. The 3^{rd} mode is in x-direction which is the most interesting mode, as the demo setup is testing the planar motor in the x- and z-direction. The modes in z direction and the other two rotational modes R_z, R_x occur at higher frequencies due to stiffer design directions. The first mode in z-direction is in combination with a plate mode in the vacuum vessel, resulting in a lower density of strain energy in the piezo stacks. Also, the main mode in z-direction is expected to be higher, being more in line with mode 9.

The fraction of strain energy for each transducer is given in Figure 4.10; the effectiveness of each piezo for damping each mode is clearly visible. For the y-mode it is most effective to use transducers P_5 or P_6, which is as expected as they are in the V-frame placed in y-direction. For the 3^{rd} mode, transducer P_4 or P_7 show best effectiveness, while using transducer P_5 or P_6 will result in no damping at all. The mode shape of the modes in R_y and x-direction are depicted in Figure 4.11 and Figure 4.12, while the other mode shapes can be found in Appendix B. For clarity, some of the vacuum vessel parts are hidden.

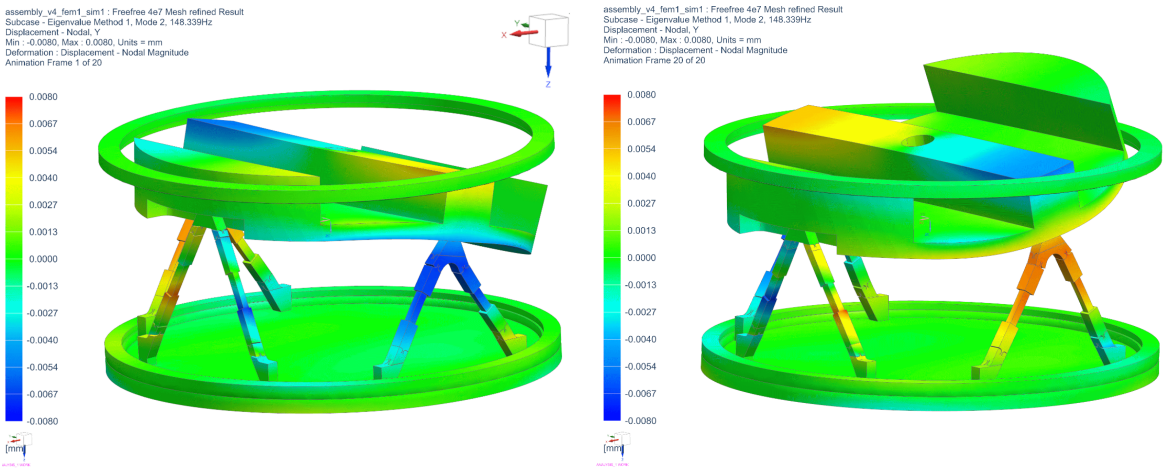

Figure 4.11: Mode shape of mode 2 in R_y-direction at $f = 148$ Hz.

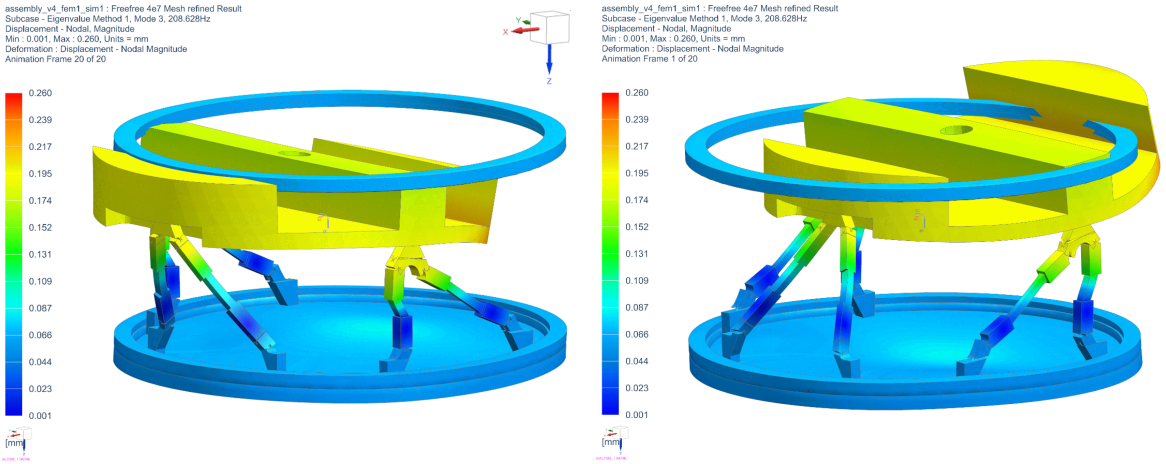

Figure 4.12: Mode shape of mode 3 in x-direction at $f = 209$ Hz.

CHAPTER 5

Experimental validation

The damping performance will be experimentally validated in Chapter 5. This is done by cooling the demonstrator with implemented transducers to cryogenic temperatures. The measurement plan is discussed first; the setup with implemented sensors is shown and the testing steps and method will be explained. The section will be concluded with the obtained results.

5.1 Measurement plan

An overview of the demonstrator with sensor placement is shown in Figure 5.1. Here, P denotes the transducers, T the temperature sensors and the accelerometer locations are depicted by $a_{x,z}$ In Figure 5.2 the schematic representation of the experimental setup is shown. The demonstrator is placed with 12 small spacers in a EPS isolation box, which is placed on a vibration isolation table. A 150L dewar containing liquid nitrogen is placed next to the table with a hose to pour LN2 on the demonstrator to cool it to $T = 77$ K. The analysis regarding thermal feasibility of cooling with LN2 and isolation with EPS can be found in Appendix C.1. Wiring is fed through the EPS isolation towards the excitation and measurement equipment. A graphic representation of the measurement setup and details on the used measurement equipment can be found in Appendix C.2.

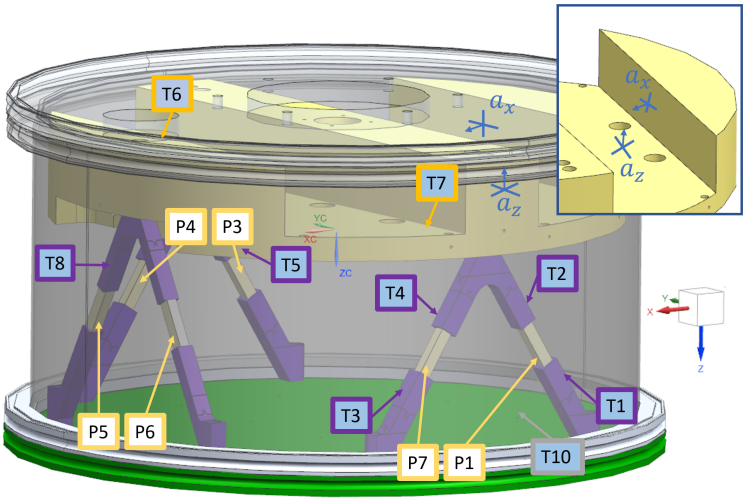

Figure 5.1: Sensor placement in the demonstrator.

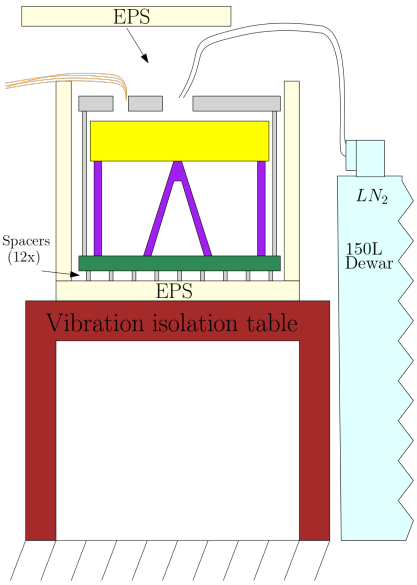

Figure 5.2: Experimental setup

Common methods for system excitation like a shaker test or impact test are hard to realize in the isolated cryogenic setup. For this reason, it is chosen to use one of the piezo transducers as an actuator. The excitation location is chosen to be piezo P_7, which will be used for all measurements unless mentioned otherwise. Two accelerometers were placed on the isolation mass in x- and z-direction, with their positioning shown in Figure 5.1. The location is chosen based on the largest expected displacement for the modes of interest, based on the dynamical analysis of Section 4.4.

In order to get the damping performance at cryogenic temperatures, several measurement steps need to be taken first. The different (measurement) steps are outlined below and explained for there functionality.

1. Mode identification (RT)
2. Fraction of strain energy evaluation (RT)
3. Damping (RT)
4. Repeat step 1 & 3 at different temperatures
5. Capacitance measurement at different temperatures

Mode identification at room temperature is performed to link the resonances in the measured dynamic response to the modes of Section 4.4 (step 1). Next, measurements with different electrical boundary conditions are performed to evaluate the fraction of strain energy of the transducers. Based on these steps a decision can be made on which transducer to use to target which mode (step 2). This mode can then be damped using the tuning method described below (step 3). After step 1-3 are finished at room temperature, the demonstrator is cooled down and step 1 & 3 are repeated in a temperature range of $T = 77$ K $-$ 205 K (step 4). Besides the mode identification and damping measurements, the capacitance of the piezoelectric transducer is also measured (step 5). Then, the natural-, realized- and obtainable damping can be deducted from the measurement results by:

ζ_0 The Half Power Bandwidth Method is used for this. Obtain the eigenfrequency Ω and the frequencies ω^+, ω^- where the power of the response is -3 dB lower. The difference in frequency ($\Delta\omega = \omega^+ - \omega^-$) can be used to estimate the natural damping using: $\zeta_0 = \Delta\omega/(2\Omega)$.

ζ_{att} Obtain the response level at Ω for the undamped situation and for the damped response. Use the attenuation α_{att} and the natural damping ζ_0 to calculate the obtained damping ratio: $\zeta_{\text{att}} = \zeta_0 \alpha_{\text{att}}$.

ζ_d Obtain the open and short-circuited eigenfrequencies Ω, ω and calculate the generalized coupling factor using Equation 3.37, next calculate the maximum obtainable performance ζ_d according to Equation 3.41.

Tuning method

Unlike the tuning of the theoretical model, where the capacitance of the piezo, the global coupling factor K_m and the resonance frequency Ω_m are already exactly known and an inductance and resistance value can be calculated according to Equation 3.39 - 3.40, the real system needs some iteration in order to get close to the optimal tuning.

First the response with open electrodes will be generated to obtain the eigenfrequency Ω_m. This makes it possible to tune the electrical frequency to be equal $\omega_e = \Omega_m$. The inductor tuning can be done by connecting the variable L-shunt[1] to the system and checking the accelerometer for the lowest time-response when exciting the system at the resonance frequency Ω. An anti-resonance at the original systems resonance frequency (Ω_m) is know created, similar to the system with L-shunt of Figure 3.9.

Now the inductance value is set, the resistance can be tuned iteratively. This is done by measuring the Frequency Response Function (FRF) with the electrical resistance tuned in the range of $R = 10\ \Omega - 150\ \Omega$ and visually checking the attenuation of the resonance peak.

5.2 Results

The experimental results will be examined in different parts, first the general mode identification will be done to match FEM results to the obtained FRFs. Secondly, the damping performance will be analysed by looking at the tuning effects as decribed in the measurement plan. Lastly, the change in capacitance and frequency will be compared to literature.

5.2.1 Mode identification

The obtained frequency response functions can be found in Figure 5.3 for the transfer from excitation transducer P_7 to the accelerometers in x- and z-direction. The mode in R_y and x-direction are visible around respectively $f = 118$ Hz and $f = 160$ Hz. The mode in y-direction is not visible in this frequency range. A look at the phase behaviour was needed to identify the modes, as the eigenfrequency for the R_y and x-mode is 20-25% lower compared to the FEM results. The x- and z-response are in-phase for $f = 118$ Hz, which complies with the R_y mode (see Figure 4.11). The x- and z-response are out-of-phase for $f = 160$ Hz, complying with the x-mode (see Figure 4.12).

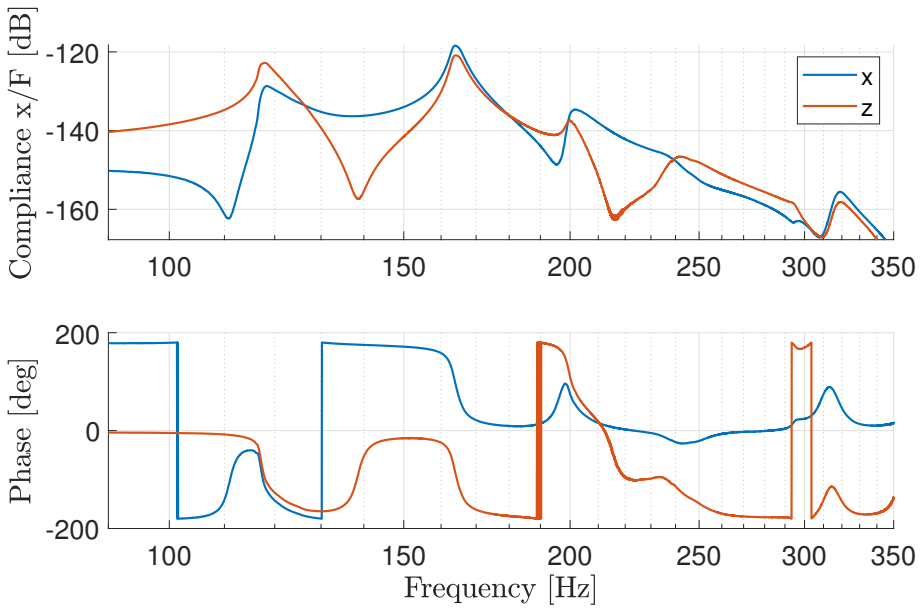

Figure 5.3: Measured open-circuit response of the demonstrator at $T = 293$ K

[1]Strictly taken it is still a RL-shunt due to fixed resistance R6 in series with the variable resistance R7.

Furthermore, the peak at $f = 205$ Hz is expected to represent the 4^{th} mode, occurring due to a plate mode of the bottom plate. The 5^{th} mode (R_z) of the FEM model is expected not to be visible and the 6^{th} mode (z) can be linked to the peak at $f = 245$ Hz, which is better visible in the z-direction compared to x-direction. The system dynamics for a larger frequency range can be found in Appendix C.3. Mode 2 and 3 are the only modes of interest for damping, so no further identification of the system is performed to confirm the identification of the other modes. An overview of the modes can be found in Table 5.1.

Table 5.1: Modes overview

Nr.	FEM	Exp.	Mode shape
1	102 Hz	-	y
2	148 Hz	118 Hz	R_y
3	209 Hz	160 Hz	x
4	224 Hz	*205* Hz	plate mode
5	281 Hz	-	R_z
6	308 Hz	*245* Hz	z (+ plate modes)
9	473 Hz	*445* Hz	z
10	480 Hz	-	R_z

In Figure 5.4 the resonance peak for the mode in R_y and x-direction are examined with different electrical boundary conditions. The different transducers are open- and short circuited one by one in order to examine the global coupling factor (and following fraction of strain energy) according to Equation 3.36. The situation where all transducers are short circuited, ω_m, can be compared to the situation where the l^{th} transducer is open circuited, ${}^{l}\Omega_m$. The change in frequency for the separate transducers can be seen with respect to the situation where all transducers are open circuited, Ω_m.

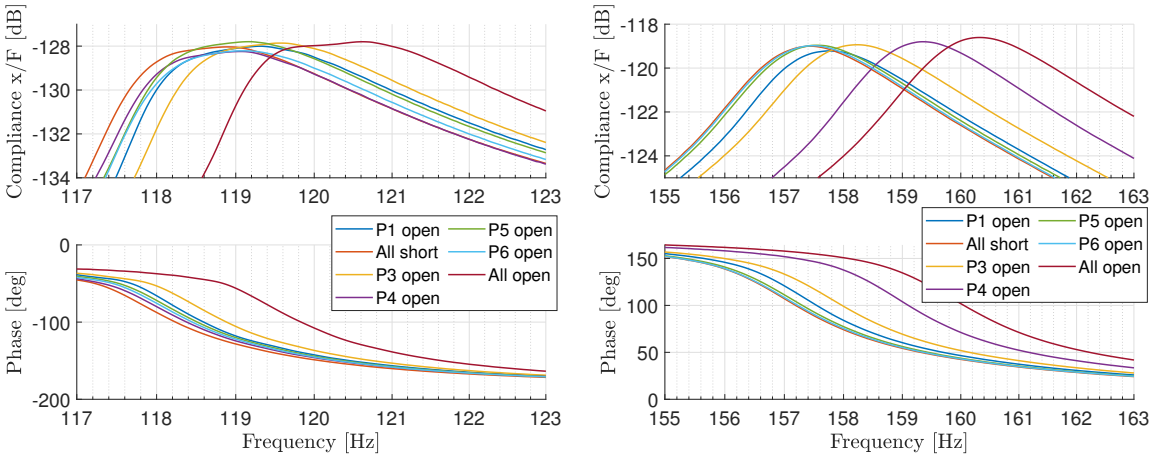

Figure 5.4: Measured response for different electrical boundary conditions. Zoomed at the R_y mode at $f = 120$ Hz (left) and the x mode at $f = 160$ Hz (right)

The fraction of strain energy for each transducer is obtained by Equation 3.36 and compared to the modal analysis, displayed in Figure 5.5. Here, the first column of each mode represents the fraction of strain energy of the FEM results, the second column represents the experimental results with piezo P_7 as excitation source and the third column with piezo P_1 as excitation source.

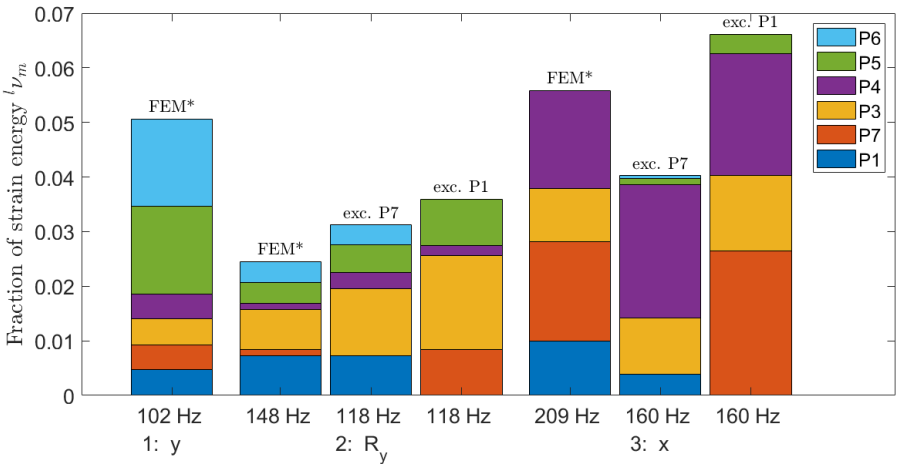

Figure 5.5: Fraction of strain energy of FEM model and experiments (*scaled $\times 0.1$)

The largest contribution to the total fraction of strain energy for the y-mode comes from P_5 and P_6 in the FEM analysis, which makes sense as the transducers are placed in the V-frame which constrains the y-direction. When comparing the strain energy of the R_y mode in FEM with the measured response at $f = 118$ Hz, it is seen that piezo P_3 has the highest contribution in both cases, followed by P_1 for the FEM and P_7 excitation results. This confirms the identification of the peak at $f = 118$ Hz to be the R_y mode. Finally, it is seen that P_4 and P_7 have the largest contribution for the x mode, just as was seen in the FEM results. So it is decided to use transducer P_4 to damp the x mode.

5.2.2 Damping

The results for damping the x-mode at room temperature are shown in Figure 5.6, together with the open and short circuited response.

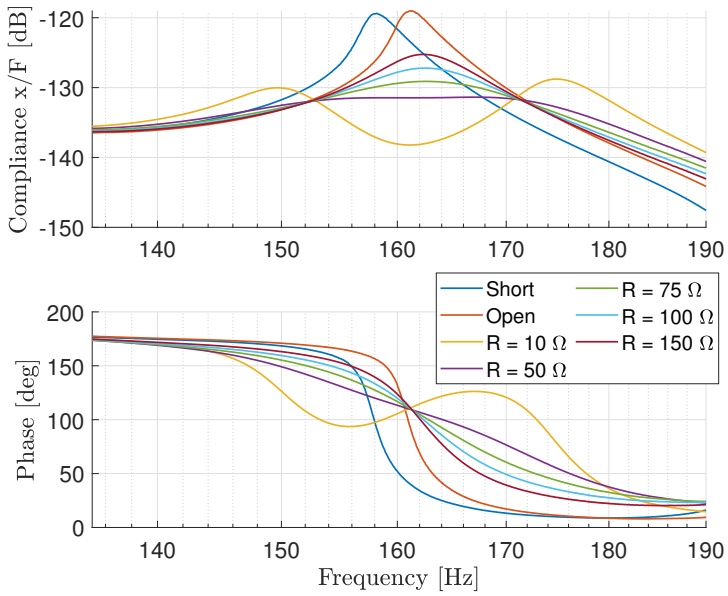

Figure 5.6: Tuning of shunt system ($\omega_e = 161.3$ Hz) at $T = 293$ K using P_4.

The tuning of $R = 10\ \Omega$ shows the behaviour of an (almost) L-shunt, with the lowest response at $f = 161$ Hz. For low resistance the response contains two peaks with some damping, having the poles of the system visually separate. Increasing the resistance to $R = 50\ \Omega$ shows the best attenuation of the system. It is seen that the damped poles move closer to each-other when the resistance is increased, which creates a response similar to a maximum damping design. Too much resistance limits the energy transfer to the circuit. The electrical resistance for best attenuation is in line with the tuning rules of Equation 3.40; $R_t = 55\ \Omega$ when considering the generalized coupling factor for transducer P_4 which can be calculated as ${}^4K_3 = 0.15$.

The global generalized coupling factor (all transducers used) can be calculated to be $K_3 = 0.195$, resulting in an obtainable damping of $\zeta_d = 0.069$. Furthermore, the natural damping is $\zeta_0 = 0.012$, which with an attenuation of 12.3 dB results in a realized damping of $\zeta_{att} = 0.049$. Knowing the piezoelectric capacitance (in the structure), the inductor value can be calculated according to Equation 4.4 to be L = 0.18 H. This inductor value is synthesized by the gyrator board with a resistance of $R_5 = 2$ kΩ, which is in line with the value used during tests.

The results for damping the x mode at $T = 77$ K are shown in Figure 5.7. The damping performance is lower compared to room temperature, having a maximal obtainable damping of $\zeta_d = 0.059$, a natural damping of $\zeta_0 = 0.006$ and a realized damping of $\zeta_{att} = 0.038$. Due to the next anti-resonance and resonance laying close to the damped peak, the tuning was not performed optimally, seen in the larger difference between obtainable damping and realized damping. The needed inductance is slightly increased to $L = 0.34$ H, based on a capacitance of $C = 2000$ nF. Furthermore, it is seen that the electrical resistance for best attenuation also increased, which is expected to be around $R_t = 106\ \Omega$.

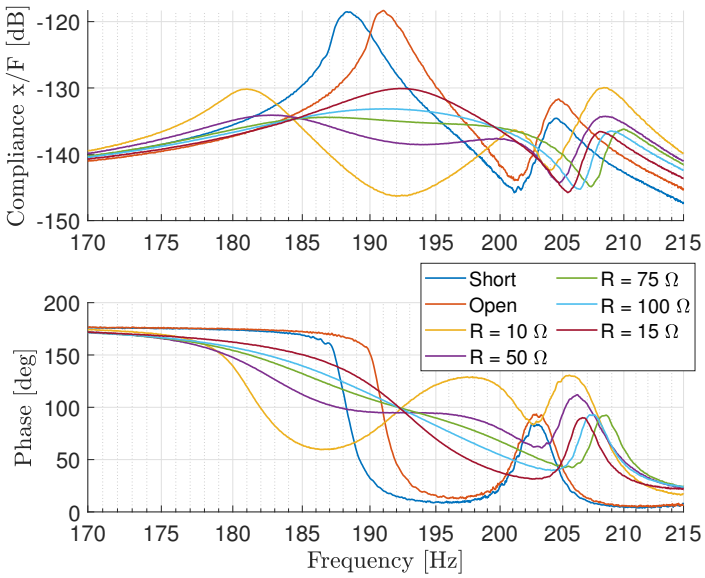

Figure 5.7: Tuning of shunt system ($\omega_e = 191$ Hz) at $T = 77$ K using P_4

The same analysis is performed for temperatures in the range of $T = 100$ K $-$ 205 K of which the corresponding tuning graphs can be found in Appendix C.3. The temperature at which the measurements are performed can be found in Figure 5.8. Here, the temperature is averaged over sensor T_1 and T_2 to determine the temperature at the transducer.

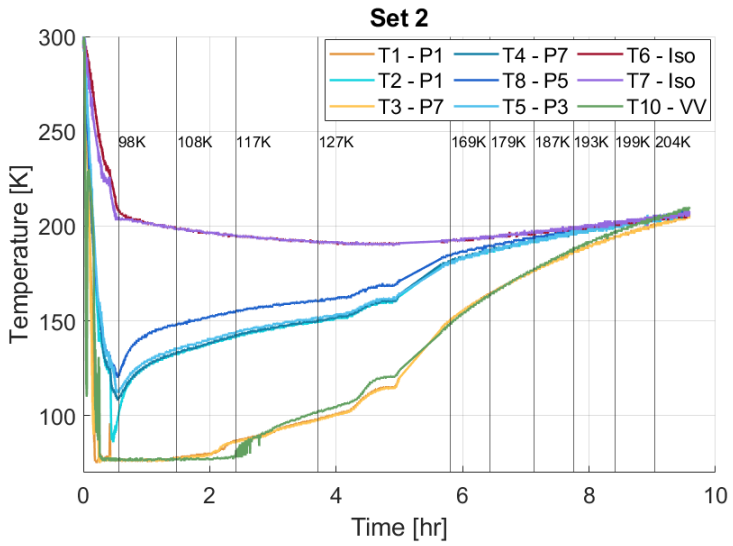

Figure 5.8: Temperature of setup during measurements of set 2.

The damping results for different temperatures are compared in Figure 5.9. Looking at the fitted damping ζ_d a decrease of 17.2% is observed from room temperature to $T = 80$ K. For the realized damping ζ_{att} a decrease of 16.1% is observed. Comparing this to the electromechanical coupling factor of Figure 3.17 found in literature, a decrease of 13.4% was observed. It is shown that the change in damping performance is minimal for a temperature of $T = 80$ K, which is related to the small change in electromechanical coupling factor k_{33}.

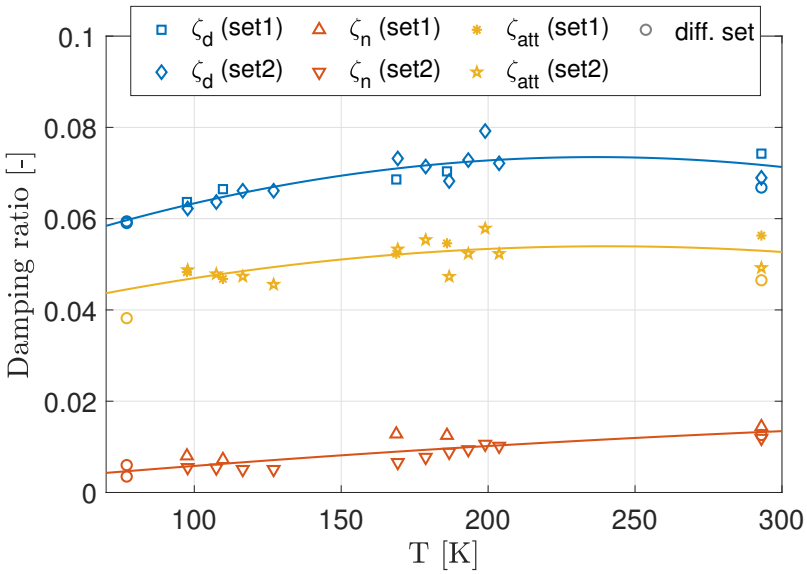

Figure 5.9: Measured damping as function of temperature

Furthermore, a damping of $\zeta_{\text{att}} = 0.053$ is realized at room temperature and a slightly lower damping of $\zeta_{\text{att}} = 0.045$ is seen at a temperature $T = 80$ K. At a temperature of $T = 100$ K a damping of $\zeta_{\text{att}} = 0.047$ is realized, showing the feasibility of the damping method.

5.2.3 Capacitance

The piezo capacitance plays an important role in the RL-shunt tuning, especially for cryogenic temperatures as it is highly dependent on temperature. This strong effect can be seen by the measurements of the capacitance of transducer P_3 and P_4 when implemented in the structure, displayed in Figure 5.10.

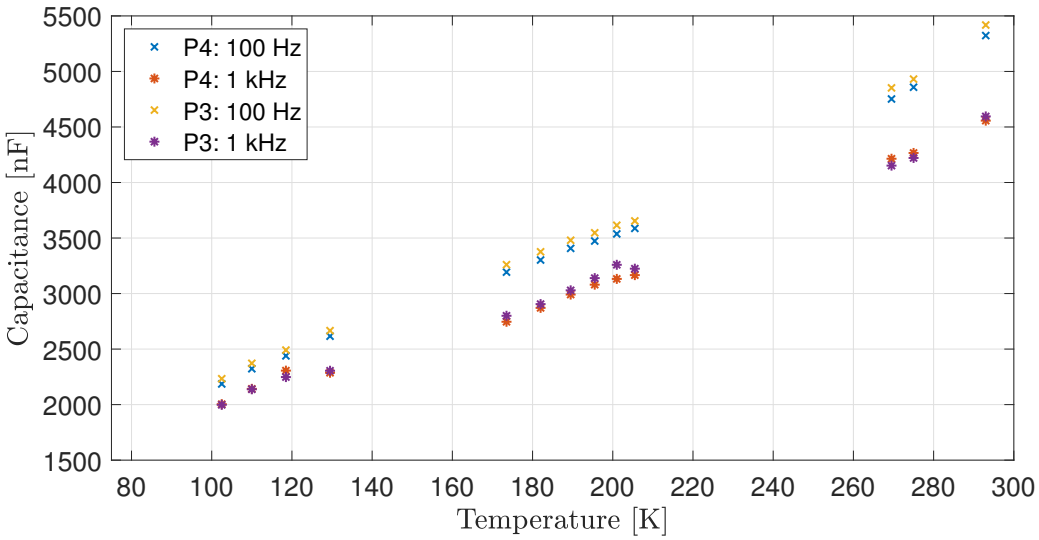

Figure 5.10: Capacitance of different transducers versus temperature (@1V$_{rms}$)

When looking at the temperature change of the capacitance a fairly linear relation is seen, where the capacitance of both transducer P_3 and P_4 is almost a factor 2.5 lower for $T = 100$ K compared to room temperature. The relation looks similar to the dielectric temperature dependence of type II in Figure 3.15, where the same temperature change causes a drop of a factor 2.9 in dielectric constant. The measured capacitance change is thus in line with the observation made in literature.

5.2.4 Elastic compliance

An increase in frequency for the x mode of 18% is observed, which would logically follow from an increase in stiffness of approximately 39%. This behaviour is not in line with the stiffness increase of 20-23% for PZT as shown in Section 3.2.3. This is not completely unexpected, as it was hard to obtain exact values for the elastic compliance for low temperatures. Furthermore, during transducer selection, it was already noted that suppliers do generally not specify a precise stiffness value as it depends on the used circumstances.

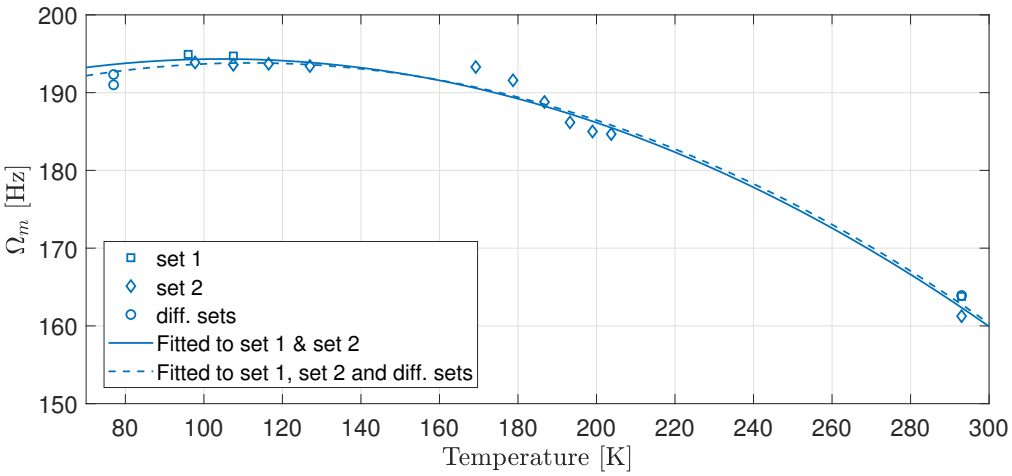

Figure 5.11: Frequency versus temperature for open circuit transducers

The extra increase in stiffness could be explained by the non-linear stress-strain relation of PZT. The pre-load of the stack increases due to the difference in thermal expansion between the beryllium-copper pre-load frame and the ceramic stack. The extra mechanical stress could increase the stiffness of the stack, as it is already known that the modulus can vary in a range of 25-60 GPa due to effects like the electrical control conditions, drive frequency and also mechanical pre-load [60]. Studies into this behaviour are performed and confirm the stress-dependent stiffness, but should be handled with care as different materials and circumstances are used [63].

CHAPTER 6

Conclusions and recommendations

6.1 Conclusions

It is shown that ECD is a less viable solution for the damping of the SCPM at temperatures $T > 50$ K, and frequencies $f > 100$ Hz for three main reasons: 1) the conductivity of copper only significantly increases for temperatures below $T = 10$ K; 2) the high frequency operation and increased conductivity of copper cause the penetration depth of the eddy currents to decrease significantly, decreasing the effective volume of the conductor; and 3) the counteracting mutual inductance effects at high frequencies which reduces significantly the damping performance. It is concluded that insufficient damping is obtained for the SCPM due to this.

Piezoelectric shunt damping showed superior damping performance at cryogenic temperatures. The electromechanical coupling factor k_{33}, being the main factor indicating the damping performance level, showed a decrease of only 13% at 80 K and a decrease of 22% at 4 K, which results in a maximum modal damping of about 9% at 80 K and 7% at 4 K, against 11% at room temperature.

The measurements, at room temperature, identified the mode in x-direction to be occurring at $f = 160$ Hz, exhibiting the highest fraction of strain energy at transducer P_4. Using only this transducer resulted into a realized damping of 5.3% which could be increased even further by using the other transducers. The required inductance $L = 0.2$ H is considered reasonable for practical implementation. Further experimental validation showed no decrease in performance at 200 K. At 80 K a damping performance of 4.5% is obtained, corresponding to a decrease of respectively 15.1%, well in line with the numerical thermomechanical model of the piezoelectric transducer. Measuring at very low temperatures, close to 4 K, was not possible and would require a more sophisticated thermal isolation and control.

Furthermore, the measured capacitance was in line with the change in dielectric constant in literature, both decreasing a factor 2.5-3 from room temperature to $T = 100$ K. To conclude, piezoelectric shunt damping has shown to be a viable damping solution for the SCPM demonstrator at $T = 80$ K.

6.2 Recommendations

Experimentally validating ECD on the observed effects (skin depth, mutual inductance) would be very useful to complement the comparison between ECD and piezoelectric shunt damping sketched in this work. By analysing and testing both solutions over a wide temperature and frequency range, a complete overview could be created on what solution would suit best for different applications.

Further depth in piezoelectric behaviour for cryogenic temperatures could lie with a better mapping of the non-linear effects and their influence on the application. It was observed that the non-linearity of the stiffness (function of electrical boundary, drive signal and mechanical stress) should be accounted for, to obtain higher predictability. Measurements with different mechanical and electrical loading could be investigated, similar to what is partly done in [63]. Other non-linearities like hysteresis and creep show smaller effects in cryogenics [64], due to less shifting of grain boundaries compared to room temperatures.

To better predict the dynamical behaviour of the system with piezoelectric shunt damping, an electromechanical model which represents the full system is recommended. In this way, the implementation of transducers can be further optimized and the experimental observed behaviour can be linked to the dynamical model.

For the specific application, it is recommended to design a monolithic V-frame connection and pre-loading mechanism. With this, the pre-load can be increased to withstand the expected tensile force of 1.8 kN and the connection design will become more deterministic. The axial elasticity of a concertina bush or similar spring mechanism is commonly used, with extra hinges to preserve the stack from bending loads. The latter is already covered by the V-frames. Another improvement for the current application lies with implementing multi-mode damping with a single transducer [65][66], single-mode damping with multiple transducers [45] or adaptive shunt damping [67].

Finally, single-crystal materials like PMN-PT could provide significant performance increase due to their outstanding electromechanical coupling factor, with $k_{33} = 0.95$ at room temperature and $k_{33} = 0.7$ at 10 K [57]. Further research into single-crystals for piezoelectric shunt damping at cryogenic temperatures is therefore recommended.

Bibliography

[1] R. S. Lakes, "High damping composite materials: Effect of structural hierarchy," *Journal of Composite Materials*, vol. 36, no. 3, pp. 287–297, 2002. [Online]. Available: https://doi.org/10.1177/0021998302036003538

[2] E. J. Gunter, R. Humphris, and S. J. Severson, "Design study of magnetic eddy-current vibration suppression dampers for application to cryogenic turbomachinery," University of Virginia, Tech. Rep., 1983.

[3] R. E. Cunningham, "Passive eddy-current damping as a means of vibration control in cryogenic turbomachinery," National Aeronatuics and Space Administration, Tech. Rep., 1986.

[4] K. Bender, "Cryogenic vibration damping mechanisms for space telescopes and interferometers," https://ehb8.gsfc.nasa.gov/sbir/docs/public/recent_srielections/SBIR_04_P1/S3.03/040344/briefchart.pdf, (accessed July, 2020).

[5] J. Zheng, Z. Deng, Y. Zhang, W. Wang, S. Wang, and J. Wang, "Performance improvement of high temperature superconducting maglev system by eddy current damper," *IEEE Transactions on Applied Superconductivity*, vol. 19, no. 3, pp. 2148–2151, Jun. 2009. [Online]. Available: https://doi.org/10.1109/TASC.2009.2017899

[6] Z. F. Jiang and X. F. Gou, "Eddy damping effect of additional conductors in superconducting levitation systems," *Physica C: Superconductivity and its Applications*, vol. 519, pp. 112–117, Oct. 2015. [Online]. Available: https://www.sciencedirect.com/science/article/pii/S0921453415002658

[7] J. A. Gripp and D. A. Rade, "Vibration and noise control using shunted piezoelectric transducers: A review," *Mechanical Systems and Signal Processing*, vol. 112, pp. 359–383, 2018. [Online]. Available: https://doi.org/10.1016/j.ymssp.2018.04.041

[8] K. Marakakis, G. K. Tairidis, P. Koutsianitis, and G. E. Stavroulakis, "Shunt piezoelectric systems for noise and vibration control: A review," *Frontiers in Built Environment*, vol. 5, May 2019. [Online]. Available: https://www.frontiersin.org/article/10.3389/fbuil.2019.00064

[9] H. Jaffe, "Piezoelectric Ceramics," *Journal of the American Ceramic Society*, vol. 41, no. 11, pp. 494–498, Jul. 1958.

[10] R. P. Taylor, G. F. Nellis, S. A. Klein, D. W. Hoch, J. Fellers, P. Roach, J. M. Park, and Y. Gianchandani, "Measurements of the material properties of a laminated piezoelectric stack at cryogenic temperatures," *AIP Conference Proceedings*, vol. 824, no. 1, pp. 200–207, 2006. [Online]. Available: https://aip.scitation.org/doi/abs/10.1063/1.2192352

[11] M. S. Islam and J. Beamish, "Shear Piezoelectric and Dielectric Properties of LiNbO 3 , PMN-PT and PZT-5A at Low Temperatures," *Journal of Low Temperature Physics*, vol. 194, no. 3-4, pp. 285–301, 2019. [Online]. Available: https://doi.org/10.1007/s10909-018-2097-7

[12] X. Jiang, W. B. Cook, and W. S. Hackenberger, "Cryogenic piezoelectric actuators," *Astronomical and Space Optical Systems*, vol. 7439, 2009. [Online]. Available: https://doi.org/10.1117/12.826341

[13] A. Veprik and V. Babitsky, "Ultra-light weight undamped tuned dynamic absorber for cryogenically cooled infrared electro-optic payload," *Cryogenics*, vol. 83, pp. 22–30, 2017. [Online]. Available: http://dx.doi.org/10.1016/j.cryogenics.2017.01.008

[14] A. Rittweger, J. Albus, E. Hornung, H. Öry, and P. Mourey, "Passive damping devices for aerospace structures," *Acta Astronautica*, vol. 50, no. 10, pp. 597–608, 2002.

[15] B. Zohuri, *Physics of Cryogenics*, 1st ed. Elsevier Science Publishing Co Inc, 2017.

[16] H. Koolmees, "A Superconducting Magnet Plate," Ph.D. dissertation, Eindhoven, Technische Universiteit, 2020.

[17] H. Butler and W. Simons, "Position control in lithographic equipment," *Proceedings of the ASPE 2013 Spring Topical Meeting*, vol. 55, pp. 7–12, 2013.

[18] Brainporteindhoven, "Photo of NXE:3400c EUV lithography system of ASML," https://brainporteindhoven.com/int/wp-content/uploads/2018/06/ASML-NXE_3400-system-right-semi-open_Original_43670-1024x718.png, (accessed May, 2020).

[19] H. B. Koolmees, B. J. De Bruyn, J. P. Vermeulen, J. W. Jansen, and E. A. Lomonova, "The performance potential of superconducting linear and planar motors," *Proceedings of the 17th International Conference of the European Society for Precision Engineering and Nanotechnology, EUSPEN 2017, Hannover, DE*, vol. 3, pp. 465–466, 2017.

[20] H. B. Koolmees and J. P. Vermeulen, "High stiffness fixation and thermal insulation in a superconducting planar motor," *Proceedings of the 18th International Conference of the European Society for Precision Engineering and Nanotechnology, EUSPEN 2018, Venice, IT*, pp. 191–192, 2018.

[21] K. E. Graves, D. Toncich, and P. G. Iovenitti, "Theoretical comparison of motional and transformer EMF device damping efficiency," *Journal of Sound and Vibration*, vol. 233, no. 3, pp. 441–453, 2000.

[22] B. Hendriks, "Passieve demping van mechanische systemen," Master's thesis, Dept. Mechanical Engineering, Eindhoven University of Technology, The Netherlands, 2004.

[23] H. A. Sodano and J. S. Bae, "Eddy current damping in structures," *Shock and Vibration Digest*, vol. 36, no. 6, pp. 469–478, 2004.

[24] X. Lu, Q. Zhang, D. Weng, Z. Zhou, S. Wang, S. A. Mahin, S. Ding, and F. Qian, "Improving performance of a super tall building using a new eddy-current tuned mass damper," *Structural Control and Health Monitoring*, vol. 24, pp. 1–17, 2017.

[25] S. B. Chikkamaranahalli, R. R. Vallance, B. N. Damazo, R. M. Silver, and J. D. Gilsinn, "Dynamic modeling and vibration analysis of a UHV scanning tunneling microscope," *Proceedings of the 20th Annual ASPE Meeting, ASPE 2005*, no. 1, 2005.

[26] D. A. Kienholz, C. A. Smith, W. B. Haile, D. A. Kienholz, C. A. Smith, and W. B. Haile, "Magnetically damped vibration isolation system for a space shuttle payload," vol. 2720, pp. 272–280, 2017.

[27] H. A. Sodano, J. S. Bae, D. J. Inman, and W. Keith Belvin, "Concept and model of eddy current damper for vibration suppression of a beam," *Journal of Sound and Vibration*, vol. 288, no. 4-5, pp. 1177–1196, 2005.

[28] H. A. Sodano, J. S. Bae, D. J. Inman, and W. K. Belvin, "Improved concept and model of eddy current damper," *Journal of Vibration and Acoustics, Transactions of the ASME*, vol. 128, no. 3, pp. 294–302, 2006.

[29] H. Teshima, Tanaka, K. Miyamoto, K. Nohguchi, and K. Hinata, "Effect of eddy current dampers on the vibrational properties in superconducting levitation using melt-processed YBaCuO bulk superconductors," *Physica C: Superconductivity and its Applications*, vol. 274, no. 1-2, pp. 17–23, 1997.

[30] C. Elbuken, M. B. Khamesee, and M. Yavuz, "Eddy current damping for magnetic levitation: Downscaling from macro- to micro-levitation," *Journal of Physics D: Applied Physics*, vol. 39, no. 18, pp. 3932–3938, 2006.

[31] J. S. Bae, M. K. Kwak, and D. J. Inman, "Vibration suppression of a cantilever beam using eddy current damper," *Journal of Sound and Vibration*, vol. 284, no. 3-5, pp. 805–824, 2005.

[32] D. Meeker, "Finite Element Method Magnetics," https://www.femm.info/, (accessed July 21, 2020).

[33] D. Cebron, "Magnetic fields of solenoids and magnets," https://nl.mathworks.com/matlabcentral/fileexchange/71881-magnetic-fields-of-solenoids-and-magnets, 2016, (Accessed July, 2020).

[34] Janssen Precision Engineering, "Cryogenic (4K... 293K) Material Properties," https://www.jpe-innovations.com/precision-point/cryogenic-material-properties/, (accessed July, 2020).

[35] E. J. Rothwell and M. J. Cloud, *Electromagnetics*, 3rd ed. CRC Press, 2018.

[36] B. Hao, X. Liu, K. M. Lee, and K. Bai, "State-space model and analysis of motion-induced eddy-current based on distributed current source method," *IEEE/ASME International Conference on Advanced Intelligent Mechatronics, AIM*, vol. 2019-July, pp. 1528–1533, 2019.

[37] K. Leang, Q. Zou, and G. Pannozzo, "Teaching modules on modeling and control of piezoactuators for system dynamics, controls, and mechatronics courses," *Education, IEEE Transactions on*, vol. 53, pp. 372 – 383, 09 2010.

[38] S. Wu, B. Avenue, H. Beach, T. L. Turner, and S. A. Rizzi, "Piezoelectric shunt vibration damping of F-15 panel under high acoustic excitation," *Proceedings of 7th International Symposium on Smart Structures and Materials, Newport Beach, CA*, vol. 3989, no. 27, pp. 5–9, 2000.

[39] T. L. Rocha and M. Dias, "Improved sound transmission loss in an automotive component using piezoceramic patches and dissipative shunt circuits," *Journal of Intelligent Material Systems and Structures*, vol. 26, no. 4, pp. 476–486, 2015.

[40] F. Bachmann, R. De Oliveira, A. Sigg, V. Schnyder, T. Delpero, R. Jaehne, A. Bergamini, V. Michaud, and P. Ermanni, "Passive damping of composite blades using embedded piezoelectric modules or shape memory alloy wires: A comparative study," *Smart Materials and Structures*, vol. 21, no. 7, 2012.

[41] R. L. Forward, "Electronic damping of vibrations in optical structures," *Applied Optics*, vol. 18, no. 5, p. 690, 1979.

[42] F. A. C. Viana and V. Steffen, Jr, "Multimodal vibration damping through piezoelectric patches and optimal resonant shunt circuits," *Journal of the Brazilian Society of Mechanical Sciences and Engineering*, vol. 28, pp. 293–310, 09 2006.

[43] N. W. Hagood and A. von Flotow, "Damping of structural vibrations with piezoelectric materials and passive electric networks," *Journal of Sound and Vibration*, vol. 146, pp. 243–268, 1991.

[44] A. Preumont, *Vibration control of active structures*, 4th ed. Springer, 2011, vol. 246.

[45] B. Mokrani, "Piezoelectric Shunt Damping of Rotationally Periodic Structures," Ph.D. dissertation, Université libre de Bruxelles, 2015. [Online]. Available: https://scmero.ulb.ac.be/Publications/Thesis/Mokrani_2015_thesis.pdf

[46] D. S. Paik, S. E. Park, and W. Hackenberger, "Cryogenic behavior of perovskite materials," *Ferroelectrics*, vol. 221, no. 1-4, pp. 175–180, 1999.

[47] B. D. Marneffe, "Active and Passive Vibration Isolation and Damping via Shunted Transducers," Ph.D. dissertation, Bruxelles, Universite Libre de Bruxelles, 2007.

[48] W. Wersing, W. Heywang, and K. Lubitz, *Piezoelectricity Evolution and Future of a Technology*, 1st ed. Springer, 2008.

[49] X. L. Zhang, Z. X. Chen, L. E. Cross, and W. A. Schulze, "Dielectric and piezoelectric properties of modified lead titanate zirconate ceramics from 4.2 to 300 K," *Journal of Materials Science*, vol. 18, no. 4, pp. 968–972, 1983.

[50] R. G. Sabat, B. K. Mukherjee, W. Ren, and G. Yang, "Temperature dependence of the complete material coefficients matrix of soft and hard doped piezoelectric lead zirconate titanate ceramics," *Journal of Applied Physics*, vol. 101, no. 6, 2007.

[51] B. Yurke, P. G. Kaminsky, and D. M. Eigler, "Cryogenic piezoelectric displacement tester," *Cryogenics*, vol. 26, no. 7, pp. 435–436, 1986.

[52] E. R. Naimon, W. F. Weston, and H. M. Ledbetter, "Elastic properties of two titanium alloys at low temperatures," *Cryogenics*, vol. 14, no. 5, pp. 246–249, 1974.

[53] CedratTechnologies, "Mechatronic solutions," https://www.cedrat-technologies.com/en/catalogue, (Accessed August, 2020).

[54] CTSCorporation, "PZT Materials Complete Properties," https://www.ctscorp.com/wp-content/uploads/CTS_-PZT-Materials_Complete-Properties_20180829.pdf, (Accessed August, 2020).

[55] P. Groen, *An Introduction to PiezoelectricMaterials and Components An Introduction to Piezoelectric Materials and Components.* Stichting Applied Piezo, 2018.

[56] Z. Yang and J. Zu, "Comparison of PZN-PT, PMN-PT single crystals and PZT ceramic for vibration energy harvesting," pp. 321–329, 2016.

[57] F. Martin, H. J. Ter Brake, L. Lebrun, S. Zhang, and T. Shrout, "Dielectric and piezoelectric activities in (1-x)Pb(Mg 1/3Nb 2/3)O 3-xPbTiO 3 single crystals from 5 K to 300 K," *Journal of Applied Physics*, vol. 111, no. 10, pp. 2–7, 2012.

[58] E. K. Akdogan, M. Allahverdi, and A. Safari, "Piezoelectric composites for sensor and actuator applications," *IEEE Transactions on Ultrasonics, Ferroelectrics, and Frequency Control*, vol. 52, no. 5, pp. 746–775, 2005.

[59] CTS Corporation, "Tools and Tutorials," https://www.ctscorp.com/resource-center/tutorials/faq/, (accessed September, 2020).

[60] PI Ceramic GmbH, "Properties of Piezo Actuators," https://www.piceramic.com/en/piezo-technology/properties-piezo-actuators/forces-stiffnesses/, (accessed September, 2020).

[61] CTS Corp, "PZT Materials Complete Properties," https://www.ctscorp.com/wp-content/uploads/CTS_-PZT-Materials_Complete-Properties_20180829.pdf, (accessed September, 2020).

[62] A. Antoniou and K. S. Naidu, "Modeling of a Gyrator Circuit." vol. 20, no. 5, pp. 272–275, 1973.

[63] M. Selten, G. A. Schneider, and V. Knoblauch, "On the evolution of the linear material properties of PZT during loading history — an experimental study," *International Journal of Solids and Structures*, vol. 42, pp. 3953–3966, 2005.

[64] M. S. Islam and J. Beamish, "Shear Piezoelectric and Dielectric Properties of LiNbO 3 , PMN-PT and PZT-5A at Low Temperatures," *Journal of Low Temperature Physics*, vol. 194, no. 3-4, pp. 285–301, 2019. [Online]. Available: https://doi.org/10.1007/s10909-018-2097-7

[65] J. J. Hollkamp, "Multimodal passive vibration suppression with piezoelectric materials and resonant shunts," *Journal of Intelligent Material Systems and Structures*, vol. 5, no. 1, pp. 49–57, 1994.

[66] S. Wu, "Method for multiple mode piezoelectric shunting with single pzt transducer for vibration control," *Journal of Intelligent Material Systems and Structures*, vol. 9, no. 12, pp. 991–998, 1998.

[67] B. Mokrani, I. Burda, and A. Preumont, "Adaptive inductor for vibration damping in presense of uncertainty," in *Smart Structures and Materials*, vol. 43. Springer International Publishing AG, 2017, pp. 133–152.

[68] National Institute of Standards and Technology, "Properties of solid materials from cryogenic- to room-temperatures," https://trc.nist.gov/cryogenics/materials/materialproperties.htm, (accessed August, 2020).

APPENDIX A

Piezoelectric 1-DoF model extended

First the double mass-spring-piezo model with 2 transducers is derived, which results are used in Section 3.2.2. Then, the modal decomposition and state space representation is shown, which is used to model the system with a modal damping ζ_0 and obtain the modes shapes. Lastly, the impedance of the non-used transducer is analysed to conclude on what electrical boundary conditions to use when tuning other circuits.

Model

The two masses are modelled with displacement x_i and are connected to respectively each-other and the fixed world via a spring k_i in series with a transducer stiffness K_{ai}^*. The connection point between the spring and transducer is modelled by the displacement Δ_i. The system overview and the force equilibrium are shown in Figure A.1 and A.2.

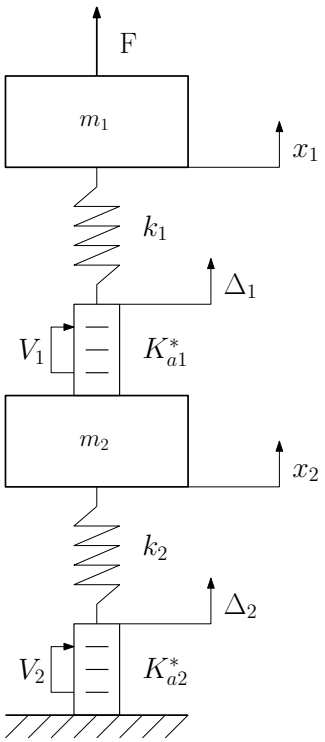

Figure A.1: 1DOF system with 2 masses

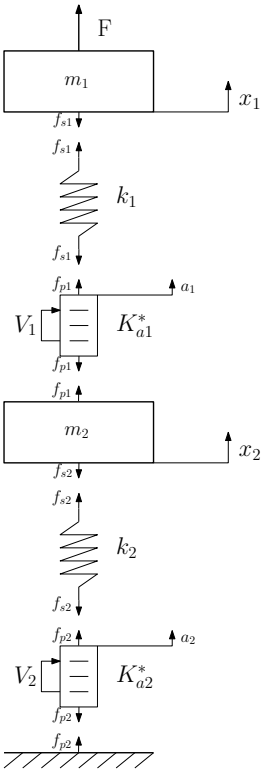

Figure A.2: Force balance of system

The dynamic equilibrium of the masses gives the mechanical equations of motion based on Newtons second law

$$m_1\ddot{x}_1 = -f_{s1} + F_1 \tag{A.1}$$

$$m_2\ddot{x}_2 = -f_{s2} + f_{p1} + F_2 \tag{A.2}$$

where F_i gives the external force applied to mass m_i. Moreover, f_{si} is the spring force, which is auto-equilibrated at the attachment point Δ_i to the piezoelectric transducer force f_{pi}. This is depicted in the force balance of Figure A.2 and gives

$$f_{si} = k_i(x_i - \Delta_i) = f_{pi} \tag{A.3}$$

resulting in an expressing for the displacement point Δ_i

$$\Delta_i = -\frac{f_{pi}}{k_i} + x_i \tag{A.4}$$

The transducer force can be obtained by using the piezoelectric constitutive equations

$$f_{p1} = -\frac{n_1 d_{33} K_{a1}^*}{C_1} Q_1 + K_{a1}^*(\Delta_1 - x_2) \tag{A.5}$$

$$f_{p2} = -\frac{n_2 d_{33} K_{a2}^*}{C_2} Q_2 + K_{a2}^* \Delta_2 \tag{A.6}$$

Here, it is assumed that the piezostack geometry might vary for piezostack 1 and piezostack 2, but the material (d_{33}) is the same for both. K_{ai}^* is the stiffness of the transducers with open circuited electrodes,

$$K_{ai}^* = \frac{K_{ai}}{1 - k_{ci}^2} \tag{A.7}$$

with k_{ci} the electromechanical coupling factor. Substituting Equation A.4 into Equation A.5 and A.6 gives respectively

$$f_{p1} = -\frac{n_1 d_{33} K_{a1}^*}{C_1} \gamma_{11} Q_1 + K_{a1}^* \gamma_{11}(x_1 - x_2) \tag{A.8}$$

$$f_{p2} = -\frac{n_2 d_{33} K_{a2}^*}{C_2} \gamma_{12} Q_2 + K_{a2}^* \gamma_{12} x_2 \tag{A.9}$$

where γ_{1i} (and γ_{2i}) depict the stiffness ratio between the spring and the piezoelectric transducer, given by

$$\gamma_{1i} = \frac{k_i}{k_i + K_{ai}^*} \tag{A.10}$$

$$\gamma_{2i} = \frac{K_{ai}^*}{k_i + K_{ai}^*} \tag{A.11}$$

Now, substitution of Equation A.4 and A.8-A.9 into Equation A.1-A.2 leaves the mechanical system as

$$m_1\ddot{x}_1 = \frac{n_1 d_{33} K_{a1}^*}{C_1} \gamma_{11} Q_1 - K_{a1}^* \gamma_{11}(x_1 - x_2) + F_1 \tag{A.12}$$

$$m_2\ddot{x}_2 = \frac{n_2 d_{33} K^*_{a2}}{C_2}\gamma_{12}Q_2 - K^*_{a2}\gamma_{12}x_2 - \frac{n_1 d_{33} K^*_{a1}}{C_1}\gamma_{11}Q_1 + K^*_{a1}\gamma_{11}(x_1 - x_2) + F_2 \tag{A.13}$$

The equilibrium of the piezoelectric system can be described using the constitutive equations, given by

$$V_1 = \frac{1}{C_1(1-k^2_{c1})}Q_1 - \frac{n_1 d_{33} K^*_{a1}}{C_1}(\Delta_1 - x_2) \tag{A.14}$$

$$V_2 = \frac{1}{C_2(1-k^2_{c2})}Q_2 - \frac{n_2 d_{33} K^*_{a2}}{C_2}\Delta_2 \tag{A.15}$$

using Δ_i of Equation A.4 and respecitively f_{p1} of Equation A.8 or f_{p2} of Equation A.9, yields

$$\Delta_1 = \frac{n_1 d_{33}\gamma_{21}}{C_1}Q_1 + \gamma_{11}x_1 + \gamma_{21}x_2 \tag{A.16}$$

$$\Delta_2 = \frac{n_2 d_{33}\gamma_{22}}{C_2}Q_2 + \gamma_{12}x_2 \tag{A.17}$$

Substituting Equation A.16, A.17 in respectively Equation A.14, A.15, plus using the definition of the coupling factor

$$k^2_{ci} = \frac{n_i^2 d_{33}^2 K_{ai}}{C_i}, \tag{A.18}$$

yields the final electrical equations,

$$V_1 = \frac{1-\gamma_{21}k^2_{c1}}{C_1(1-k^2_{c1})}Q_1 - \frac{n_1 d_{33} K^*_{a1}\gamma_{11}}{C_1}(x_1 - x_2) \tag{A.19}$$

$$V_2 = \frac{1-\gamma_{22}k^2_{c2}}{C_2(1-k^2_{c2})}Q_2 - \frac{n_2 d_{33} K^*_{a2}\gamma_{12}}{C_2}x_2 \tag{A.20}$$

This leaves the total set of equations, transferred to the Laplace domain

$$\begin{bmatrix} m_1 s^2 + K^*_{a1}\gamma_{11} & -K^*_{a1}\gamma_{11} & -\frac{n_1 d_{33} K^*_{a1}}{C_1}\gamma_{11} & 0 \\ -K^*_{a1}\gamma_{11} & m_2 s^2 + K^*_{a1}\gamma_{11} + K^*_{a2}\gamma_{12} & \frac{n_1 d_{33} K^*_{a1}}{C_1}\gamma_{11} & -\frac{n_2 d_{33} K^*_{a2}}{C_2}\gamma_{12} \\ -\frac{n_1 d_{33} K^*_{a1}\gamma_{11}}{C_1} & \frac{n_1 d_{33} K^*_{a1}\gamma_{11}}{C_1} & \frac{1-\gamma_{21}k^2_{c1}}{C_1(1-k^2_{c1})} & 0 \\ 0 & -\frac{n_2 d_{33} K^*_{a2}\gamma_{12}}{C_2} & 0 & \frac{1-\gamma_{22}k^2_{c2}}{C_2(1-k^2_{c2})} \end{bmatrix} \begin{bmatrix} x_1 \\ x_2 \\ Q_1 \\ Q_2 \end{bmatrix} = \begin{bmatrix} F_1 \\ F_2 \\ V_1 \\ V_2 \end{bmatrix} \tag{A.21}$$

Modal decomposition

Taking the mechanical part describing the behaviour of x_i of Equation 3.34 and writing it in the form of a mass $\underline{M}$, damping $\underline{C}$ and stiffness $\underline{K}$ matrix, with the force $\underline{F}$ and charge $\underline{Q}$ as input gives

$$\underline{M}\,\underline{\ddot{x}} + \underline{C}\,\underline{\dot{x}} + \underline{K}^D\,\underline{x} = \underline{\alpha}_1\underline{F} - \underline{\alpha}_2\underline{Q} \tag{A.22}$$

Defining matrices α_i and β as

$$\alpha_1 = \begin{bmatrix} 1 & 0 \\ 0 & 1 \end{bmatrix}, \qquad \alpha_2 = \begin{bmatrix} -a_1 & 0 \\ a_1 & -a_2 \end{bmatrix}, \qquad \beta = \begin{bmatrix} b_1 & 0 \\ 0 & b_2 \end{bmatrix} \tag{A.23}$$

Using β to substitute $\underline{Q}$ and get the system equations as function of the voltage $\underline{V}$ gives

$$\underline{M}\,\underline{\ddot{x}} + \underline{C}\,\underline{\dot{x}} + (\underline{K}^D - \underline{\alpha}_2\underline{\beta}^{-1}\underline{\alpha}_2)\,\underline{x} = \underline{\alpha}_1\underline{F} - \underline{\alpha}_2\underline{\beta}^{-1}\underline{V} \tag{A.24}$$

The stiffness matrix can be rewritten as $\underline{K}^E = \underline{K}^D - \underline{\alpha}_2\underline{\beta}^{-1}\underline{\alpha}_2$, showing the difference in electrical boundary conditions. Next, a modal decomposition is done by substituting $\underline{x} = \underline{\Phi}\underline{\eta}$ and pre-multiplying the whole equation with $\underline{\Phi}^T$ leaves

$$\underline{\Phi}^T\underline{M}\,\underline{\Phi}\underline{\ddot{\eta}} + \underline{\Phi}^T\underline{C}\,\underline{\Phi}\underline{\dot{\eta}} + \underline{\Phi}^T\underline{K}^E\,\underline{\Phi}\underline{\eta} = \underline{\Phi}^T\left(\underline{\alpha}_1\underline{F} + \underline{\alpha}_2\underline{\beta}^{-1}\underline{V}\right) \tag{A.25}$$

Due to the mass orthogonality of the eigenvector the mass matrix can be written according to Equation A.26. Depending on the electrical boundary conditions, either the charge is set equal to zero ($Q_i = 0$) or the voltage is set equal to zero ($V_i = 0$) representing respectively open- and short circuited electrodes. The resulting decomposition for both situations is shown by Equation A.27 - A.30. Here, the modal damping can be applied by $\zeta_{0,i}$.

$$\underline{\Phi}^T\underline{M}\,\underline{\Phi} = \begin{bmatrix} 1 & 0 \\ 0 & 1 \end{bmatrix} \tag{A.26}$$

$$\underline{\Phi}^T\underline{C}^E\,\underline{\Phi} = \begin{bmatrix} 2\zeta_{0,1}\omega_1 & 0 \\ 0 & 2\zeta_{0,2}\omega_2 \end{bmatrix} \tag{A.27}$$

$$\underline{\Phi}^T\underline{C}^D\,\underline{\Phi} = \begin{bmatrix} 2\zeta_{0,1}\Omega_1 & 0 \\ 0 & 2\zeta_{0,2}\Omega_2 \end{bmatrix} \tag{A.28}$$

$$\underline{\Phi}^T\underline{K}^E\,\underline{\Phi} = \begin{bmatrix} \omega_1^2 & 0 \\ 0 & \omega_2^2 \end{bmatrix} \tag{A.29}$$

$$\underline{\Phi}^T\underline{K}^D\,\underline{\Phi} = \begin{bmatrix} \Omega_1^2 & 0 \\ 0 & \Omega_2^2 \end{bmatrix} \tag{A.30}$$

State space representation

By taking $\underline{\delta}_1 = \underline{\eta}$ and $\underline{\delta}_2 = \dot{\underline{\delta}}_1$ and making use of the definitions of Equation A.26-A.30 the system can be rewritten into state space representation, this is done for the short circuited boundary conditions and given as

$$\begin{bmatrix} \dot{\underline{\delta}}_1 \\ \dot{\underline{\delta}}_2 \end{bmatrix} = \begin{bmatrix} \underline{0} & \underline{I} \\ -\underline{\omega}^2 & -2\underline{\zeta}_0\underline{\omega} \end{bmatrix} \begin{bmatrix} \underline{\delta}_1 \\ \underline{\delta}_2 \end{bmatrix} + \begin{bmatrix} \underline{0} & \underline{0} \\ \underline{\Phi}^T\underline{\alpha}_1 & \underline{\Phi}^T\underline{\alpha}_2\underline{\beta}^{-1}\underline{\alpha}_2 \end{bmatrix} \begin{bmatrix} \underline{F} \\ \underline{V} \end{bmatrix} \tag{A.31}$$

$$\underline{y} = \begin{bmatrix} \underline{x} \\ \underline{Q} \end{bmatrix} = \begin{bmatrix} \underline{\Phi} & \underline{0} \\ \underline{\alpha}_2\underline{\beta}^{-1}\underline{\Phi} & \underline{0} \end{bmatrix} \begin{bmatrix} \underline{\delta}_1 \\ \underline{\delta}_2 \end{bmatrix} + \begin{bmatrix} \underline{0} & \underline{0} \\ \underline{0} & \underline{\beta}^{-1} \end{bmatrix} \begin{bmatrix} \underline{F} \\ \underline{V} \end{bmatrix} \tag{A.32}$$

This system is depicted in a feedback diagram, shown in Figure A.3, where the charge is fed back into the system. The impedance $Z(s)$ represents the shunt circuit connected, which tuning details will be shown next.

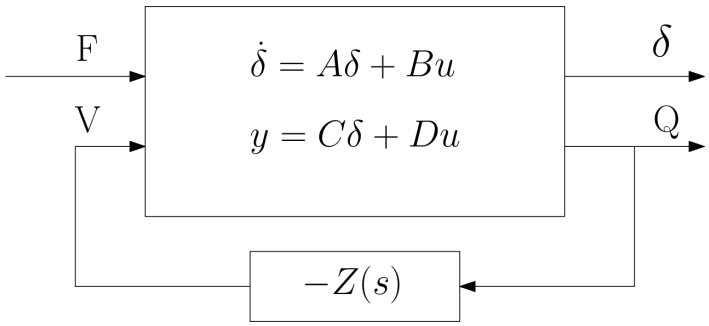

Figure A.3: State space feedback diagram

Shunt system

The boundary conditions of Table 3.6 of the inactive transducer (e.g. p_1 is not used for mode 1) are chosen based on the impedance that the transducer will feel at this frequency. This is done because it is observed that the stiffness of the inactive transducer will influence the frequencies ω_m, Ω_m of the active mode by a few percent. This will both have an effect on the tuning as well as on the performance indication by K_m. In Figure A.4 it can be seen that the impedance of transducer p_2 (with shunt) is close to the open circuit for mode 2. The boundary condition of p_2 is therefore set as an open circuit in Table 3.6 when examining ω_2, Ω_2. For the first transducer p_1, the impedance is like a capacitor and hence in-between short- and open circuit. It is chosen to set the transducer p_1 to short-circuited when examining ω_1, Ω_1. However, this is an assumption as it is hard to obtain the real impedance when tuning multiple modes

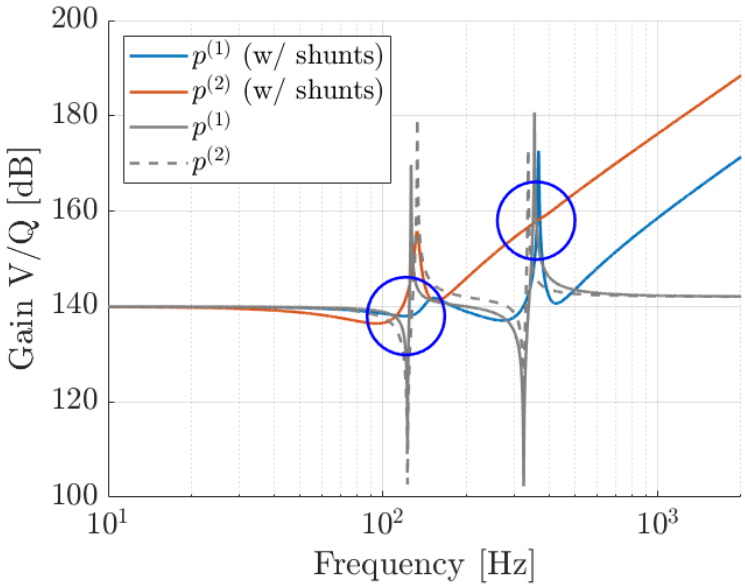

Figure A.4: Shunt impedance

Transfer function in Z-direction

The transfer function in Z-direction for the SCPM following from the double mass-spring-oiezo system with implemented transducers is depicted in Figure A.5.

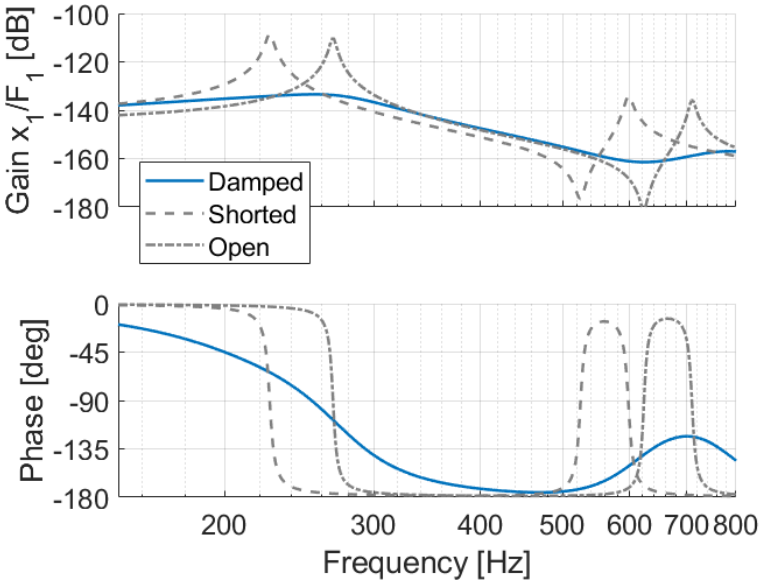

Figure A.5: Transfer function for 1-DoF double mass-piezo-spring system in z-direction

APPENDIX B

Mode shapes of dynamical model

The mode shapes for the SCPM demonstrator with implemented transducers as discussed in Section 4.4 are depicted in Figures B.1- B.5. The vacuum vessel is partly hidden, for better visualization of the modes.

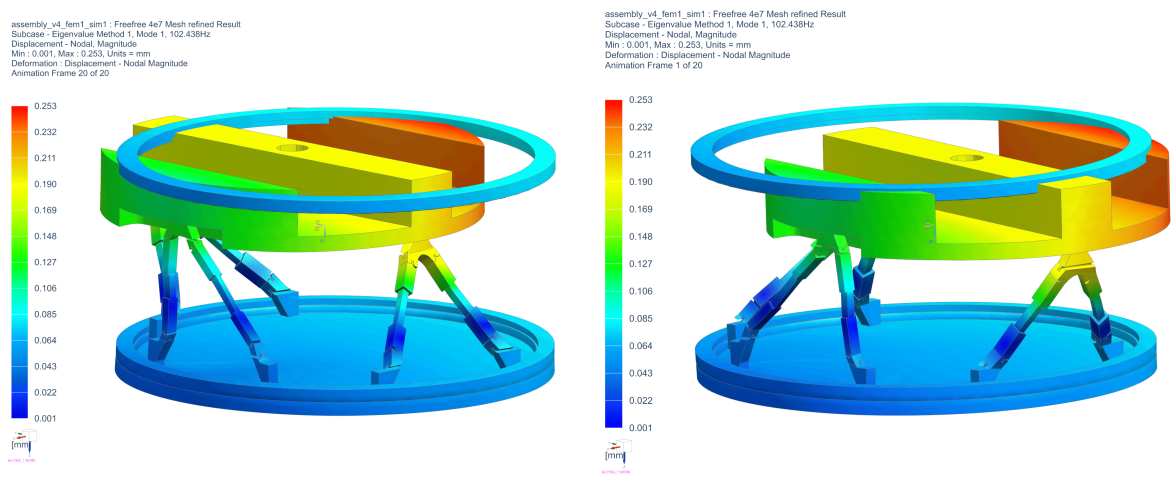

Figure B.1: Mode shape of mode 1 in y-direction at $f = 224$ Hz.

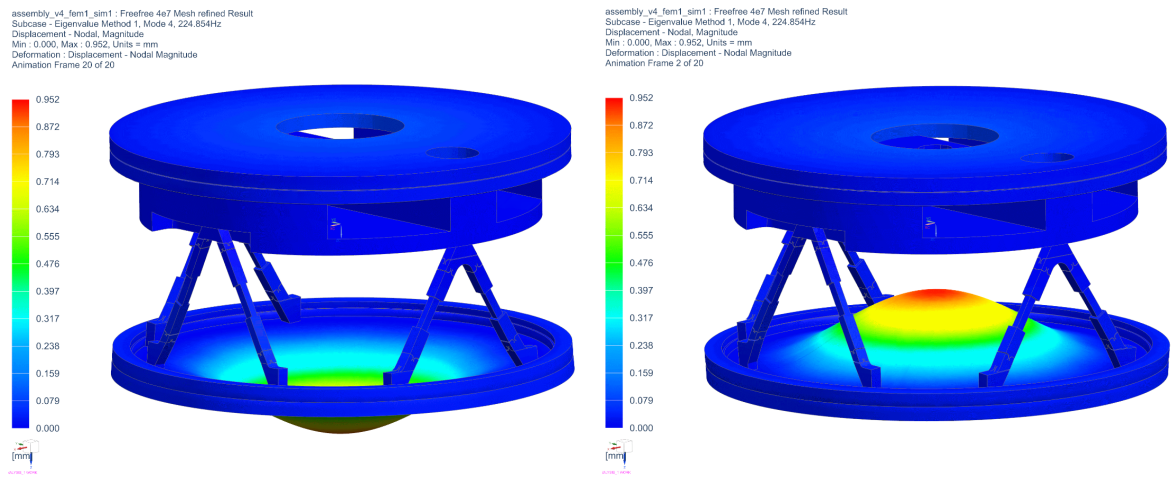

Figure B.2: Mode shape of mode 4 of the plate at $f = 224$ Hz.

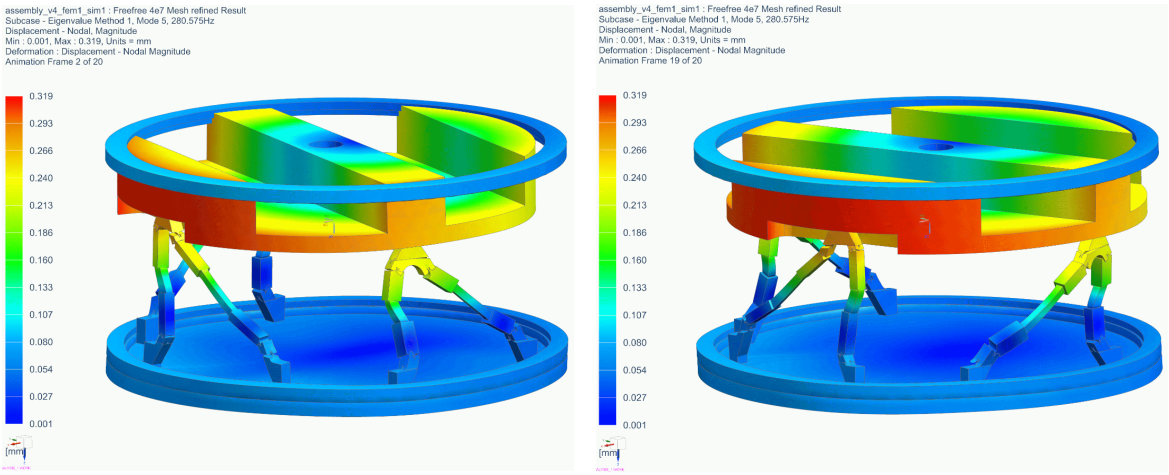

Figure B.3: Mode shape of mode 5 in R_z-direction at $f = 280$ Hz.

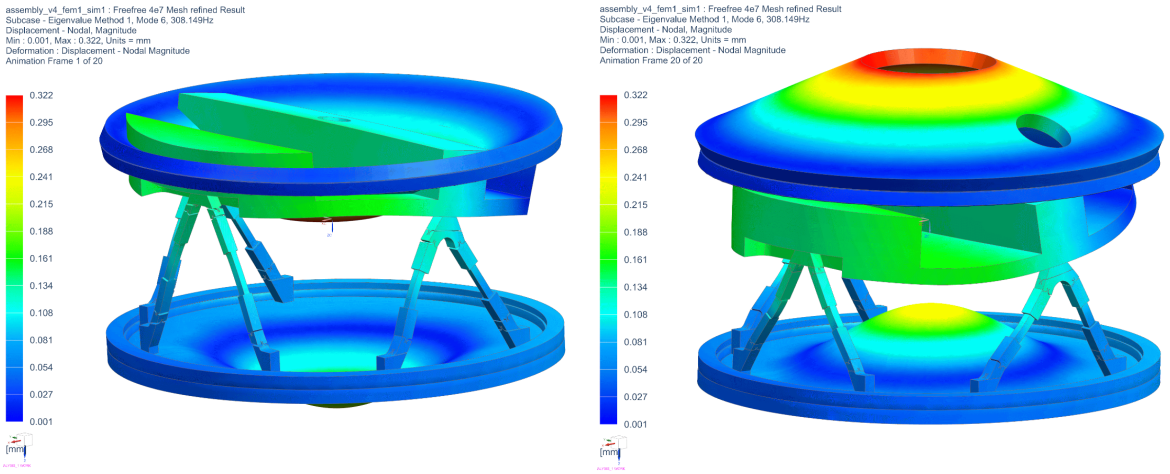

Figure B.4: Mode shape of mode 6 in z-direction and of the vacuum vessel at $f = 308$ Hz.

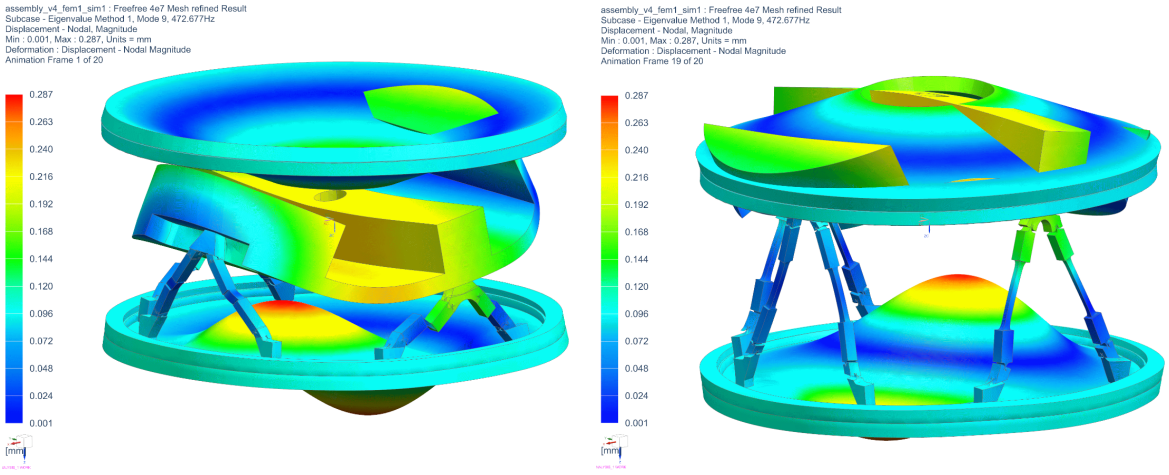

Figure B.5: Mode shape of mode 9 in z-direction and of the vacuum vessel at $f = 472$ Hz.

APPENDIX C

Experiments

C.1 Thermal feasibility

It is chosen to make use of liquid nitrogen cooling in an open system to test at cryogenic temperatures. Other options which required active cooling systems were considered, but turned out less feasible. Although the demo setup is designed for direct connection to a cryogenic two-stage cooling system (e.g. Cryomech PT420), this option required too much designing time and extra expenses. Also, the demo setup was too big for using a third party cryogenic cooling chamber and this option would give limitation for available testing time.

The thermal feasibility of the experiments is tested in two ways. First by estimating the volume of liquid nitrogen (LN2) needed to cool down the total setup. Secondly, the thermal time constant is derived by means of a modelled thermal resistance network. By estimating the thermal time constant, it can be estimated what the time span is for conducting the experiments over a certain temperature range.

C.1.1 Heat capacitance

To know how much heat has to be taken out of the setup, the heat (or thermal) capacitance of the masses is needed. The specific heat capacitance, considering constant pressure, but changing temperature is given by

$$c_p(T) = \frac{1}{m}\frac{dQ}{dT} \tag{C.1}$$

Here it is seen that the capacitance is a function of temperature. The dependence on temperature for the aluminium isolation frame and the stainless steel vacuum vessel can be found in respectively Figure C.1 and Figure C.2. The total heat capacitance can be calculated by integrating the specific heat over the temperature range and multiplying this with the corresponding mass as given by

$$E_{tot} = \left(m_{AL} \int_{77K}^{293K} c_{p,AL} dT + m_{SS} \int_{77K}^{293K} c_{p,SS} dT \right) \tag{C.2}$$

This results into a total energy of $E_{tot} = 8.6$ MJ to be removed from the setup to cool it to a temperature $T = 77$ K from room temperature.

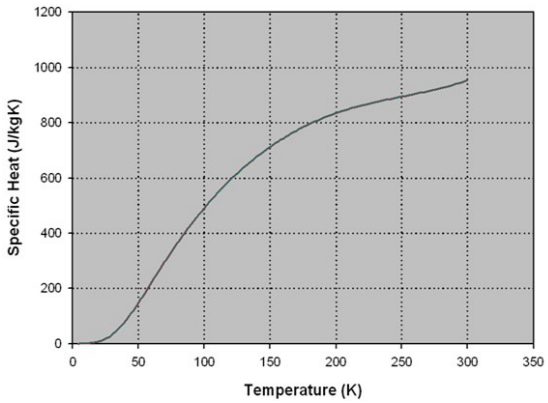

Figure C.1: Specific heat capacitance of AL6061 (Source: [68])

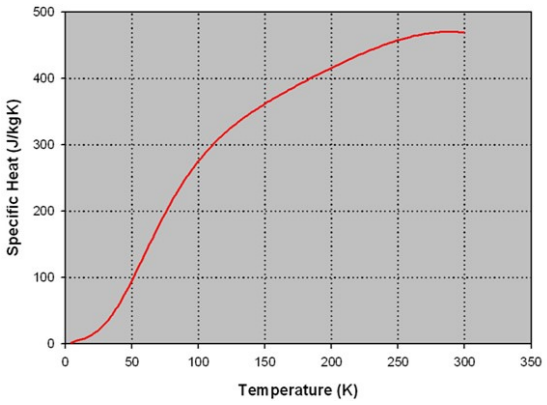

Figure C.2: Specific heat capacitance of SS304 (Source: [68])

C.1.2 LN2 cooling

As the liquid nitrogen is stored at or real close to its boiling temperature ($T = 77$ K), the energy transfer occurs by the phase change of LN2. Cooling the demo setup is thus based on the latent heat of vaporization of liquid nitrogen which is equal to $L_{LN_2} = 2e5$ J/kg. Removing an amount of $E_{tot} = 8.6$ MJ to cool the demo setup will take $m_{LN_2} = 43$ kg of liquid nitrogen. Assuming a spillage (e.g. vaporization when in contact with air) of at least 50% of the LN2, the demo setup can still be cooled down with a single dewar of 150L (≈ 120 kg). This is the first step of showing the thermal feasibility of using liquid nitrogen for the experiments.

C.1.3 Heat load

The next step is to make sure the setup is not immediately heating up again by looking at the heat load. When assuming a natural convection of 25 W/mK around the vacuum vessel, the thermal resistance towards the ambient world is only $R_{conv,nat} = 0.05$ K/W. For this reason EPS isolation is placed around the whole setup to create a significant larger thermal resistance of $R_{EPS} = 1.3$ K/W. The only remaining heat load, when placing the setup in EPS isolation, is the conductance of the wiring of $R_{wires} = 206$ K/W. Due to a high geometry ratio L/A, a high wire resistance is realized.

The heat transfer between the vacuum vessel and the isolation frame can be modelled by a combined thermal resistance of different components. The convection and radiation between the isolation mass and the vacuum vessel are estimated by assuming a parallel plate condition between the two masses, resulting in thermal resistance of $R_{conv} = 0.128$ K/W and $R_{rad} = 9.4$ K/W between vacuum vessel and isolation mass. The third component is the solid conduction occurring via the V-frames, which is relatively high ($R_{cond} = 20.9$ K/W). Details on the derivation of all heat load components can be found in Appendix C.1.

C.1.4 Thermal model

The derived thermal resistances can be used to set up the thermal network of the system. The network is shown in Figure C.4 and consists of three nodes representing the ambient temperature T_{amb}, the temperature of the vacuum vessel T_{vv} and the temperature of the

isolation mass T_{iso}. The nodes are connected by the thermal capacitances C_{vv} and C_{iso} and the total resistances between the nodes, which values can be found in Table C.1.

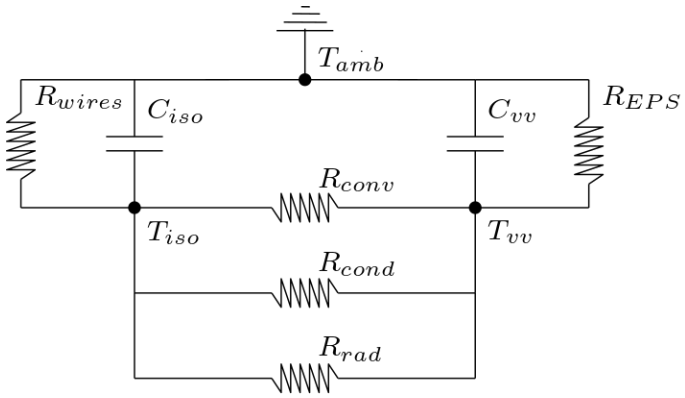

Figure C.3: Simplified thermal network demo setup

Table C.1: Thermal resistance and capacitance of demo setup

Parameter	Value	Unit
C_{vv}	25.1	MJ
C_{iso}	14.6	MJ
$R_{conv,nat}$	0.05	K/W
R_{EPS}	1.3	K/W
R_{wires}	206	K/W
R_{conv}	0.128	K/W
R_{rad}	9.4	K/W
R_{cond}	20.9	K/W

Setting boundary conditions of $T_{amb,0} = 293$ K and $T_{vv,0}, T_{iso,0} = 77$ K results in the thermal behaviour of Figure C.4. Here it can be seen that it takes approximately 10 hours for the setup to heat to 180 K, meaning on average an hour is available to make a measurement in a range of 10 K. This is considered feasible for the measurement plan of Section 5.1.

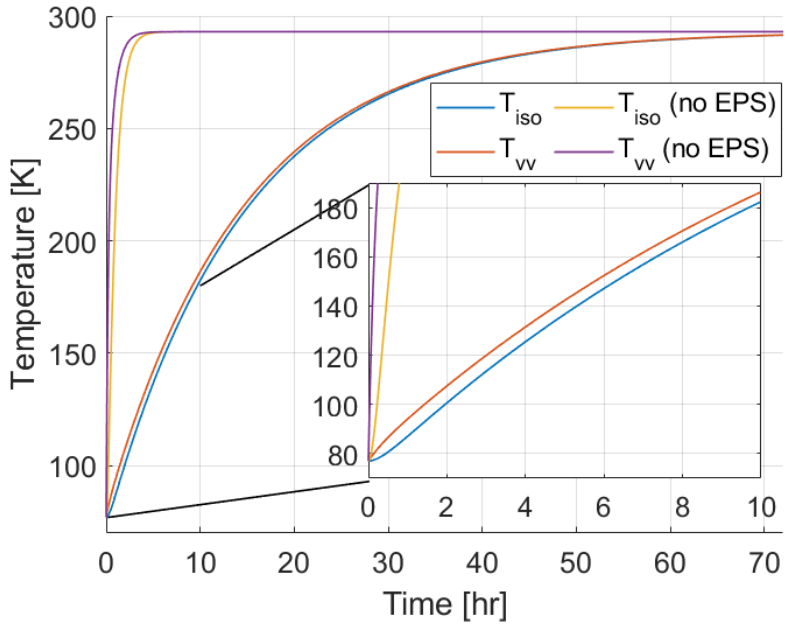

Figure C.4: Simplified thermal network behaviour of demo setup

When removing the EPS isolation, the setup will heat significantly faster. This effect is also shown in Figure C.4, where the temperature goes within 1 hour to 200 K. This shows the necessity of the EPS isolation.

C.1.5 Thermal results

Measurements are performed to validate the expected heat behaviour of the setup after cooling to 77 K. Temperature sensors are placed at 9 locations in the setup, which can be seen in the setup overview of Figure 5.1. Two of the sensors (T_6, T_7) are placed on the isolation mass and one sensor (T_{10}) is placed on the vacuum vessel. To know the temperature in the piezo element, the temperature is measured below and above piezo P_1 (by T_1, T_2) and piezo P_7 (by T_3, T_4). Furthermore, the temperature above piezo P_3 (by T_5) and above piezo P_5 (by T_8) is measured. The temperature over time can be found in Figure C.5.

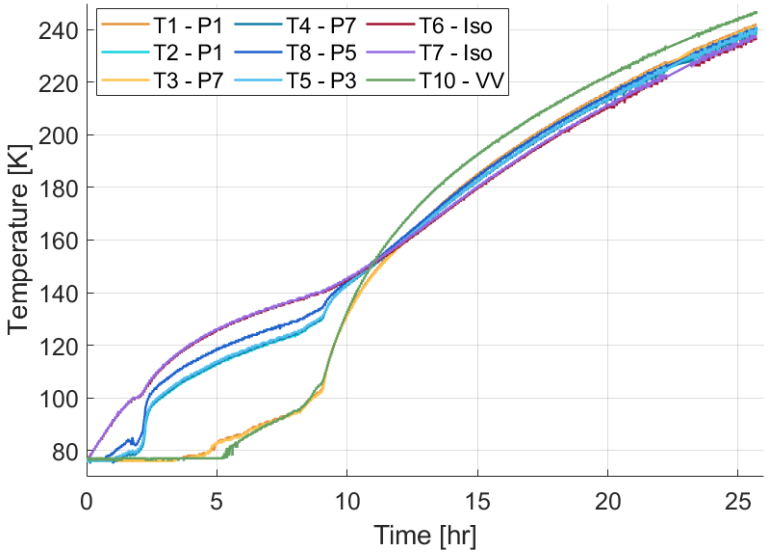

Figure C.5: Simplified thermal network behaviour of demo setup

It is seen that the heating does not occur homogeneously in the temperature range of 77-150K. Which is the range of interest. This effect occurs due to LN2 remaining on the bottom of the vacuum vessel, having a cooling effect on the bottom, although the rest of the setup is already heating. This can be seen by the temperature sensors T1, T3 and T10 which are all placed relatively low in the setup and stay at 77K for the first 5 hours. The sensors T2, T4, T5 and T8 which are placed higher on the V-frames already start heating together with the isolation mass. Around 5 hours the lower sensor locations also start to heat, but there is still LN2 in the setup. After 9 hours, the LN2 is all evaporated and the heating finally starts to occur homogeneously.

The heating behaviour measured after 10 hours is more or less the same as what was shown in the thermal model results of Figure C.4 with a gradient of approximately 10 K per hour. Here it is also seen that the vacuum vessel heats first, then the piezo transducers and lastly the isolation mass, which is as expected based on the heat load on the system.

Although the inhomogeneous effect due to LN2 in the vessel is not desired, the feasibility of using LN2 to cool down the setup is still proven. It is also shown that the use of EPS isolation results in a good thermal time constant to perform the measurements.

C.2 Experimental setup

Pictures of the used setup can be found in Figure C.6 and Figure C.7. Here it can be seen how the demonstrator was 'filled' with liquid nitrogen by using a 150 L storage dewar. It can also be seen how the demonstrator is supported by 12 spacers in order to not have any friction damping and to obtain a certain level of decoupling from the table.

Figure C.6: Demonstrator with spacers (vacuum vessel top taken of for picture)

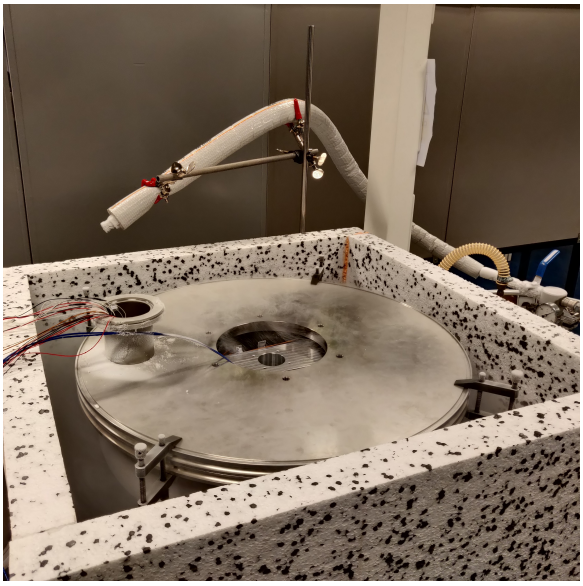

Figure C.7: Demonstrator cooled and isolated (EPS top taken of for picture)

C.2.1 Equipment

For measuring the temperature, thin film resistance temperature detectors (RTD) are used (model p1k0.232.6w). Two sets of 5 sensors are connected in series and supplied by a 1 mA current source. Two data acquisition systems (NI USB-3211) are used to measure the voltage over the RTD sensors. The accelerometers (PCB Model: 351B41) give a voltage output (due to its Integrated Circuit Piezoelectric system), which is measured by a third data acquisition system. For measuring the capacitance, a Keysight U1733C LCR meter is used.

C.3 Results

The comparison between excitation with transducer P_1 and P_7 is shown in Figure C.8. It can be observed that there is difference in response, which was the reason to use transducer P_7. However, it is shown that using transducer P_1 was also a possibility.

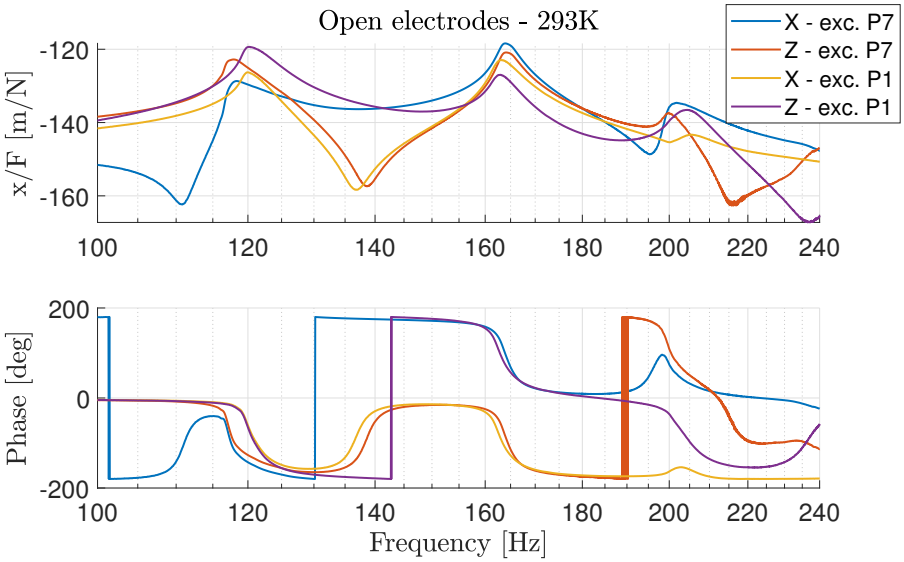

Figure C.8: Comparison of piezo P7 and P1 excitatoin

In Figure C.9, the transfer function in X-direction is shown over a range of 10-1500 Hz. This is done to show the higher Z mode present around 450 Hz.

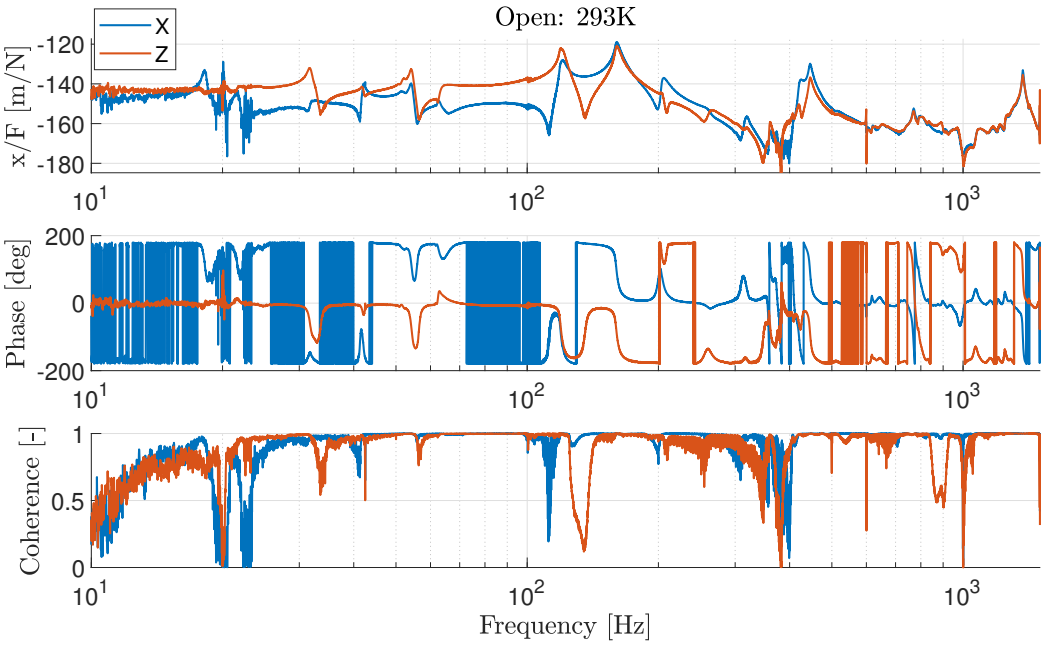

Figure C.9: Transfer function of a wider frequency range

In Figure C.10 it can be seen that good coherence is obtained for measurements in the range of 80-350 Hz. This shows a typical coherence result, which is seen for most measurements.

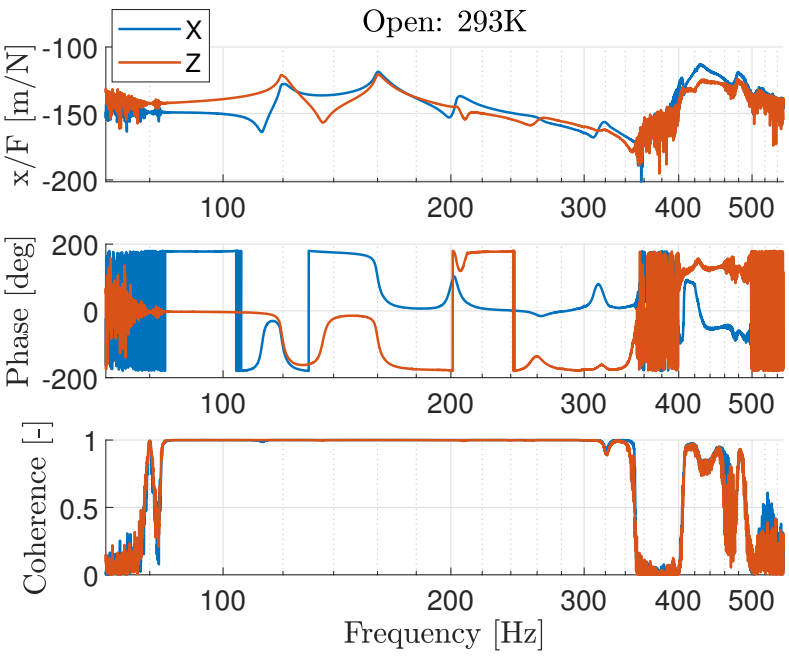

Figure C.10: Transfer function with typical coherence values for performed measurements

The damping results and different tuning situation for the temperatures in the range of T = 100 K − 205 K are shown in Figures C.11-C.20.

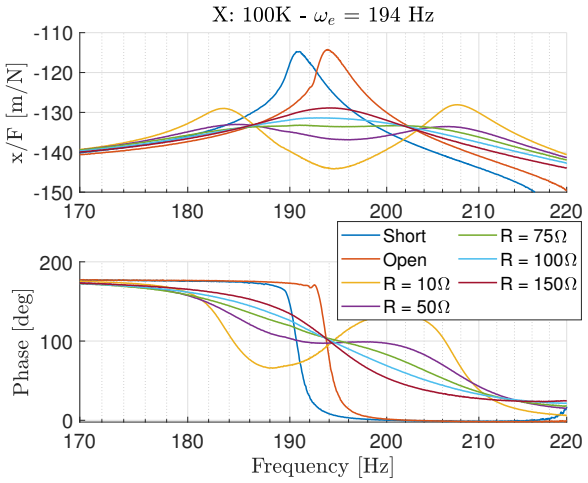

Figure C.11: Tuning of shunt system at 100K

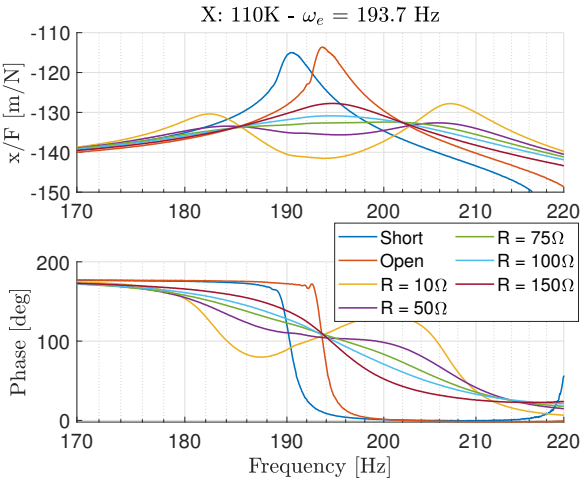

Figure C.12: Tuning of shunt system at 110K

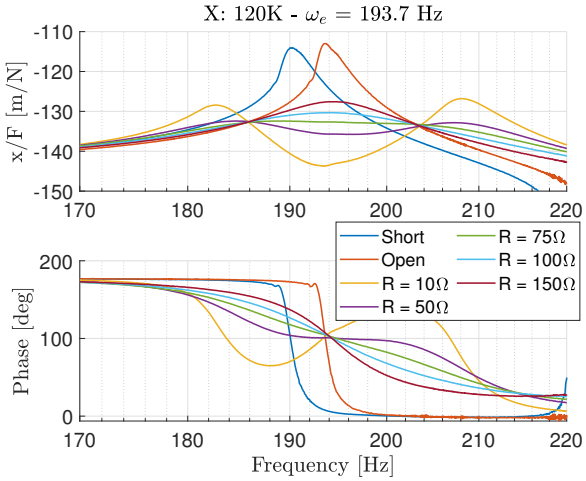

Figure C.13: Tuning of shunt system at 120K

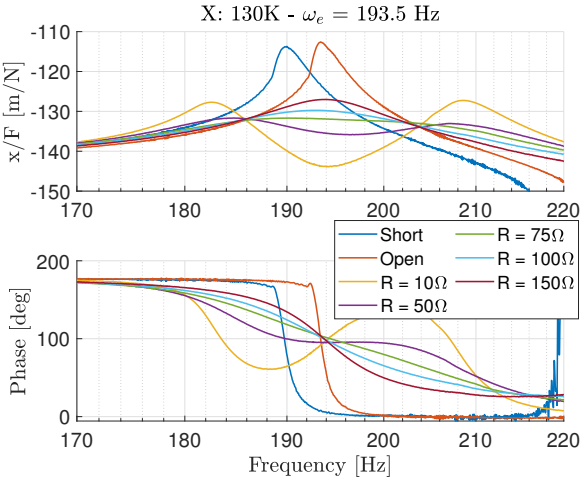

Figure C.14: Tuning of shunt system at 130K

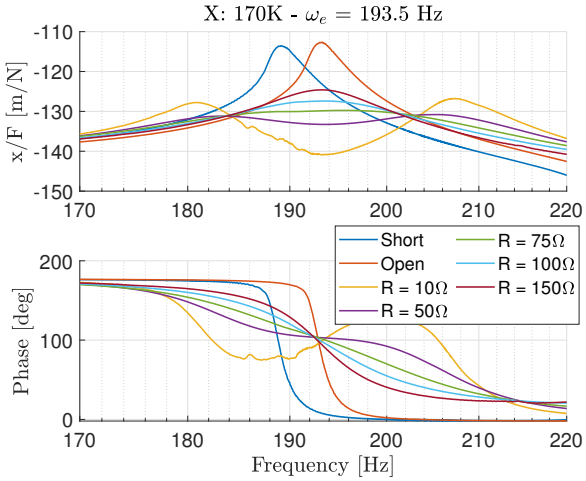

Figure C.15: Tuning of shunt system at 170K

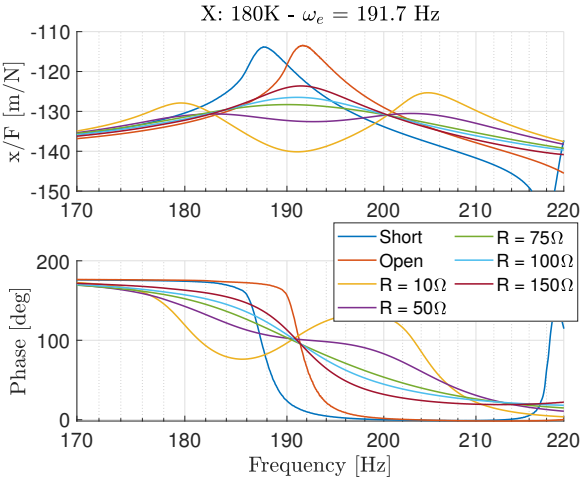

Figure C.16: Tuning of shunt system at 180K

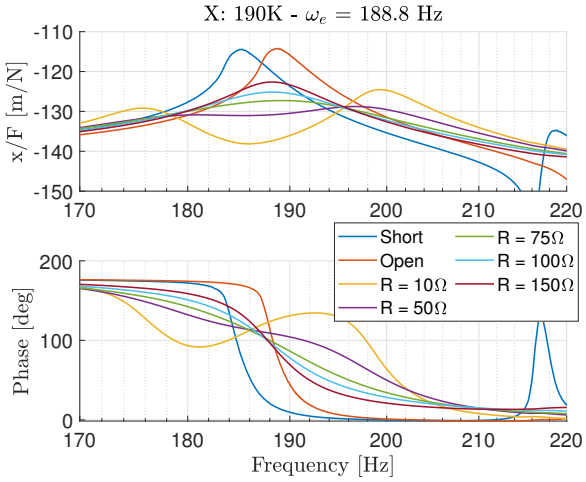

Figure C.17: Tuning of shunt system - 190K

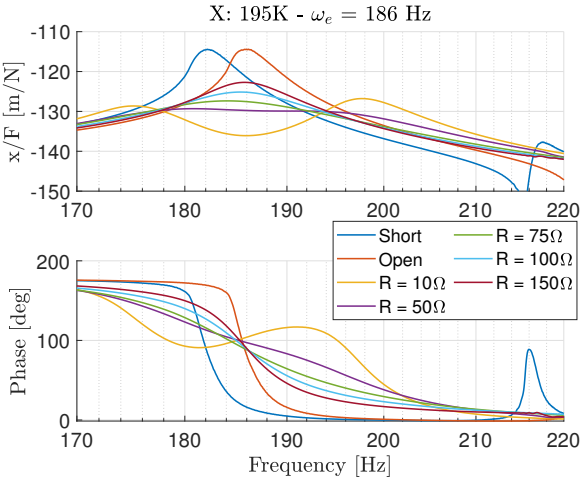

Figure C.18: Tuning of shunt system - 195K

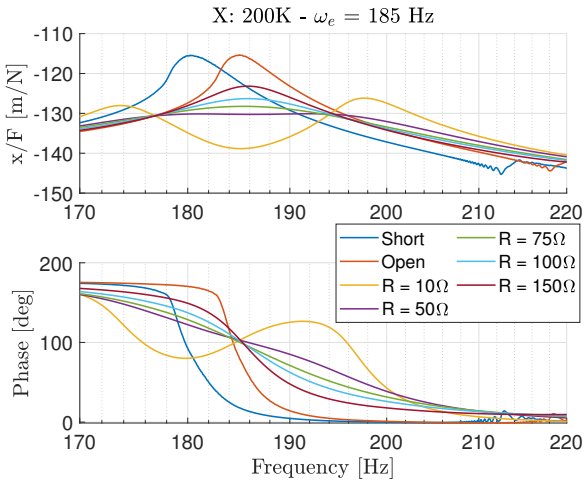

Figure C.19: Tuning of shunt system - 200K

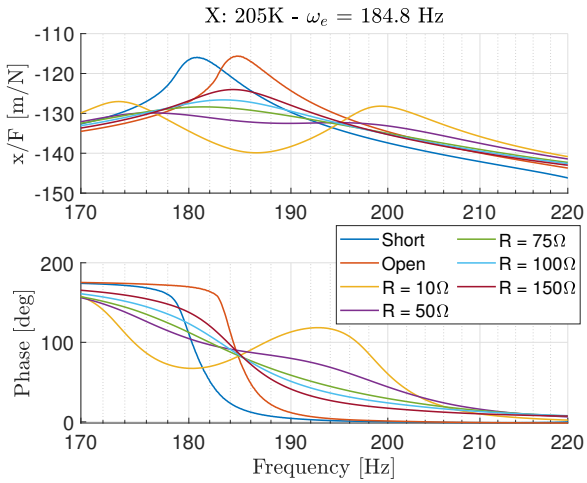

Figure C.20: Tuning of shunt system - 205K

The benefit of implementing multiple transducers into the structure is shown in Figure C.21, by damping two modes simultaneously. Here, transducer P_4 is used to damp at $f = 191$ Hz with a resistance of $R = 75\ \Omega$, while transducer P_3 is used to damp the peak at 210 Hz with a resistance of $R = 10\ \Omega$ and $50\ \Omega$. No clear tuning rules where derived for modes laying this close to each-other. However, by manual tuning, the extra suppression on both modes is shown, which shows potential for using multiple transducers simultaneously.

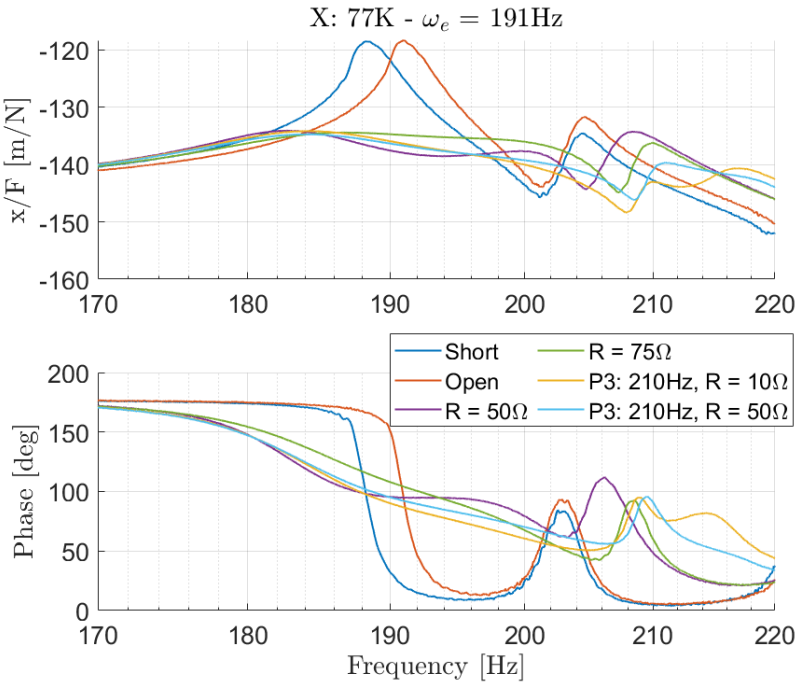

Figure C.21: Damping 2 modes at 77K using P4 for 191 Hz and P3 for 210 Hz

Technische Universiteit
Eindhoven
University of Technology

Declaration concerning the TU/e Code of Scientific Conduct for the Master's thesis

I have read the TU/e Code of Scientific Conduct[i].

I hereby declare that my Master's thesis has been carried out in accordance with the rules of the TU/e Code of Scientific Conduct

Date

31-03-2021

Name

Ambaum, N (Niek)

ID-number

0910516

Signature

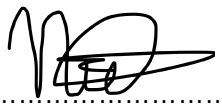

Submit the signed declaration to the student administration of your department.

[i] See: http://www.tue.nl/en/university/about-the-university/integrity/scientific-integrity/
The Netherlands Code of Conduct for Academic Practice of the VSNU can be found here also.
More information about scientific integrity is published on the websites of TU/e and VSNU